Spatial and temporal coupling between tectonics and surface processes during lithosphere inversion of the Pyrenean-Cantabrian Mountain belt : contraints from exhumation histories and surface process modelling

Zoltan Erdös

UNIVERSITÉ DE GRENOBLE

THÈSE

Pour obtenir le grade de

DOCTEUR DE L'UNIVERSITÉ DE GRENOBLE

Spécialité : **Sciences de la terre et univers, environnement**

Arrêté ministériel : 7 août 2006

Présentée par

Zoltán Erdős

Thèse dirigée par **Ritske S. Huismans** et **Peter A. van der Beek**
codirigée par **Haakon Fossen**

préparée au sein du **Institut des Sciences de la Terre**
dans **l'École Doctorale Terre, univers, environnement**

Modélisation couplée de la tectonique et des processus de surface dans l'extension et l'inversion des Pyrénées

Thèse soutenue publiquement le **26.09.2014**,
devant le jury composé de :

Prof., François, Roure
Président, Rapporteur
Prof., Taras, Gerya
Rapporteur
Prof., Peter A., van der Beek
Membre
Prof., Ritske S., Huismans
Membre

Université Joseph Fourier / Université Pierre Mendès France /
Université Stendhal / Université de Savoie / Grenoble INP

UNIVERSITETET I BERGEN

Coupled surface process and tectonic modelling of extension-inversion tectonics in the Pyrenees

Dissertation for the degree of Philosophiae Doctor (PhD)

Zoltán Erdős

University of Bergen

2014

Preface

The research presented in this thesis was conducted at the Department of Earth Science, University of Bergen (Norway), and in parallel at the Institute of Earth Sciences, Joseph Fourier University (Grenoble, France) under the supervision of Prof. Ritske Huismans, Prof. Peter van der Beek and Prof. Haakon Fossen. The project started in September 2009 and was funded by the Norwegian Research Council through the Norwegian component of the European Science Foundation Eurocore TOPO-Europe project PyrTec. The computationally intensive numerical modeling was carried out on the University of Bergen supercomputers Fimm and Hexagon, maintained by the Bergen Center of Computational Science.

The thesis is structured in accordance with the Norwegian guidelines for doctoral dissertations in natural sciences, where the main body of the thesis consists of research papers either published, submitted or about to be submitted to international peer-reviewed journals. The present thesis comprises three papers: Paper 1 has been accepted for publication by the AGU journal Tectonics; Paper 2 has been submitted to Earth and Planetary Science Letters; and Paper 3 is in preparation for the Journal of Geophysical Research. The three research papers are preceded by an Introductory Chapter that details the general background and aims of the project, synthesizes its outcome, and outlines prospects for future work. An authorship statement provides an overview of the contribution of each author to this collaborative research work.

Acknowledgements

First of all, I would like to thank my supervisors: Ritske Huismans, for giving me the opportunity to embark on the great journey that is getting a PhD and for guiding my way throughout patiently; Peter van der Beek, for supporting and encouraging me tirelessly all the way despite the huge geographical distance between us and for the countless insightful suggestions throughout or work together; Haakon Fossen for his kindness and encouragement and for all the helpful discussions. I am truly grateful for the belief that all three of them have shown in me.

I would like to thank Jean Braun for his contagious enthusiasm and the helping hand he gave me with the use and development of his code, Pecube, and Cedric Thieulot for all the long hours he devoted to share his knowledge on numerical modeling and his code, FANTOM.

I would like to thank the Department of Earth Science both in Bergen and Grenoble, for supporting me with a truly pleasant and stimulating working environment. From the PhDs and postdocs, through the permanent researchers to the administrative stuff, everybody was always kind, helpful, and incredibly friendly towards me.

I am immensely thankful for a huge number of people who have been incredibly supportive towards me and made my days a lot more joyful and without whose help my life would have been a lot grayer and a lot more difficult. I will not name them all (seriously, it would cost the trees of a small rainforest to print it) but I will simply thank the *lunch group*, the *cake-club*, the *geo-sports* and all the kind people I met in Bergen and Grenoble for making my days that much better.

Finally, I would like to thank my family and friends in Hungary for their long-distance support and last but by no means least I would like to say thank you to Iló, for bearing with me throughout the ups and downs of this incredible adventure to a land up, North!

Table of Contents

List of Publications

Erdős, Z., van der Beek, P., Huismans, R. S.
Evaluating balanced section restoration with thermochronology data: a case study from the Central Pyrenees
Tectonics, 33, doi:10.1002/2013TC003481

Erdős, Z., Huismans, R. S., van der Beek, P.
First order control of syntectonic sedimentation on crustal-scale structure of mountain belts
Submitted to *Earth and Planetary Science Letters*

Erdős, Z., Huismans, R. S., van der Beek, P.
Extensional inheritance and surface processes as controlling factors of mountain belt structure
Submitted to the *Journal of Geophysical Research*

Authorship statement

The main body of this thesis consists of three research papers, with the Ph.D. candidate Zoltán Erdős as the first author of all three and the sole author of the Introductory Chapter to the thesis. The research papers are a result of collaborative work and the relative contribution of their authors is specified below.

Paper 1: Evaluating balanced section restoration with thermochronology data: a case study from the Central Pyrenees by **Z. Erdős**, **P. van der Beek** and **R.S. Huismans**

All three authors were actively involved in designing the general concept of the novel method presented in the paper. **EZ** subsequently modified the thermo-kinematic model to suit the method, carried out the structural-kinematic modeling, the thermo-kinematic modeling and the statistical analysis of the case study. **EZ** also wrote the manuscript and drafted the figures. **PvdB** contributed to the thermo-kinematic modeling, the statistical analysis, the editing of the manuscript and participated in the joint discussions of the results. **RSH** contributed to the structural-kinematic modeling, the editing of the manuscript and participated in the joint discussions of the results.

Paper 2: First order control of syntectonic sedimentation on crustal-scale structure of mountain belts by **Z. Erdős**, **R.S. Huismans** and **P. van der Beek**

All three authors were actively involved in designing the experimental model setup presented in the paper. **EZ** subsequently implemented the surface process algorithms, carried out the thermo-mechanical modeling, the literature study, wrote the manuscript and drafted most of the figures. **RSH** contributed to the literature study, the editing of the manuscript, the design of figure 5 and figure 6 and participated in the analysis of the results. **PvdB** contributed to the literature study, the editing of the manuscript and participated in the analysis of the results.

Paper 3: Extensional inheritance and surface processes as controlling factors of mountain belt structure by **Z. Erdős**, **R. Huismans** and **P. van der Beek**

All three authors were actively involved in designing the experimental model setup presented in the paper. **EZ** carried out the thermo-mechanical modeling, wrote the manuscript and drafted the figures. **RSH** contributed to the editing of the manuscript, and participated in the joint discussions of the results. **PvdB** contributed to the editing of the manuscript and participated in the joint discussions of the results.

Abstract

Orogenic belts are fundamental features of plate tectonics. The crustal structure of orogens around the world shows a wide range of deformation styles from narrow, asymmetric wedges like the Pyrenees to wide, plateau-like orogens such as the Zagros or the Himalaya.

The primary controlling factor on the size and structure of an orogen is the amount of convergence between the colliding plates. However, there are important additional factors providing major controls on the structural development of orogens. Among the potential parameters that can affect the style of deformation are the crustal strength, inherited weaknesses, and the surface processes. These parameters have been studied extensively in the past but their overall importance remains unclear.

The aim of this thesis is to improve our understanding of: (1) How surface processes affect mountain building, with a special focus on the relationship between thin-skinned deformation of forelands and thick-skinned internal deformation of orogens. (2) How inherited extensional structures affect mountain building. The study was carried out using the Pyrenees as a special reference case.

To answer our research questions we have used a wide range of state-of-the-art numerical modelling tools. In paper 1 we present a new method where we couple a structural-kinematic model and a thermo-kinematic model to evaluate the consistency of existing balanced section reconstructions with independent thermochronology data. In papers 2 and 3 we use 2D lithospheric scale thermo-mechanical models with surface process algorithms.

Using the above toolset, we demonstrate that syntectonic sedimentation results in longer basement thrust sheets as well as longer thin-skinned thrust sheets and a generally wider orogen. Conversely erosion tends to narrow the wedge and reduce the orogenic loading of the colliding plates, limiting the space available for deposition in the foreland deeps.

We also demonstrate that inherited extensional structures play a crucial role in mountain building as they facilitate the migration of deformation into the undeformed basement of the overriding plate. Moreover, a significant amount of lower-crustal/mantle-lithospheric material is preserved at shallow depths only in the presence of extensional inheritance, but significant erosion is needed in order to bring this material to the surface.

Our models also show that thin-skinned thrust sheets are generally rooted in the footwall of basement thrusts as they form outward-propagating sequences. As soon as a new basement thrust forms, the thin-skinned sequence situated on top of the new basement thrust-sheet is abandoned in favour of a new sequence in the footwall of the basement thrust.

Regarding our case study, in the modelling presented in paper 1, we found that it was possible to reproduce the section restoration of the Pyrenees proposed by Muñoz (1992), using a structural-kinematic model with high accuracy up to its 36 Ma time slice and with limited accuracy up to its 50 Ma time slice. The thermochronometric ages predicted by the subsequent thermo-kinematic modelling of the orogen are generally in good agreement with both the high- and low-temperature thermochronology data available in the Central Pyrenees; hence we conclude that the examined restoration is to a first order consistent with these datasets. The predicted thermochronological ages approximate the available low-temperature thermochronology data better by taking into account a late-stage burial and re-excavation scenario affecting the southern flank of the Pyrenean wedge presented by Coney et al. (1996), and quantified by Fillon and van der Beek (2012).

Moreover, our thermo-mechanical model experiments presented in papers 2 and 3 suggest, that extensional inheritance played a prime role in the structural evolution of the Pyrenees, with the major characteristics of the North Pyrenean Unit, including the presence of steep, inverted normal faults, the relative tectonic quiescence of the area after the early inversion and the presence of a lower-crustal body at shallow depth below the unit, best recaptured by our accordion models.

Résumé

Les chaînes orogéniques sont l'une des manifestations fondamentales de la tectonique des plaques. La structure des chaînes de montagnes sur Terre montre une variation importante des styles de déformation entre, d'une part, des prismes étroits et asymétriques comme les Pyrénées et, d'autre part, des orogènes larges associés à des plateaux orogéniques comme le Zagros ou l'Himalaya.

Le facteur primordial déterminant la taille et la structure des chaînes orogéniques est la quantité de convergence entre les plaques en collision. Cependant, d'autres facteurs peuvent fortement contrôler le développement structural des orogènes. Quelques-uns des facteurs affectant potentiellement le style de déformation sont la résistance crustale, les zones de faiblesse héritées, et les processus de surface. Malgré de nombreuses études concernant ces facteurs, leur importance générale reste mal connue.

Le but de cette thèse est d'améliorer notre compréhension de : (1) comment les processus de surface affectent le développement des orogènes, en se focalisant particulièrement sur les relations entre la déformation « thin-skinned » des zones d'avant-pays et la déformation « thick-skinned » à l'intérieur des orogènes ; (2) comment les structures extensives héritées affectent le développement des chaînes de montagne. Cette étude utilise les Pyrénées comme cas de référence.

Afin de répondre à ces questions, nous avons utilisé différents outils de modélisation numérique développés récemment. Dans une première partie, nous présentons une nouvelle méthode couplant un modèle structural-cinématique avec un modèle thermo-cinématique afin d'évaluer la cohérence des restaurations basées sur des coupes équilibrées avec des données thermochronologiques obtenues de façon indépendante. Dans les deuxième et troisième parties de la thèse, nous utilisons des modèles thermo-mécaniques 2D à l'échelle de la lithosphère incluant des algorithmes pour modéliser les processus de surface.

Avec ces outils, nous démontrons que la sédimentation syn-tectonique mène à des nappes de charriage de socle, ainsi que des nappes de charriage de surface, plus longues et donc à un orogène généralement plus large. Au contraire, l'érosion tend à diminuer la largeur du prisme orogénique ainsi que la charge orogénique sur les plaques en collision, diminuant ainsi l'espace disponible pour le dépôt de sédiments dans les bassins d'avant-pays.

Nous démontrons également que les structures héritées d'une phase d'extension jouent un rôle crucial dans le développement des chaînes de montagnes en facilitant la migration de la déformation vers le socle non-déformé de la plaque chevauchante. En outre, des quantités importantes de matériel provenant de la croûte inférieure ou du manteau lithosphérique peuvent être transportées vers de faibles profondeurs seulement en présence d'un héritage extensif. Néanmoins, une érosion importante est nécessaire afin de faire affleurer ce matériel à la surface.

Nos modèles montrent finalement que les nappes de charriage superficiels sont généralement enracinées dans le mur des chevauchements crustaux (affectant le socle) lors de la formation de séquences de propagation frontale. Dès qu'un nouveau chevauchement crustal se forme, la série de chevauchements « thin-skinned » située au-dessus de la nouvelle nappe de charriage crustale est abandonnée en faveur d'une nouvelle série se formant dans le mur de ce chevauchement.

En ce qui concerne notre cas d'étude, la modélisation présentée dans la première partie montre qu'il est possible de reproduire la coupe équilibrée et la restauration des Pyréneés proposées par Muñoz (1992), en utilisant un modèle structural-cinématique avec une bonne précision jusqu'à la restauration à 36 Ma et avec une précision acceptable jusqu'à la restauration à 50 Ma. Les âges thermochronologiques prédits par la modélisation thermo-cinématique de la chaîne qui s'en suit concordent généralement bien avec les données thermochronologiques (de haute ainsi que de basse température) disponibles dans les Pyrénées centrales ; ainsi nous concluons que la restauration évaluée est en premier ordre cohérente avec ces données. Nous obtenons un meilleur accord entre âges

thermochronologiques prédits et les données thermochronologiques de basse température disponibles en incluant un scénario d'enfouissement et ré-excavation tardifs du flanc sud des Pyrénées, comme proposé par Coney et al. (1996), et quantifié précédemment par Fillon et van der Beek (2012).

Nos modélisations thermo-mécaniques présentées dans les parties 2 et 3 suggèrent que l'héritage extensif a joué un rôle primordial dans l'évolution structurale des Pyrénées. Des caractéristiques majeurs de l'Unité Nord-Pyrénéenne, notamment la présence de failles normales inversées à fort pendage, la quiescence relative de cette partie du prisme après l'inversion précoce, et la présence de matériel de la croûte inférieure à des faibles profondeurs, sont reproduits par nos modèles « en accordéon » qui incluent une phase d'extension initiale avant la phase de convergence et collision.

Part I
Introduction

Introduction

State of the art

Orogenic belts and their foreland basins are fundamental features of plate tectonics that can be generally associated with convergent plate-boundaries. The crustal structure of orogens around the world shows a wide range of deformation styles from narrow, asymmetric doubly-vergent wedges like the Pyrenees (Muñoz, 1992) to wide, plateau-like orogens such as the Zagros mountain belt (Mouthereau et al., 2007) or the Himalaya (e.g., DeCelles et al., 2001) (Gehrels et al., 2003).

Recently, Jamieson and Beaumont (2013) proposed a conceptual temperature-magnitude framework for orogenesis (Figure 1). In their work they propose that orogens can be placed on a scale ranging from small-cold to large-hot orogens. Examples of small-cold orogens are the Southern Alps of New Zealand (Beaumont et al., 1996) or Taiwan (Mouthereau, 2003; Simoes et al., 2007). This category is defined to cover those orogens in which the upper part of the sublithospheric mantle underthrusts with little deformation, particularly with little bulk shortening, and where crustal thickening and heating are limited. On the other end of the scale reside the large-hot orogens, of which the Himalaya (DeCelles et al., 2001; Gehrels et al., 2003) is a prime example. These orogens are typically composed of a central elevated plateau underlain by thick crust, flanked by external wedges including fold-and-thrust belts, and foreland basins. As orogens grow, they eventually evolve from small-cold orogens dominated by critical wedge mechanics to large-hot orogens characterized by an orogenic plateau underlain by a weak ductile flow zone (Jamieson and Beaumont, 2013).

In this framework, the primary controlling factor on the size and overall structure of an orogen is the amount of convergence between the colliding plates. However, there are several important additional factors providing major controls on the structural development of mountain belts. Among the potential parameters that can significantly affect the style of deformation are the crustal strength, inherited weakness zones, and the efficiency of surface process. These parameters have been studied extensively in the last decades (Buiter, 2012;

Jammes and Huismans, 2012; Mouthereau et al., 2013; Mugnier et al., 1997; Stolar et al., 2006; Willett et al., 1993) but their relative importance remains unclear.

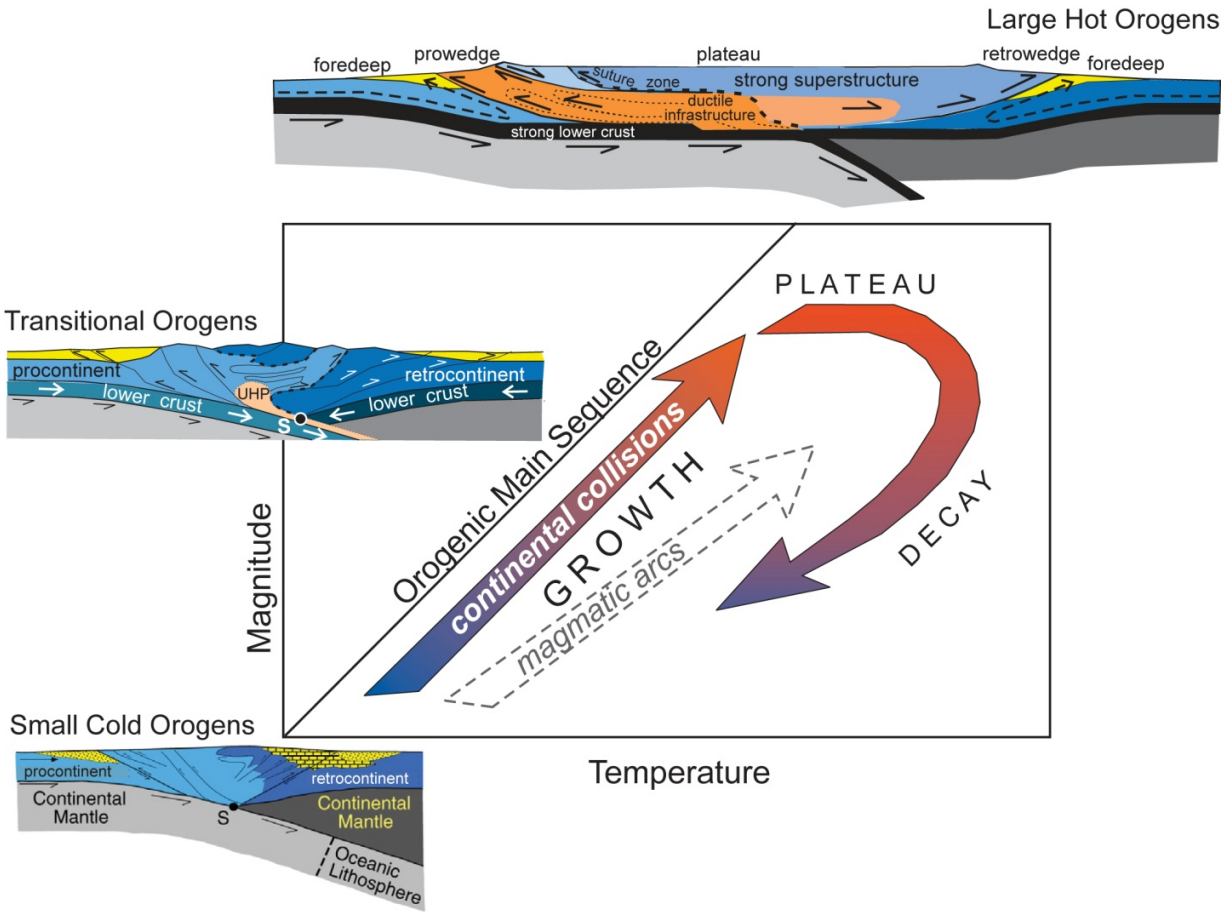

Figure 1 Conceptual orogenic temperature-magnitude diagram showing the growth from small-cold to large-hot orogens (after Jamieson and Beaumont, 2013). In collisional orogens, increasing magnitude and temperature both result from accretion and thickening of crustal material, factors that are ultimately dependent on the amount of convergence.

Numerous studies have shown that the relative strength of the crust and the mantle-lithosphere provides a first-order control on deformation processes in both extensional (Buck, 1991; Buck et al., 1999; Huismans and Beaumont, 2003, 2011; Huismans et al., 2005; Jammes and Huismans, 2012) and contractional settings (Beaumont et al., 1994; Ellis et al., 1998; Jammes and Huismans, 2012; Willett et al., 1993) with the depth and thickness of the viscous mid-crustal zone playing a pivotal role. In addition, as Jammes and Huismans (2012) have pointed out recently, the strength of the crust is heavily dependent on inherited weaknesses.

Although most orogens initiate by inversion of passive margins or rifted basins, we know very little about how the inherited extensional structures affect the evolution of these belts. Jammes and Huismans (2012) showed that rifting inheritance can explain the presence of a lower crustal/mantle lithospheric body at shallow depth, as inferred for the Pyrenees (Muñoz, 1992) and European Alps (Schmid and Kissling, 2000) for example, and that it facilitates the propagation of deformation to the external part of the orogen. However, their study focused mainly on the evolution of basement structures, as the resolution attained by their models was insufficient to address the small-scale structures.

The potential role of surface processes on mountain building is one of the hotly debated and contentious issues in the Earth Sciences (see Whipple, 2009 and references therein). Earlier research has predominantly focused on the effects of erosion on mountain building (e.g., Beaumont et al., 1992), (Willett, 1999), (Whipple, 2009)) and recently on sedimentation controls on thin-skinned deformation (Bonnet et al., 2007; Fillon et al., 2012; Storti and Mcclay, 1995). However, in spite of our improved understanding of the controls that surface processes exert on the evolution of contractional orogens, it is still unclear how they might affect mountain building in the presence of inherited extensional structures. Neither has much work been done to decipher which aspects of orogenic structure and evolution can be ascribed to tectonic inheritance or to surface processes specifically, and which of these provide the prime control on the structure of individual mountain belts.

Aims and Research Objectives

The aim of this thesis is to improve our understanding of:

(1) How surface processes affect mountain building, with a special focus on the relationship between thin-skinned foreland fold-and-thrust belts and thick-skinned deformation in the internal part of an orogen.
(2) How inherited extensional structures affect mountain building.

The study was carried out using the Pyrenees as a special reference case. This orogen is exceptionally well studied and a wealth of geological and geophysical data is available from its

central region. However, there remain significant uncertainties about the evolution of the belt, in particular concerning the relative roles of surface processes and inherited extensional structures in controlling the structure and evolution of the Pyrenean orogen.

Study area

The Pyrenees are a collisional orogen formed by convergence between the African-Iberian and European plates between Late-Cretaceous (90 Ma) to Early-Miocene (20 Ma) times. The convergence rate between the two blocks reached its peak during Eocene to Oligocene (50-20 Ma) times (Roest and Srivastava, 1991; Rosenbaum et al., 2002; Vissers and Meijer, 2012). The Pyrenees are an intracontinental convergence structure; Triassic – Late-Cretaceous extension did not lead to continental breakup between Europe and Iberia (even though the possible existence of an ocean remains advocated by some; see for instance Vissers and Meijer 2012). The range is dominated by inversion tectonics (Muñoz et al., 1986) owing to thrusting along pre-existing extensional structures. These structures were originally formed during Triassic to Cretaceous rifting and transtension associated with anticlockwise rotation of the Iberian plate with respect to Europe and consequent opening of the Bay of Biscay (Roest and Srivastava, 1991; Rosenbaum et al., 2002).

The asymmetrical Pyrenean orogen was built by northward underthrusting of the Iberian crust below the European crust, resulting in a wide southern pro-wedge and a narrower northern retro-wedge (figure 2 and 3). From south to north, the Pyrenees consists of the Ebro foreland basin; the South Pyrenean Unit, a fold-and-thrust belt consisting of Mesozoic and Cenozoic sedimentary successions; the Axial Zone, which comprises a south-vergent antiformal stack of upper-crustal thrust sheets; the North Pyrenean Unit, where basement and cover rocks form north vergent thrust sheets and pop-up structures; and the Aquatine foreland basin (Capote et al., 2002; Muñoz, 1992).

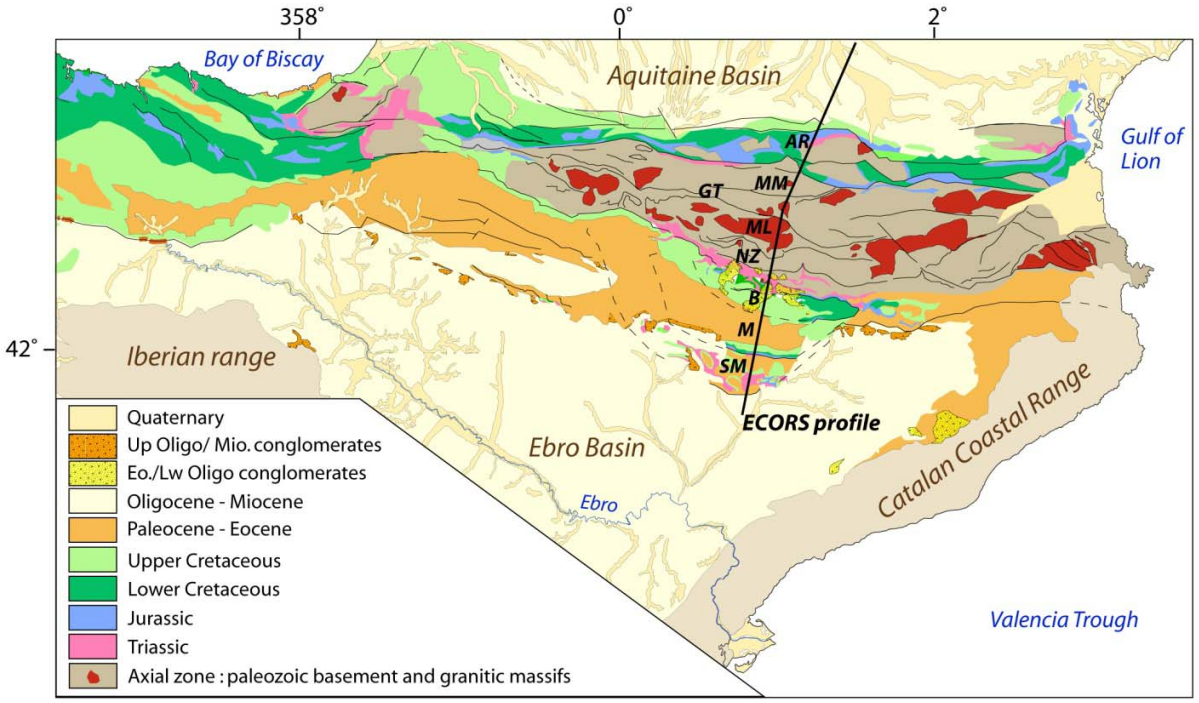

Figure 2 Geological map of the Pyrenees. The black line represents the ECORS deep seismic profile along which the balanced cross section of Figure 3 was constructed. AR: Arize block, MM: Marimaña massif, ML: Maladeta massif, NZ: Nogueres Zone, GT: Gavarnie-thrust B: Bóixols, M: Montsec, SM: Sierras Marginales (redrawn after Fillon and van der Beek (2012))

The kinematics of the South Pyrenean Unit are well constrained as the tectonic evolution is exceptionally well recorded by syntectonic sediments (Muñoz, 1992; Puigdefabregas et al., 1986; Puigdefabregas et al., 1992). The evolution of the Axial Zone is constrained by correlation of its basement thrust sheets with the thin-skinned structures of the South Pyrenean Unit, while the evolution of the North Pyrenean Unit is considerably less well constrained due to a lack of preserved synorogenic sediments (Figure 3).

The South Pyrenean Unit is made up of three thin-skinned thrust sheets (from south to north, the Sierras Marginales, Montsec and Bóixols; see Figure 3), which have been emplaced in an outward-propagating deformation sequence on top of a shallow décollement located in Upper Triassic evaporites (Muñoz, 1992). The Bóixols thrust was activated during the Maastrichtian (from approximately 70-65 Ma), as indicated by the overlying syntectonic sequences. Deformation stepped onto the Montsec thrust during the Ypresian (around 55 Ma). Finally, the

Sierras Marginales unit was activated between the Early and Late Eocene (50-40 Ma). The outward propagation of deformation was interrupted during the last (Late Eocene) stage of the thrust belt evolution by break-back reactivation of the older thrusts and by the development of new, minor out-of-sequence thrusts (Capote et al., 2002). The northern fault contact of the Bóixols thrust sheet is the Morreres backthrust, which has been interpreted as a passive-roof thrust (Muñoz, 1992).

The antiformal stack of the Axial Zone involves upper to middle crustal rocks and consists of three basement thrust sheets: Nogueres, Orri and Rialp. These units were initially separated by extensional faults before the onset of thrusting (Muñoz, 1992). The uppermost of the three units is the highly eroded Nogueres thrust sheet; its frontal tip is preserved in the southern limb of the antiformal stack, known as the Nogueres Zone, while its root-zone crops out in the northern part of the Axial Zone (Muñoz, 1992). The Nogueres unit has been thrusted over the Orri unit between the Late Cretaceous and the Early Eocene (90-50 Ma) before deformation stepped onto another Mesozoic extensional fault, causing the Orri unit to overthrust the Rialp unit during the Middle to Late Eocene (50-36 Ma). Finally, deformation shifted again to create the Rialp thrust sheet between the Middle Eocene and the Late Oligocene (36-20 Ma) (Capote et al., 2002).

North of the Axial Zone in the North Pyrenean Unit, very steep, north-vergent thrust sheets and pop-up structures involve basement and Mesozoic cover rocks in both their foot- and hanging-walls. Most of the orogenic displacement in the North Pyrenean Unit occurred along the North Pyrenean Frontal Thrust, while the steep faults observed in the basement were probably not very active during the Pyrenean orogeny. They may represent either contractional Hercynian structures or younger, low-angle pre-Pyrenean fault zones (Capote et al., 2002). Since in the absence of preserved synorogenic sediments the timing of the deformation along the sub-vertical faults is very difficult to assess, the structural history of North Pyrenean Unit remains controversial (ECORS Pyrenees Team, 1988).

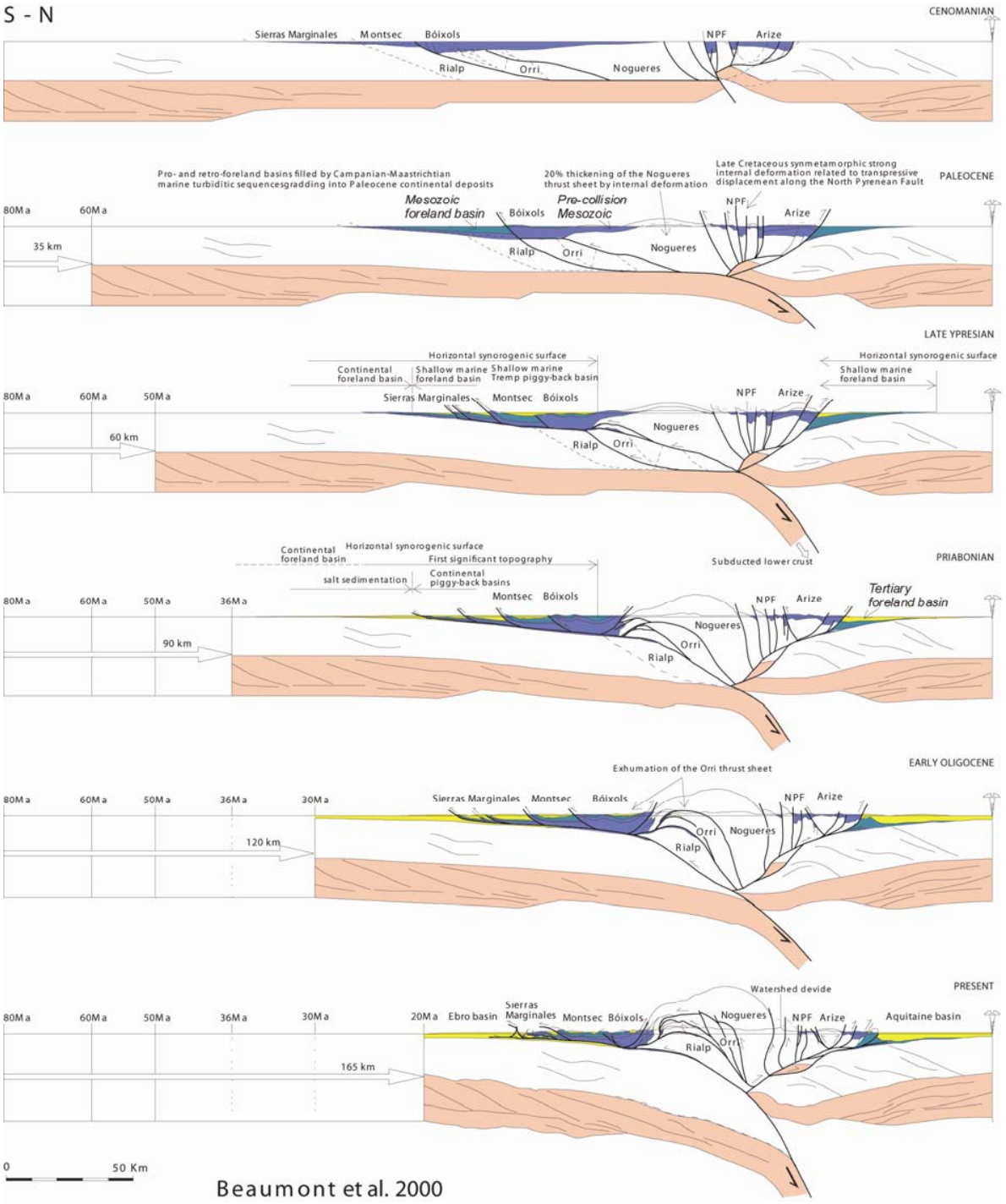

Figure 3 Balanced cross section restoration of the crust along the ECORS profile, showing the inferred evolution of the mountain belt since the onset of convergence in the Cenomanian (~80 Ma). Modified after Beaumont et al. (2000)

Modeling approach

To answer our research questions we have used a wide range of state-of-the-art numerical modeling tools. In Paper 1, we present a new method where we couple a structural-kinematic model and a thermo-kinematic model to evaluate the consistency of existing area-balanced section reconstructions with independent thermochronology data (figure 4). In Papers 2 and 3, we use two-dimensional lithospheric scale thermo-mechanical models coupled with simple surface process algorithms to study the effects of extensional inheritance and surface processes on mountain building.

Structural-kinematic modeling

The first component of the new method presented in Paper 1 is the structural-kinematic modeling software 2D-Move™ (Midland Valley Ltd). Using 2D-Move™, we can create a crustal-scale cross-section of our research area and model the effects of fault movements on the entire section. The aim of this exercise was to produce a set of velocity fields from a balanced cross-section restoration to describe its kinematics. A conventional section restoration, such as the one presented by Muñoz (1992) for the Central Pyrenees (Figure 3), consists of several time slices representing the structure of a crustal section at different times. Using the constraints derived from the section restoration on the timing and amount of displacement along the active faults, theoretically all the crustal blocks can be moved back gradually from their present position to their original pre-deformation position, with intermediate stages matching the partially restored sections.

2D-Move™ offers a range of algorithms suited for modeling hanging-wall deformation resulting from movement along a fault plane. We have tested the different available options, and decided to use the simple-shear algorithm in our case study as it proved to be capable of handling the geometric complexity of the modeled section. The algorithm predicts the deformation of the hanging-wall using the shape of the underlying fault while leaving the footwall undeformed (Withjack and Peterson, 1993). The deformation fulfills the condition of

volume conservation (or area conservation, in case of a 2D section assuming plane strain) and is calculated according to the 'velocity method' of Waltham and Hardy (1995).

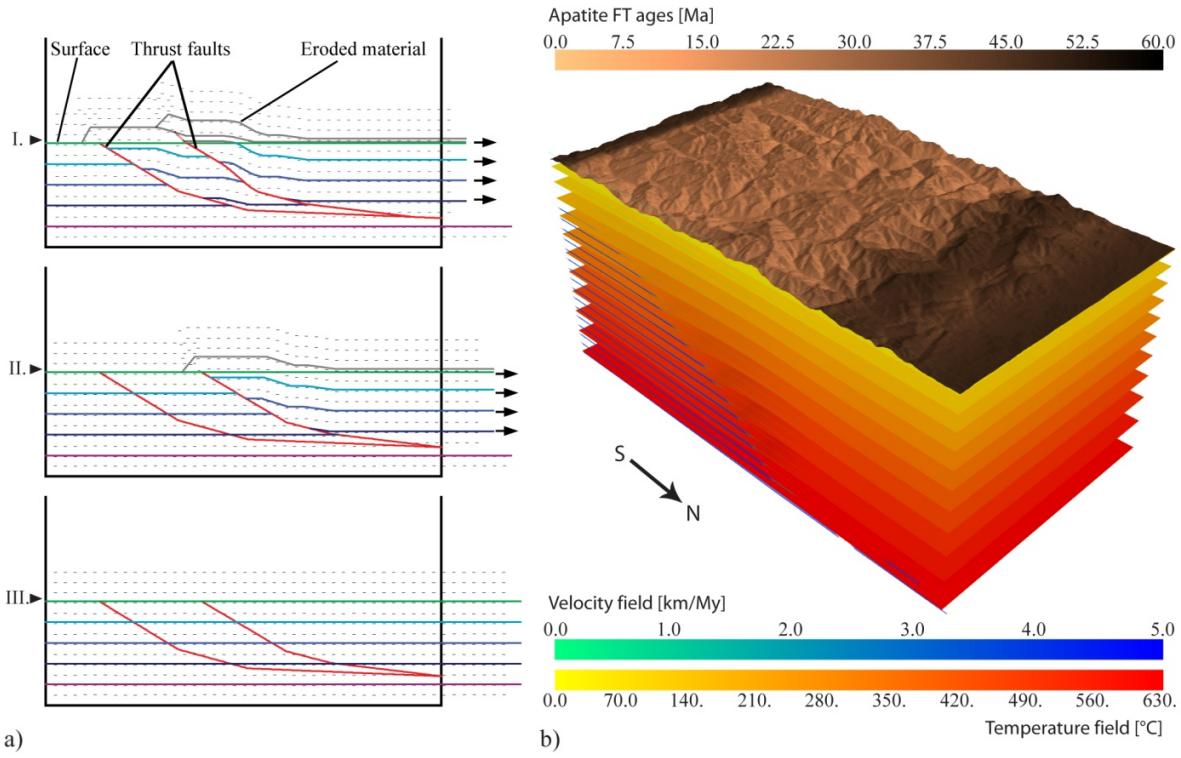

Figure 4 Principle of the method presented in Paper 1. **(a) Structural-kinematic component:** A velocity field is derived for each time interval of the modeled section restoration using 2D-Move™. A time interval is defined between two consecutive steps (e.g. I and II or II and III) of the restoration. In our synthetic example, the black cloud of points represents a Lagrangean marker field tracking the materials. **(b) Thermo-kinematic component:** The velocity fields are subsequently imported in the thermo-kinematic model PECUBE to predict thermochronometric ages for particles ending up on the surface of the model. These ages can be compared with sample ages obtained from the area.

In 2D-Move™ all fault motions must be applied sequentially. For any given step of the reconstruction the velocity field is calculated from the sum of all the individual fault-movements, therefore the order in which fault movements are applied within the step is inconsequential.

Since the simple-shear algorithm leaves the footwall of the active fault undeformed, the flexural-slip unfolding algorithm has been used to simulate the changes in the shape of the main crustal decollement from one time slice to the other. This algorithm divides the section

into thin vertical strips that can be freely translated along their boundaries in the vertical direction. With this method, a chosen horizon (in our case the main decollement on the present-day time slice) can be unfolded to a target line (in our case a line following the shape of the decollement on the pre-dating time slice). It is important to note that the flexural-slip unfolding algorithm also conserves area.

Thermo-kinematic modeling

The second component of the method presented in Paper 1 is the thermo-kinematic model PECUBE (Braun (2003); see also Braun et al. (2012)). The aim of the thermo-kinematic modeling component is to predict thermochronological ages in the study area and compare them to available observations by integrating the velocity fields derived from the structural-kinematic model into the thermo-kinematic modeling.

PECUBE is designed to solve the heat-transport equation in a three-dimensional crustal block submitted to a tectonic and topographic scenario. The code is based on a finite-element approach and derives the *time-temperature (t-T) paths* of individual rock particles ending up on the surface at the end of the model run. These *t-T paths* are subsequently used to compute apparent ages for a range of thermochronometers, using standard thermochronological age-prediction models (Braun et al., 2012).

The standard kinematic input for PECUBE consists, for each modeled time-step, of a fault geometry and the velocities of the hanging- and footwall with respect to the fault [cf. Braun et al. (2012)]. We have implemented a new input option where a set of velocity vectors derived from the structural-kinematic model can be used for modeling the tectonic scenario of each time-step. These two-dimensional input velocity fields are extrapolated in the third dimension, normal to the section, to allow direct comparison with the observed thermochronological data and correctly take into account the influence of topography.

The thermochronometric ages are predicted from the time-temperature histories of rock particles using forward kinetic models (Braun et al., 2012).

For further details on the coupling of the structural-kinematic and thermo-kinematic models, and the limitations of the new method we refer to the Methodology and Limitations sections of Paper 1.

Thermo-mechanical modeling

In Papers 2 and 3 we use a modified version of the Arbitrary Lagrangean-Eulerian finite-element thermo-mechanical code FANTOM (Thieulot, 2011) to study the effects of surface processes and extensional inheritance on the structural development of contractional orogens and their foreland basins.

FANTOM is designed to model thermally coupled, plane-strain, incompressible viscous-plastic creeping flows in the crust and upper mantle. When the stress is below the yield criterion, the deformation is viscous while when the stress exceeds the yield criterion the deformation is frictional-plastic. In case of viscous deformation, the effective viscosity η_{eff} is specified as:

$$\eta_{eff} = fA^{-1/n}\ \dot{\varepsilon}^{(1-n)/2n}\ exp\left(\frac{Q+Vp}{nRT}\right)$$

where *A* is the pre-exponential scaling factor, *n* is the power-law exponent, $\dot{\varepsilon}$ is the second invariant of the deviatoric strain rate tensor, *Q* is activation energy, *V* is activation volume, *p* is pressure, *T* is temperature, and *R* is the universal gas constant. Values for *A*, *n*, *Q* and *V* are derived from laboratory measurements. The factor *f* is used to scale viscosities calculated from the reference 'wet' quartzite flow law. Frictional-plastic yielding occurs when:

$$(J_2')^{1/2} = p\ sin\phi_{eff} + \ C\ cos\phi_{eff}$$

Where J_2' is the second invariant of the deviatoric stress, ϕ_{eff} is the effective internal angle of friction given as $psin(\phi_{eff}) = (p\text{-}p_f)sin(\phi)$ for pore fluid pressure p_f , and *C* is cohesion. With appropriate choice of *C* and ϕ_{eff}, this yield criterion can approximate the effect of pore fluid pressure and frictional sliding in rocks. The effect of strain softening is introduced by a linear decrease of the internal angle of friction from 15° to 2° and by a simultaneous decrease of cohesion from 20 MPa to 4 MPa. The initial temperature field is laterally uniform and includes

radioactive heat production in the crust. The thermal and mechanical systems are fully coupled and solved sequentially at each time-step. The implemented surface processes comprise optional elevation-dependent erosion and full sedimentation below a fixed base level. For detailed model setup, used parameter values and the description of the surface process algorithms we refer to the methodology sections of Papers 2 and 3. The modified version of this code solves the resulting systems of equations in parallel, allowing for the solution of a larger number of unknowns then hitherto. The numerical models have unprecedented high resolution and allow us to study the link and interaction between thin-skinned deformation in the sediments and crustal scale deformation.

Summary of papers

Paper 1

Erdős, Z., **van der Beek, P.**, and **Huismans, R. S.**
Evaluating balanced section restoration with thermochronology data: a case study from the Central Pyrenees
Tectonics, 33, doi:10.1002/2013TC003481

In this study, we propose a new method that can be used to quantitatively evaluate the consistency of a balanced cross-section restoration with independent thermochronology data that constrain spatial and temporal patterns of exhumation. To achieve this, we use the structural-kinematic software 2D-Move™ to constrain a set of velocity fields that describe the kinematics of the cross-section. Using these velocity fields as input for the thermo-kinematic code PECUBE, we can predict the thermal history and a range of thermochronometric ages for any location in the modeled area. Finally we can quantitatively compare the predicted thermochronometric ages with the available independent thermochronology data.

We present our method through a case study of a crustal-scale balanced cross-section restoration of the Central Pyrenees, presented by Muñoz (1992) and Beaumont et al. (2000). This cross-section restoration is exceptionally well constrained and supported by a wide variety of geological and geophysical data. Moreover, an extensive thermochronological dataset has

been collected independently from the area. Our results show that the section restoration is consistent to a first order with both low- and high-temperature thermochronology data collected in the last two decades from the study area. Moreover, the data provide additional constraints on the timing of individual thrusting events, the thermal structure of the crust and the post-orogenic topographic evolution of the mountain belt. The high-temperature (zircon fission-track and K-feldspar Ar-Ar) data constrain the thermal structure of the belt as well as the timing of underplating while the low-temperature (apatite fission-track and (U-Th)/He) data require late synorogenic sedimentary burial of the southern flank of the Pyrenees between Late-Eocene (40 Ma) to Late-Miocene (9 Ma) times, consistent with previous inferences (Coney et al., 1996), and imply that no such burial occurred on the northern flank. The presented case study demonstrates the validity of this new approach.

Paper 2

Erdős, Z., **Huismans, R. S.**, and **van der Beek, P.**
First order control of syntectonic sedimentation on crustal-scale structure of mountain belts
Submitted to *Earth and Planetary Science Letters*

The idea of a potentially strong coupling between surface processes and mountain building has been extensively discussed in the last decades. The strong localizing feedback of erosion on the orogenic hinterland and the effect of sedimentation on the shallow structures of foreland fold-and-thrust belts have been extensively studied in recent years, but the governing forces of basement deformation below the foreland remain poorly constrained. In this paper, we offer a novel hypothesis that is consistent with observations from a range of orogens around the globe. Using high-resolution plain-strain thermo-mechanical models coupled with a simple sedimentation algorithm we show that syntectonic sedimentation has a controlling effect on the style of basement deformation in mountain belts and below their adjacent foreland fold-and-thrust belts. We present numerical model experiments exploring the effect of different sedimentation and erosion rates. Through these model experiments, we identify two end members that we term “sediment-loaded” and “sediment-starved” orogens, and we propose that they account for the primary characteristics of orogenic forelands.

Sediment-starved orogens such as the Urals (Brown et al., 1997a; 1997b), display short, narrowly spaced basement thrust-sheets with relatively small displacement along the individual basement thrusts in the orogenic core. In the presence of pre-orogenic sediments and a décollement layer the orogen is flanked by short thin-skinned thrust-sheets in the foreland with no or limited basement deformation below the foreland. In contrast, sediment-loaded orogens, such as the Swiss Alps (Roure, 2008), display long basement thrust-sheets penetrating the basement below thick foreland basin deposits with a large amount of displacement along the individual thrusts. As a result of basement involvement in the foreland, the orogenic wedge is significantly wider. The pre- to synorogenic deposits of the foreland fold-and-thrust belt deform by long thin-skinned thrust-sheets. Furthermore, the presented models suggest that while erosion strongly affects the width of the orogenic hinterland, it has limited direct effects on the evolution of the orogenic foreland.

We present a simple analytical scaling analysis that suggests a quadratic dependence of basement thrust spacing on syntectonic sediment thickness. A comparison of the results of our analysis with a compilation of basement thrust-sheet length and synorogenic sediment thickness data from a range of orogenic examples yields good correlation. Natural examples from the Urals, the Swiss Alps and the Zagros, and the data compilation also demonstrate that our modelling results are to a first order consistent with natural observations.

Paper 3

Erdős, Z., **Huismans, R. S.**, and **van der Beek, P.**
Extensional inheritance and surface processes as controlling factors of mountain belt structure
Submitted to *Journal of Geophysical Research*

Surface processes and inherited structures are widely regarded as factors that strongly influence the evolution of mountain belts around the world. The first order effects of these parameters have been studied extensively throughout the last decades, but their relative importance remains notoriously difficult to estimate.

In this paper we use lithospheric-scale plane-strain thermo-mechanical models to study the effects of surface processes and inherited extensional structures on orogenic wedges and their adjacent foreland basins. Surface processes are modeled with the combination of an elevation-dependent erosion model and a simple sedimentation algorithm, where all topography is filled up to a prescribed reference level. The inherited extensional structures are generated explicitly by forward modeling the formation of an extensional basin, before inverting the velocity boundary conditions to model convergent mountain building. We also present an additional sensitivity test investigating the effect of varying upper-crustal strength.

Our results show that sedimentation increases the length scale of both the thin-skinned and thick-skinned thrust-sheets, facilitating the building of a wider orogen, while erosion helps to localize deformation, promoting narrowing of the orogen. Extensional inheritance facilitates basement deformation in the retro-wedge, increasing the width of the orogen. Additionally, the sensitivity test shows that a weaker than average upper crust results in a wider orogen with lower, plateau-like topography.

We have compared the modeled behaviors to the High Atlas, the Pyrenees and the Western Alps, three well studied natural examples, characterized by different inversional stages to confirm the observed controls of surface processes and extensional inheritance on the orogenic structure. We find that the crustal structure at different stages of the models presented in this study show good correlation with structural features observed in these mountain belts.

Conclusions

Surface processes and mountain building

The models presented in Papers 2 and 3 demonstrate that syntectonic sedimentation results in longer basement thrust sheets as well as longer thin-skinned thrust sheets and a generally wider orogen. The main deformation zone cutting through the upper crust remains active for a longer time, accommodating more displacement while subsequent new basement thrusts form further out below the foreland, creating longer thrust sheets. In the presence of inherited extensional structures, this effect can be observed in the retro-wedge as well as the pro-wedge, although the thrust-sheets developing in the former are consistently shorter than those developing in the latter. Our models also confirm the results of Fillon et al. (2012), who have shown that syntectonic sedimentation increases the characteristic length of thin-skinned thrust sheets.

Conversely to the effects of syntectonic sedimentation, as erosion removes material from the internal part of the orogen, it tends to narrow the wedge and reduce the orogenic loading of the colliding plates, therefore limiting the space available for deposition in the flexural foreland deeps. The presented models also demonstrate that although, as expected, erosion promotes a narrower orogen, the lengthening effect of sedimentation on both the thin-skinned and the basement thrust sheets remains largely unaffected.

Extensional inheritance and mountain building

The models presented in Paper 3 demonstrate that inherited extensional structures play a crucial role in mountain building as they facilitate the migration of deformation into the undeformed basement of the overriding plate. Moreover, a significant amount of lower-crustal/mantle-lithospheric material is preserved at shallow depths only in the presence of extensional inheritance, but significant erosion is needed in order to bring this material to the surface.

Examining the model behavior in contractional mode after subjecting the model to various amounts of extension showed that above a certain point, increasing the amount of extension and hence the number of inherited extensional structures does not affect the overall structural style of deformation heavily. The initial keystone structure (i.e. a triangular crustal block uplifted in the early phase of convergence along a pair of conjugate thrust faults, with foreland depressions developing on either side of the structure) becomes somewhat larger and more complex when the extensional mode is run to full crustal break-up but the general features remain largely unaffected.

Interaction of thin-skinned and thick-skinned tectonics

Both the purely contractional and the "accordion" (i.e. the model subjected to an initial extensional phase before inverting the boundary conditions in order to explicitly model the inversion of extensional structures) models presented in Papers 2 and 3 show that thin-skinned thrust sheets are generally rooted in the footwall of basement thrusts as they form outward-propagating sequences. As soon as a new basement thrust forms, the thin-skinned sequence situated on top of the new basement thrust-sheet is abandoned in favor of starting a new sequence in the footwall of the new thrust.

The thin-skinned thrusts forming ahead of the basement deformation in the foreland do not control the locus of the basement deformation migrating into the foreland. The position of the new basement thrust is primarily determined by the thickness of the syntectonic sediments covering the foreland basin.

Consistency of the ECORS cross-section restoration with thermochronology data

Using the structural-kinematic modelling software 2D-Move™ it was possible to reproduce the section restoration with high accuracy up to the 36-Ma time slice and with limited accuracy up to the 50-Ma time slice. However it was not possible to reproduce the restoration beyond the 50-Ma time slice due to a combination of inaccuracies and inconsistencies arising from the hand-drawn sections, and an indicated 20% internal thickening of the Nogueres basement

thrust-sheet (i.e. large scale internal deformations cannot be reproduced by the structural-kinematic model).

The thermochronometric ages predicted by the thermo-kinematic modelling are generally in good agreement with both the high- and low-temperature thermochronology data available in the Central Pyrenees; hence we conclude that the restoration is to a first order consistent with these datasets.

The effects of surface processes on the Pyrenean orogeny

As demonstrated by the modeling exercise presented in Paper 1 the predicted thermochronological ages approximate the available low-temperature thermochronology data better by taking into account the late-stage burial and re-excavation scenario affecting the southern flank of the Pyrenean wedge presented by Coney et al. (1996), and quantified by Fillon and van der Beek (2012). This suggests that late-stage syntectonic sedimentation played a crucial role in the formation of the Pyrenean pro-wedge causing the out of sequence reactivation of faults in the foreland fold-and-thrust belt (Fillon et al., 2013).

The effects of extensional inheritance on the Pyrenean orogeny

The balanced-section restoration presented by Muñoz (1992) and Beaumont et al. (2000) displays slow accommodation of displacement along the North Pyrenean Frontal Thrust, which brought a lower-crustal body to shallow depth below the North Pyrenean Unit. Within the North Pyrenean Unit, which shows no evidence of synorogenic sedimentation, several high-angle faults can be found accommodating very little displacement. These faults involve basement and Mesozoic cover rocks in both their foot- and hanging-walls and they are thought to be inverted pre-Pyrenean extensional structures (Capote et al., 2002).

These characteristic features can only be observed in those thermo-mechanical models that have an accordion setup (for example see model M1 in Paper 3). The pure contractional models display very little overall deformation in the retro-wedge, which is dominated by a small keystone structure characterized by the absence of significant internal deformation. In contrast,

when the model is exposed to an extensional phase before contraction, a significant part of the retro-wedge is made up by a significantly larger keystone-structure that includes a lower-crustal root and a well-defined internal structure characterized by inverted normal faults.

In conclusion, our model experiments suggest, that extensional inheritance played a prime role in the structural evolution of the Pyrenees, with the major characteristics of the North Pyrenean Unit, including the presence of steep, inverted normal faults, the relative tectonic quiescence of the area after the early inversion and the presence of a lower-crustal body at shallow depth below the unit, best recaptured by our accordion models.

Future perspectives

We have used multiple modeling approaches to study the controlling effects of surface processes and extensional inheritance on mountain building, with a special focus on the Pyrenean orogeny.

The method developed in Paper 1 has a number of crucial limitations. Most of these are limitations of the applied structural-kinematic model and its algorithms. The improvement of these algorithms (e.g. more robust results when using complex geometries, inclusion of isostatic compensation) is outside our scope but, nevertheless, it could substantially contribute to the method as a whole.

A potential next step could be to further elaborate the thermo-kinematic modeling component so that it would allow for more efficient comparison of competing section restorations. Furthermore, developing an algorithm to easily identify potential areas along section from where the collection of additional data would help distinguishing between the compared restorations would also be beneficial.

In the work presented in Papers 2 and 3, the surface-process algorithms coupled to the thermo-mechanical models are very simple in design, to allow studying the first-order effects exerted by these forces on the orogen. To uncover more intricate relationships the application of a more sophisticated, internally consistent, mass-balancing topographic evolution model is required.

Moreover, we have only investigated the effect of sedimentation in contractional mode, after the development of significant topography. This limitation is necessitated by the fact that the applied simple sedimentation model is not limited in the input of material into the models hence it is not applicable in situations where there is not enough topography to serve as a source for large amounts of sediments. The coupling of an internally consistent surface evolution model with FANTOM would allow us to study the effect of surface processes both in the extensional and the inversion modes.

Regarding the effects of extensional inheritance, we have used explicitly modeled, but very basic inherited structures. The matter could be further investigated with the use of more complex geometries such as adjacent rift basins.

Previously Allken et al. (2013) have shown, using the 3D variant of FANTOM, that rift interactions are best studied in three-dimensional setup. Hence an obvious next step would be to expand our models into the third dimension.

References

Allken, V., Huismans, R.S., Fossen, H., Thieulot, C., 2013. 3D numerical modelling of graben interaction and linkage: a case study of the Canyonlands grabens, Utah. Basin Research 25, 436-449.

Beaumont, C., Fullsack, P., Hamilton, J., 1992. Erosional control of active compressional orogens, in: McClay, K.R. (Ed.), Thrust Tectonics. Chapman & Hall, London, pp. 1-18.

Beaumont, C., Fullsack, P., Hamilton, J., 1994. Styles of Crustal Deformation in Compressional Orogens Caused by Subduction of the Underlying Lithosphere. Tectonophysics 232, 119-132.

Beaumont, C., Kamp, P.J.J., Hamilton, J., Fullsack, P., 1996. The continental collision zone, South Island, New Zealand: Comparison of geodynamical models and observations. Journal of Geophysical Research 101, 3333-3359.

Beaumont, C., Munoz, J.A., Hamilton, J., Fullsack, P., 2000. Factors controlling the Alpine evolution of the central Pyrenees inferred from a comparison of observations and geodynamical models. Journal of Geophysical Research 105, 8121-8145.

Bonnet, C., Malavieille, J., Mosar, J., 2007. Interactions between tectonics, erosion, and sedimentation during the recent evolution of the Alpine orogen: Analogue modeling insights. Tectonics 26.

Braun, J., 2003. Pecube: a new finite-element code to solve the 3D heat transport equation including the effects of a time-varying, finite amplitude surface topography. Comput Geosci 29, 787-794.

Braun, J., van der Beek, P., Valla, P., Robert, X., Herman, F., Glotzbach, C., Pedersen, V., Perry, C., Simon-Labric, T., Prigent, C., 2012. Quantifying rates of landscape evolution and tectonic processes by thermochronology and numerical modeling of crustal heat transport using PECUBE. Tectonophysics 524, 1-28.

Brown, D., Alvarez-Marron, J., Perez-Estaun, A., 1997a. Preservation of a subcritical wedge in the south Urals foreland thrust and fold belt. J Geol Soc London 154, 593-596.

Brown, D., Alvarez-Marron, J., Perez-Estaun, A., Gorozhanina, Y., Baryshev, V., Puchkov, V., 1997b. Geometric and kinematic evolution of the foreland thrust and fold belt in the southern Urals. Tectonics 16, 551-562.

Buck, W.R., 1991. Modes of Continental Lithospheric Extension. Journal of Geophysical Research 96, 20161-20178.

Buck, W.R., Lavier, L.L., Poliakov, A., 1999. How to make a rift wide. Philosophical Transactions of the Royal Society A: Mathematical, Physical and Engineering Sciences 357, 671-693.

Buiter, S.J.H., 2012. A review of brittle compressional wedge models. Tectonophysics 530-531, 1-17.

Capote, R., Muñoz, J.A., Simon, J.L., Liesa, C.L., Arlegui, L.E., 2002. Alpine tectonics I: the Alpine system north of the Betic Cordillera, in: Gibbon, W., Moreno, T. (Eds.), The Geology of Spain. The Geological Society, London, pp. 367-400.

Coney, P.J., Munoz, J.A., McClay, K.R., Evenchick, C.A., 1996. Syntectonic burial and post-tectonic exhumation of the southern Pyrenees foreland fold-thrust belt. J Geol Soc London 153, 9-16.

DeCelles, P.G., Robinson, D.M., Quade, J., Ojha, T.P., Garzione, C.N., Copeland, P., Upreti, B.N., 2001. Stratigraphy, structure, and tectonic evolution of the Himalayan fold-thrust belt in western Nepal. Tectonics 20, 487-509.

ECORS Pyrenees Team, 1988. The ECORS deep reflection seismic survey across the Pyrenees. Nature 331, 508–511.

Ellis, S., Beaumont, C., Jamieson, R.A., Quinlan, G., 1998. Continental collision including a weak zone: the vise model and its application to the Newfoundland Appalachians. Can J Earth Sci 35, 1323-1346.

Fillon, C., Huismans, R.S., van der Beek, P., 2012. Syntectonic sedimentation effects on the growth of fold-and-thrust belts. Geology 41, 83-86.

Fillon, C., Huismans, R.S., van der Beek, P., Muñoz, J.A., 2013. Syntectonic sedimentation controls on the evolution of the southern Pyrenean fold-and-thrust belt: Inferences from coupled tectonic-surface processes models. Journal of Geophysical Research 118, 5665-5680.

Fillon, C., van der Beek, P., 2012. Post-orogenic evolution of the southern Pyrenees: constraints from inverse thermo-kinematic modelling of low-temperature thermochronology data. Basin Research 24, 418-436.

Gehrels, G., DeCelles, P., Martin, A., Ojha, T.P., Pinhassi, G., Upreti, B.N., 2003. Initiation of the Himalayan orogen as an early Paleozoic thin-skinned thrust belt. GSA Today.

Huismans, R.S., Beaumont, C., 2003. Symmetric and asymmetric lithospheric extension: Relative effects of frictional-plastic and viscous strain softening. Journal of Geophysical Research 108.

Huismans, R.S., Beaumont, C., 2011. Depth-dependent extension, two-stage breakup and cratonic underplating at rifted margins. Nature 473, 74-78.

Huismans, R.S., Buiter, S.J.H., Beaumont, C., 2005. Effect of plastic-viscous layering and strain softening on mode selection during lithospheric extension. Journal of Geophysical Research 110.

Jamieson, R.A., Beaumont, C., 2013. On the origin of orogens. Geological Society of America Bulletin 125, 1671-1702.

Jammes, S., Huismans, R.S., 2012. Structural styles of mountain building: Controls of lithospheric rheologic stratification and extensional inheritance. Journal of Geophysical Research 117.

Mouthereau, F., 2003. Rheology and strength of the Eurasian continental lithosphere in the foreland of the Taiwan collision belt: Constraints from seismicity, flexure, and structural styles. Journal of Geophysical Research 108.

Mouthereau, F., Tensi, J., Bellahsen, N., Lacombe, O., De Boisgrollier, T., Kargar, S., 2007. Tertiary sequence of deformation in a thin-skinned/thick-skinned collision belt: The Zagros Folded Belt (Fars, Iran). Tectonics 26.

Mouthereau, F., Watts, A.B., Burov, E., 2013. Structure of orogenic belts controlled by lithosphere age. Nature Geoscience 6, 785-789.

Mugnier, J.L., Baby, P., Colletta, B., Vinour, P., Bale, P., Leturmy, P., 1997. Thrust geometry controlled by erosion and sedimentation: A view from analogue models. Geology 25, 427-430.

Muñoz, J.A., 1992. Evolution of a continental collision belt: ECORS Pyrenees crustal balanced cross section, in: McClay, K.R. (Ed.), Thrust Tectonics. Chapman & Hall, New York, pp. 235-246.

Muñoz, J.A., Martinez, A., Verges, J., 1986. Thrust Sequences in the Eastern Spanish Pyrenees. Journal of Structural Geology 8, 399-405.

Puigdefabregas, C., Muñoz, J.A., Marzo, M., 1986. Thrust belt development in the eastern Pyrenees and related depositional sequences in the southern foreland basin, in: Allen, P.A., Homewood, P. (Eds.), Foreland basins. International Association of Sedimentologists Special Publication, pp. 229-246.

Puigdefabregas, C., Muñoz, J.A., Verges, J., 1992. Thrusting and foreland basin evolution in the southern Pyrenees, in: McClay, K. (Ed.), Thrust Tectonics. Chapman & Hall, London, pp. 247-254.

Roest, W.R., Srivastava, S.P., 1991. Kinematics of the Plate Boundaries between Eurasia, Iberia, and Africa in the North-Atlantic from the Late Cretaceous to the Present. Geology 19, 613-616.

Rosenbaum, G., Lister, G.S., Duboz, C., 2002. Relative motions of Africa, Iberia and Europe during Alpine orogeny. Tectonophysics 359, 117-129.

Roure, F., 2008. Foreland and Hinterland basins: what controls their evolution? Swiss Journal of Geosciences 101, 5-29.

Schmid, S.M., Kissling, E., 2000. The arc of the western Alps in the light of geophysical data on deep crustal structure. Tectonics 19, 62-85.

Simoes, M., Avouac, J.P., Beyssac, O., Goffé, B., Farley, K.A., Chen, Y.-G., 2007. Mountain building in Taiwan: A thermokinematic model. Journal of Geophysical Research 112.

Stolar, D.B., Willett, S.D., Roe, G.H., 2006. Climatic and tectonic forcing of a critical orogen. Geological Society of America Special Paper 398, 241-250.

Storti, F., Mcclay, K., 1995. Influence of Syntectonic Sedimentation on Thrust Wedges in Analog Models. Geology 23, 999-1002.

Thieulot, C., 2011. FANTOM: Two- and three-dimensional numerical modelling of creeping flows for the solution of geological problems. Physics of the Earth and Planetary Interiors 188, 47-68.

Vissers, R.L.M., Meijer, P.T., 2012. Iberian plate kinematics and Alpine collision in the Pyrenees. Earth-Sci Rev 114, 61-83.

Waltham, D., Hardy, S., 1995. The velocity description of deformation. paper 1: theory. Marine and Petroleum Geology 12, 153-163.

Whipple, K.X., 2009. The influence of climate on the tectonic evolution of mountain belts. Nature Geoscience 2, 97-104.

Willett, S., Beaumont, C., Fullsack, P., 1993. Mechanical Model for the Tectonics of Doubly Vergent Compressional Orogens. Geology 21, 371-374.

Willett, S.D., 1999. Orogeny and orography: The effects of erosion on the structure of mountain belts. Journal of Geophysical Research 104, 28957-28981.

Withjack, M.O., Peterson, E.T., 1993. Prediction of Normal-Fault Geometries - a Sensitivity Analysis. Aapg Bulletin-American Association of Petroleum Geologists 77, 1860-1873.

Part II
Papers

Paper I

Evaluating balanced section restoration with thermochronology data: a case study from the Central Pyrenees

Zoltán Erdős[1,2], Peter van der Beek[2], and Ritske S. Huismans[1]

1. Department of Earth Science, University of Bergen

2. Institut des Sciences de la Terre, Université Joseph Fourier

Corresponding author: Zoltán Erdős, University of Bergen, N-5007 Bergen, Norway

(zoltan.erdos@geo.uib.no)

Citation:
Erdős, Z., P. van der Beek, and R. S. Huismans (2014), Evaluating balanced section restoration with thermochronology data: A case study from the Central Pyrenees, Tectonics, 33, 617–634, doi:10.1002/2013TC003481.

Key Points

A method to evaluate section restorations with thermochrone data is proposed

The method is presented through the case of the Pyrenean ECORS cross-section

We propose the method to be applicable in other geological settings

Abstract

We present a new method that can be used to quantitatively evaluate the consistency between balanced section restorations and thermochronological datasets from orogenic belts. We have applied our method to a crustal-scale area-balanced cross-section restoration along a profile in the Central Pyrenees. This restoration is well constrained and supported by a wide variety of geological and geophysical data. Moreover, an extensive thermochronological dataset has been collected independently in the area. We use the structural-kinematic software 2D-Move™ to constrain a set of velocity fields that describes the kinematics of the Central Pyrenees. Using these velocity fields as input for the thermo-kinematic code PECUBE, we derive predictions of the thermal history and a range of thermochronometric ages for the modeled area. We find that the kinematic history of the belt as inferred from section balancing is in good agreement with the published thermochronological data. High-temperature (zircon fission-track and K-feldspar Ar-Ar) data constrain the thermal structure of the belt as well as the timing of underplating. Low-temperature (apatite fission-track and (U-Th)/He) data require late syn-orogenic sedimentary burial of the southern flank of the Pyrenees between Late-Eocene (40 Ma) to Late-Miocene (9 Ma) times, consistent with previous studies, and imply that no such burial occurred on the northern flank.

Index terms and Keywords

Thermochronology, Continental contractional orogenic belts and inversion tectonics, Tectonics and landscape evolution,

Balanced section restoration, Structural-kinematic modeling, Thermo-kinematic modeling, Age-elevation profiles, Time-temperature paths

1. Introduction

Crustal-scale balanced cross-section restorations synthesize our knowledge about the structural-kinematic history of a mountain belt. Although the method had been used previously, the basic principles of creating a balanced cross section were thoroughly discussed for the first time by Dahlstrom (1969). Crustal-scale restorations require understanding not just the present-day geology and the history of the area in question, but also the processes acting on the deep structures as well as those playing a role in the formation of topography. The synthesis of all available geological and geophysical data is essential to allow maximum constraint on the restoration. Section restorations based on deep seismic profiles have been published for the Alps (e.g. Roure et al., 1996; Schmid et al., 1996), the Canadian Rocky Mountains (e.g. Cook et al., 1992) and the Pyrenees (e.g. Muñoz, 1992; Séguret & Daigniéres, 1986) while, more recently, restorations based mainly on geologic data have been compiled for the Andes (e.g. McQuarrie, 2002; McQuarrie et al., 2008) and the Himalaya (e.g. DeCelles et al., 2001; Long et al., 2011; Robinson et al., 2006), among others.

Additional and independent constraints on orogen kinematics are provided by thermochronology data, which record exhumation of rocks in response to tectonic thickening,

rock uplift and erosion (e.g., Braun et al., 2006; Reiners and Brandon, 2006). Such data can therefore, in principle, be used to discriminate between competing kinematic models for orogens (e.g., Herman et al., 2010; Robert et al., 2011) or to provide additional temporal constraints on balanced section restorations (e.g., Long et al., 2012; McQuarrie et al., 2008). Conversely, the kinematics implied by such restorations can be used to predict thermal history and thermochronologic age patterns in, for instance, foreland fold-and-thrust belts (Lock and Willett, 2008; ter Voorde et al., 2004).

However, these two approaches to decipher orogen kinematics generally remain detached from each other and no quantitative, internally consistent framework exists as yet to fully integrate the two. In this study, we propose such a methodology and quantitatively evaluate the consistency of a balanced cross-section restoration of the central Pyrenees, based on Muñoz (1992) and Beaumont et al. (2000), with independent thermochronological data for a range of systems with different closure temperatures. The central Pyrenees constitute an ideal test case to validate our methodology, as the existing balanced cross-section is well constrained by a wide range of geological and geophysical data but does not incorporate the more recently collected extensive thermochronological database (see details and references in the next section). The method can be applied to other orogenic belts where fewer constraints exist to evaluate the consistency of proposed cross-section restorations with available thermochronology data or to provide additional temporal constraints on such restorations.

2. Geological setting

2.1. The Pyrenean orogen

The Pyrenees (Figure 1) are a collisional orogen formed by Late-Cretaceous (90 Ma) to Early-Miocene (20 Ma) convergence between the Iberian and European plates (Roest and Srivastava, 1991; Rosenbaum et al., 2002; Vissers and Meijer, 2012). According to these plate-kinematic analyses, the convergence rate reached its peak during the Eocene to Oligocene (50-20 Ma). The range is dominated by inversion tectonics (Muñoz et al., 1986) owing to thrusting along pre-existing extensional structures (Figure 2). These structures were originally formed during Triassic to Cretaceous rifting and transtension associated with anticlockwise rotation of the Iberian plate with respect to Europe and consequent opening of the Bay of Biscay (Roest and Srivastava, 1991; Rosenbaum et al., 2002).

The asymmetrical Pyrenean orogen resulted from northward underthrusting of the Iberian crust below the European crust, resulting in a wide southern pro-wedge and a narrower northern retro-wedge (Figure 2). In the centre of the belt, the Axial Zone comprises a south-vergent antiformal stack of upper-crustal thrust sheets (Muñoz, 1992). The Axial Zone is flanked by the South Pyrenean Unit towards the south and the North Pyrenean Unit towards the north, respectively. The South Pyrenean Unit is a fold-and-thrust belt consisting of Mesozoic and Cenozoic sedimentary rocks, while in the North Pyrenean Unit, basement and cover rocks form north-vergent thrust sheets and pop-up structures (Muñoz, 1992; Capote et al., 2002). The Pyrenees are flanked by the Ebro and the Aquitaine foreland basins towards the south and north, respectively (Figures 1 and 2).

Our study-area is located in the central Pyrenees, along the ECORS deep seismic profile (ECORS Pyrenees Team, 1988) (Figure 1). Although we have used the entire section to constrain the velocity fields in the structural-kinematic model, the thermo-kinematic models cover only the Axial Zone and the North Pyrenean Unit, as the bulk of the published thermochronological data has been collected in these areas.

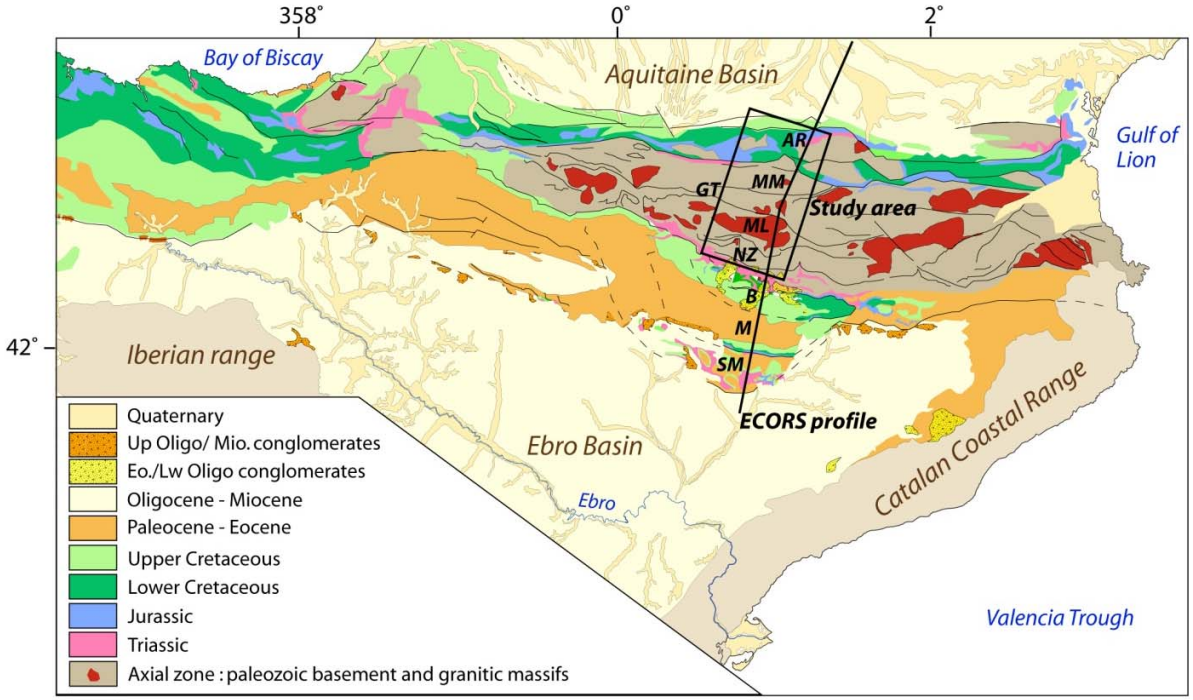

Figure 1. Geological map of the Pyrenees. The black line represents the ECORS deep seismic profile along which the balanced cross section of Figure 2 was constructed, and the box indicates the boundaries of the thermo-kinematic model. AR: Arize block, MM: Marimaña massif, ML: Maladeta massif, NZ: Nogueres Zone, GT: Gavarnie-thrust B: Bóixols, M: Montsec, SM: Sierras Marginales (redrawn after Fillon and van der Beek, 2012).

2.2. Structural evolution of the Pyrenees

The kinematics are well constrained in the South Pyrenean Unit as the tectonic evolution is exceptionally well recorded by syntectonic sediments (e.g. Muñoz, 1992; Puigdefabregas et al., 1986, 1992; Vergés and Muñoz, 1990). The evolution of the Axial Zone has been inferred from

correlation of its thrust sheets with those in the South Pyrenean Unit, while that of the North Pyrenean Unit is less well constrained.

The South Pyrenean Unit is made up of three thin-skinned thrust sheets (from south to north, the Sierras Marginales, Montsec and Bóixols; Figure 2), which have been emplaced on top of a detachment located in Upper Triassic evaporites in a southward-propagating deformation sequence (Muñoz, 1992). The Bóixols thrust was activated during the Maastrichtian (from ~70-65 Ma), as indicated by the overlying syn-tectonic sequences. Deformation stepped onto the Montsec thrust during the Ypresian (~55 Ma). Finally, the Sierras Marginales unit was activated between the Early and Late Eocene (50-40 Ma). The forward propagation of deformation in the South Pyrenean Unit was modified during the last (Late Eocene) stage of the thrust belt evolution by break-back reactivation of the older thrusts and by the development of new, minor out-of-sequence thrusts, possibly in response to rapid accumulation of syntectonic sediments (Capote et al., 2002; Fillon et al., 2013). The northern fault contact of the Bóixols thrust sheet is the Morreres backthrust, which has been interpreted as a passive-roof thrust (Muñoz, 1992).

The antiformal stack of the Axial Zone involves upper to middle crustal rocks and consists of three thrust sheets: Nogueres, Orri and Rialp (Figure 2). These units were initially juxtaposed and separated by extensional faults before the onset of thrusting (Muñoz, 1992). The highly eroded Nogueres thrust sheet is the uppermost of the three units. Its frontal tip has been preserved in the southern limb of the antiformal stack and is known as the Nogueres Zone, while its root-zone crops out in the northern part of the Axial Zone (Muñoz, 1992).

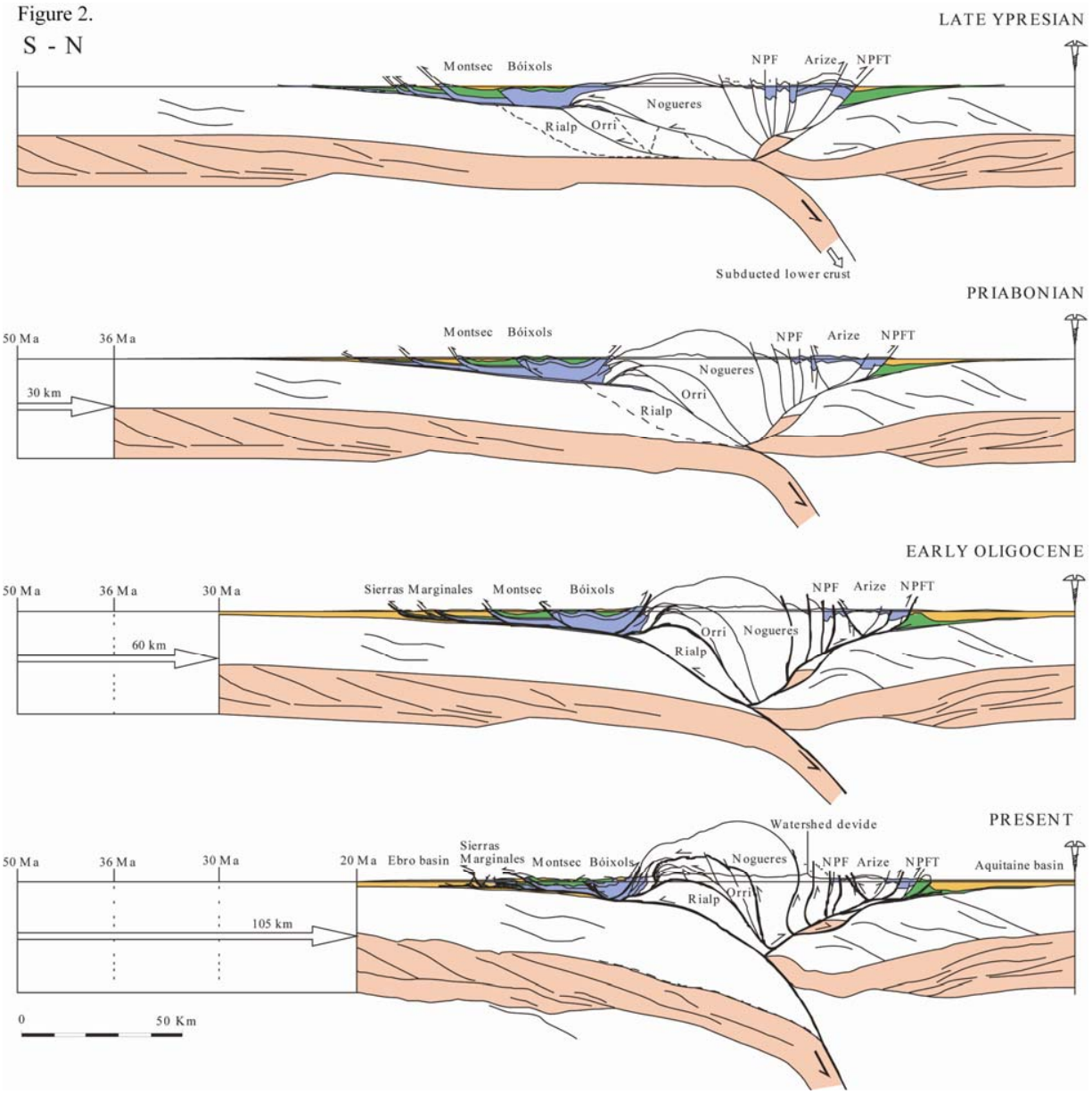

Figure 2. Four time slices (between 50 Ma and Present) of the crustal-scale area-balanced cross-section restoration of the Central Pyrenees along the ECORS deep-seismic profile by Muñoz (1992) and Beaumont et al. (2000). NPF: North Pyrenean Fault; NPFT: North Pyrenean Frontal Thrust. Figure modified from Beaumont et al. (2000).

Thrusting of the Nogueres unit over the Orri unit took place between the Late Cretaceous and the Early Eocene (90-50 Ma). Deformation subsequently stepped onto another Mesozoic extensional fault, causing the Orri unit to overthrust the Rialp unit during the Middle to Late

Eocene (50-36 Ma). Finally, deformation shifted again to create the Rialp thrust sheet between the Middle Eocene and the Late Oligocene (36-20 Ma) (Capote et al., 2002; Metcalf et al., 2009).

North of the Axial Zone in the North Pyrenean Unit, very steep, north-vergent thrust sheets and pop-up structures involve basement and Mesozoic cover rocks in both their foot- and hanging-walls. Most of the orogenic displacement in the North Pyrenean Unit occurred along the North Pyrenean Frontal Thrust, while the steep faults observed in the basement were probably not strongly reactivated during the Pyrenean orogeny. They may represent either contractional Hercynian structures or younger, extensional pre-Pyrenean fault zones (Capote et al., 2002). As the timing of the deformation along the sub-vertical faults is very difficult to assess, the structural history of North Pyrenean Unit remains controversial (ECORS Pyrenees Team, 1988).

2.3. Thermochronology data

Altogether, 74 published thermochronometric ages have been used from 48 different locations to test the predictions of the thermo-kinematic models: 40 apatite fission-track (AFT) ages, 27 apatite (U-Th)/He (AHe) ages, 4 zircon fission-track (ZFT) ages and 3 time-temperature models extracted from K-feldspar $^{40}Ar/^{39}Ar$ degassing experiments (Fitzgerald et al., 1999; Gibson et al., 2007; Metcalf et al., 2009; Sinclair et al., 2005). The samples were collected along two age-elevation profiles in the Maladeta massif, one profile in the Barruera block, one profile in the Marimaña massif, and one profile in the Lacourt massif (Figures 1 and 3). Individual samples were also collected from the Nogueres zone along the southernmost edge of the Axial Zone. The Maladeta and Barruera profiles are located in the Orri thrust sheet, whereas the Marimaña profile is located in the Nogueres thrust sheet, in the hanging-wall of the Gavarnie thrust

(Figure 1). The Nogueres samples come from the southern frontal zone of the Nogueres thrust sheet. The Lacourt profile is located within the southern part of the Arize block (Figure 3) and is the only profile located in the North Pyrenean Unit. The samples in the Maladeta, Barruera, Marimaña and Lacourt profiles were collected from Hercynian granitic plutons while the samples in the Nogueres Zone are from Cambrian to Triassic volcanic rocks.

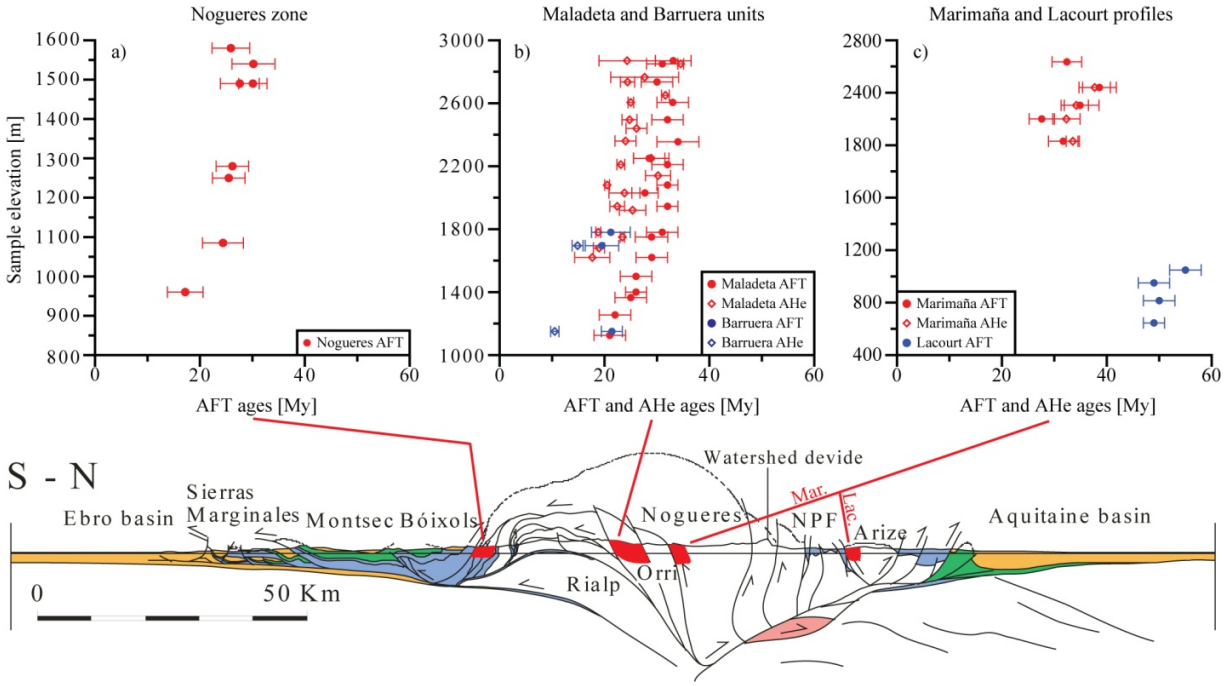

Figure 3. Apatite fission track and apatite (U-Th)/He ages along the ECORS deep seismic profile published by Fitzgerald et al. (1999), Sinclair et al. (2005), Gibson et al. (2007) and Metcalf et al. (2009), plotted together on age-elevation plots (section modified from Beaumont et al., 2000). Error bars for AHe and AFT ages represent 1-σ error. Note the different elevation scales.

The profiles line up along two different trends (Figure3). The Nogueres, Barruera, Maladeta and Marimaña profiles show an almost vertical age-elevation trend at elevations above 1500 m, suggesting rapid exhumation around 30-40 Ma (e.g. Fillon and van der Beek, 2012; Fitzgerald et al., 1999; Sinclair et al., 2005). The lower-elevation samples of these profiles line up along a gentler slope on the age-elevation plots, suggesting decreased erosion rates from 30 Ma to

around 20 Ma. The Lacourt profile spans only a few hundred meters of relief and does not show a clear age-elevation relationship; AFT ages for these samples are 50-55 Ma, significantly older than those from the other profiles.

The Barruera profile is located very close to the western Maladeta profile, but both the AFT and the AHe samples yield systematically younger ages than samples in the Maladeta profile from similar elevations. The significance and the cause of this difference are not yet fully understood. Recently, Rushlow et al. (2013) have suggested that a late stage of focused denudation affected the southern flank of the Axial Zone in response to either disturbance of the critical taper by syntectonic sedimentation in the South Pyrenean Unit or a regional climate shift.

Samples in the Marimaña profile that provided both AFT and AHe ages yielded AHe ages that are within uncertainty of or slightly older than the respective AFT ages (Gibson et al., 2007); this is also the case for some of the Maladeta profile samples reported by these authors. The significance of these ages also remains unclear; they might have been affected by either minute (U-Th)-rich inclusions or implantation of He from surrounding minerals, but could also indicate extremely rapid cooling through both the AFT and AHe closure temperatures. We have therefore chosen to include all available data in the dataset that we will compare to our forward model predictions.

Metcalf et al. (2009) modeled time-temperature paths from K-feldspar $^{40}Ar/^{39}Ar$ thermochronometry in the Maladeta Pluton. Three analyzed samples yielded similar thermal histories, showing a heating phase until around 40 - 50 Ma, interpreted as due to tectonic burial beneath the Nogueres thrust-sheet in the footwall of the Gavarnie thrust, before rapid exhumational cooling. The K-feldspar $^{40}Ar/^{39}Ar$ models do not constrain the end of exhumation

as the lowest-temperature $^{40}Ar/^{39}Ar$ step yielded an age of ~20 Ma (Metcalf et al., 2009). The peak burial temperature for the two lower-elevation samples is around 280 °C, while for the highest elevation sample it is around 175 °C. The latter estimate is, however, probably less well constrained as it is at the lowermost end of the sensitivity of the K-feldspar $^{40}Ar/^{39}Ar$ thermochronometer (Metcalf et al., 2009).

Sinclair et al. (2005) published four ZFT ages – one from the Nogueres, Barruera, Maladeta and Marimaña massifs each – that range from 49.3 ± 2.6 Ma to 159 ± 33 Ma, implying that total exhumation since 50 Ma (the starting time of our thermo-kinematic models) was not sufficient to bring rocks with fully reset ZFT ages to the surface.

3. Methodology

The proposed method links a two-dimensional structural-kinematic restoration model with a three-dimensional thermo-kinematic model that is capable of predicting cooling ages for a range of thermochronometers (Figure 4). We use velocity fields derived from the structural-kinematic model to advect material in the thermo-kinematic model. This allows us to predict thermochronometric ages and compare them quantitatively with the available observations. Our method is somewhat similar to the approach presented by Lock and Willett (2008), who aimed to predict low-temperature thermochronometric ages in fold-and-thrust belts, although our thermo-kinematic and age-prediction models are significantly more elaborate.

3.1. Calculating velocity fields

A conventional section restoration, such as the one presented by Muñoz (1992) for the Central Pyrenees (Figure 2), consists of several time slices representing the structure of a crustal

section at different times. Extracting kinematics from such a restoration requires tracking particle paths from one time slice to another, which can be achieved by quantitative structural-kinematic modeling packages. As the geological and geophysical constraints on the restoration of the section only apply to the present-day, we have chosen to carry out the structural-kinematic modeling starting with this section. Our starting point is thus a model representing the present state of the section that we created using the structural-kinematic modeling software 2D-Move™ (Midland Valley Ltd).

Figure 4.

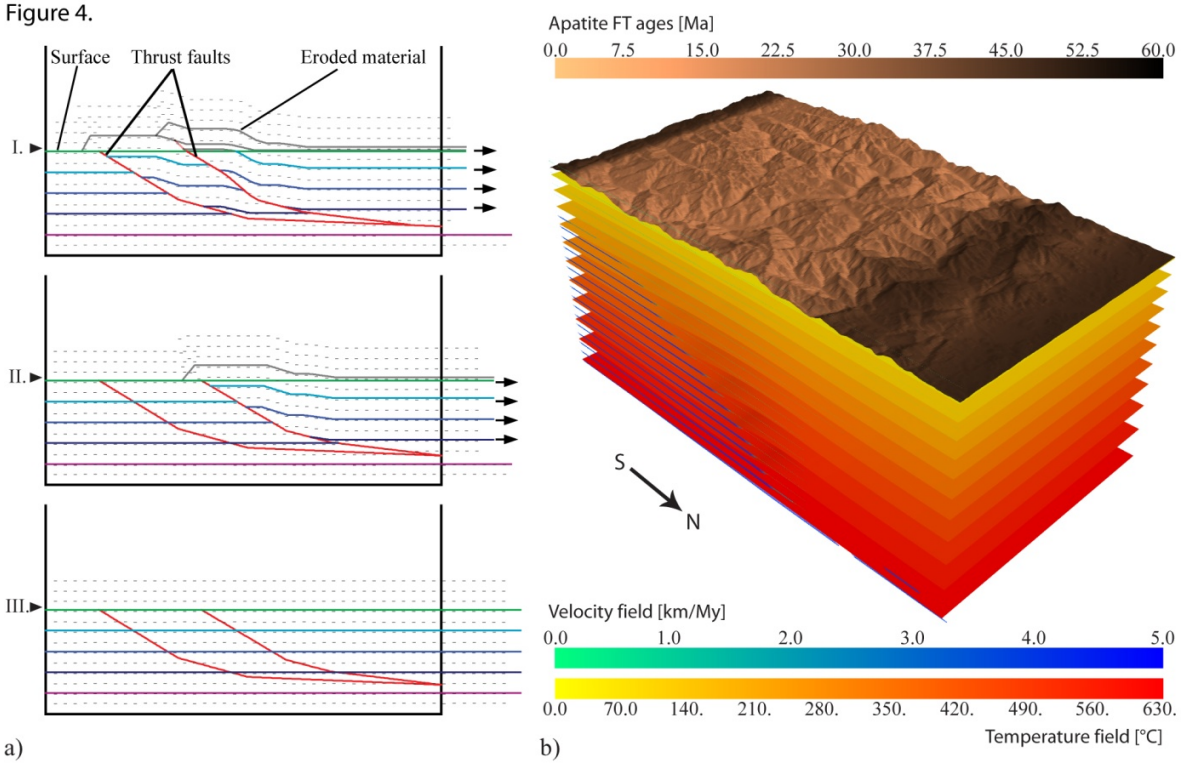

Figure 4. Principle of the method. **(a)** A velocity field is derived for each time interval of the modeled section restoration using 2D-MoveTM. A time interval is defined between two consecutive steps (e.g. I and II or II and III) of the restoration. In our synthetic example, the black cloud of points represents a Lagrangean marker field tracking the materials. **(b)** The velocity fields are subsequently imported in the thermo-kinematic model PECUBE to predict thermochronometric ages for particles ending up on the surface of the model. These ages can be compared with sample ages obtained from the area.

Using the constraints derived from the section restoration on the timing and the amount of displacement along the active faults, all the crustal blocks can be moved from their position on any particular time slice to their position on the time slice directly pre-dating it. In theory, this procedure can be repeated for an indefinite number of time slices.

In 2D-Move, the deformation within hanging-wall beds resulting from movement over a fault plane can be modeled using various algorithms. We have tested the different available options, but only the simple-shear algorithm proved to be capable of handling the geometric complexity of our model. The algorithm predicts the deformation of the hanging-wall using the shape of the underlying fault while leaving the footwall undeformed (Withjack and Peterson, 1993). The deformation fulfills the condition of volume conservation (or area conservation, in case of a 2D section assuming plane strain) and is calculated according to the 'velocity method' (Waltham and Hardy, 1995). This method provides the rate and direction of particle movement in a model calculated with the 'isogon method' of Waltham (1989) and shifts the points of the model accordingly (ter Voorde et al., 2004). An alternative option available in 2D-Move is the fault-parallel flow algorithm, which is a more appropriate choice for the reconstruction of individual units within a compressional setting, as it is designed to kinematically model geological structures in the hanging wall where deformation is accommodated by fault-parallel shear (Egan et al., 1999). However, our aim was to model the section reconstruction as a whole and the fault-parallel flow algorithm is less suitable for this purpose as it operates with angular shear (also known as back shear) to maintain constant bed thickness, which creates significant deformation in the far field (see Egan et al., 1999 and references therein).

The input parameters of the simple-shear algorithm are the amount of displacement, the direction of movement along the active fault and the angle of the applied shear. In 2D-Move, movements along different faults cannot be applied simultaneously, which means that all fault motions must be applied sequentially. The order in which fault movements are applied within any particular step of the reconstruction is inconsequential.

Since the simple-shear algorithm leaves the footwall of the active fault undeformed, the flexural-slip unfolding algorithm has been used to simulate the changes in the shape of the main crustal decollement from one time slice to the other. This algorithm divides the section into thin vertical strips that can be freely translated along their boundaries in the vertical direction. With this method, a chosen horizon (in our case the main decollement on the present-day time slice) can be unfolded to a target line (in our case a line following the shape of the decollement on the pre-dating time slice). It is important to note that the flexural-slip unfolding algorithm conserves area.

We have consistently used the simple-shear algorithm with vertical shear direction, as that is the simplest and most reliable option available in 2D-Move. In this setup the displacement isogons (lines joining points with identical displacement vectors) are vertical (Waltham, 1989). This means that the hanging-wall is deformed as if it was cut into thin, vertical columns and translated on top of the undeforming footwall. For the simple-shear algorithm to work properly, the active fault has to extend all the way below the hanging-wall. Since the decollement depicted on the reconstruction of Figure 2 ends in a steep subduction zone, it has been smoothly transitioned in our model into a horizontal fault deep in the mantle.

As the deformation of the hanging-wall depends on the shape of the active fault below, the extension of the decollement below the northern part of the section induces undesired deformation of the hanging wall north of the S-point. To restore this deformation we have used the flexural-slip unfolding algorithm. The 0-m elevation line of the starting time slice is tracked along with the modeled horizons. After resolving all fault-related deformation, we have used this 0-m elevation line as the unfolding horizon. The target horizon is a smooth downwards-convex line, representing the material eroded during the time interval in question. It is defined so that the area enclosed by this line and the 0-m elevation line of the target time slice is equal to the measured difference in area of the upper crust between the starting and the target time slices. The exact shape of the target line is picked to achieve the best geometrical match between the model and the target restoration (Figure 2).

Tracking of particle motion within the crustal blocks is achieved by the introduction of a marker cloud with unique identifiers for each point in the cloud. These markers are advected along with the material through time. A displacement vector can be derived from the starting and final position of each marker point for each time interval (i.e. the time spent between two subsequent time slices). Subsequently a velocity field can be created for each time interval by dividing the resulting displacement vectors by the length of the time interval. Note that this approach may lead to velocity fields that largely simplify particle paths within blocks that are moving along curved faults.

A detailed description of the structural-kinematic modeling carried out on the case study of the Central-Pyrenees is provided in the Supplementary Information.

3.2. Thermo-kinematic modeling

The result of the structural-kinematic modeling consists of a set of velocity fields, each describing the deformation pattern for one time interval of the section restoration. These velocity fields serve as input for the thermo-kinematic model PECUBE (Braun, 2003; see also Braun et al., 2012).

PECUBE is designed to solve the three-dimensional heat-transport equation in a crustal block submitted to a specific tectonic and topographic scenario. The code uses a finite-element approach to derive the time-temperature ($t - T$) paths of individual rock particles ending up at the surface at the end of the model run. These $t - T$ paths are subsequently used to compute apparent ages for a range of thermochronometers, using standard thermochronological age-prediction models (Braun et al., 2012).

We have implemented a new feature in PECUBE so that it can use a set of velocity fields as input files for the calculation of particle paths. The standard kinematic input for PECUBE consists, for each modeled time-step, of a fault geometry and the velocities of the hanging- and footwall with respect to the fault (cf. Braun et al., 2012). We have replaced this input by a set of velocity vectors derived from the structural-kinematic model for each time-step. The two-dimensional velocity fields derived from the structural-kinematic modeling are extrapolated in the third dimension, normal to the section, to allow direct comparison with the observed thermochronological data and correctly take into account the influence of topography.

Since the calculated $t - T$ paths are highly sensitive to surface topography, the predicted thermochronological ages will be affected by the implemented topographic evolution scenario

(Braun, 2002; Braun et al., 2006). The influence of the surface topography is strongest for thermochronometric systems characterized by low closure temperatures (e.g. apatite fission-track and (U-Th)/He systems; Braun et al., 2006). Since the paleotopography of a mountain belt is extremely difficult to determine, it is common practice to use the present-day surface topography throughout the modeled time-period, thereby supposing topographic steady state (e.g. Herman et al., 2010; Robert et al., 2011; Whipp et al., 2007). In case this simplification is not sufficient, PECUBE includes a set of options allowing simple parametric amplification or reduction of the topography (e.g. Glotzbach et al., 2011; Valla et al., 2010). Basic sedimentation scenarios can also be implemented (Fillon and van der Beek, 2012). These options enable testing different topographic evolution scenarios for the same set of velocity fields. In our models, we have used a digital elevation model of the present-day surface topography downgraded to a resolution of 300 m. The crustal blocks and the deposits have spatially uniform material properties, typical for the continental crust (Table 1). For a more detailed description of the use of PECUBE we refer the reader to Braun (2003) and Braun et al. (2012).

Parameter	Value
Crustal density	2700 kg m^{-3}
Model thickness	35 km
Thermal diffusivity	25 km^2 Myr^{-1}
Basal temperature	570 °C; 600 °C; **630 °C**
Sea-level temperature	15 °C
Atmospheric lapse rate	4 °C km^{-1}
Crustal heat production	0.8 µW m^{-3}; **0.95 µW m^{-3}**

Table 1. Reference thermal and kinematic parameters used in PECUBE modeling. Bold values for basal temperature and crustal heat production those used in the reference model and are set to obtain a surface heat flow of 70 mW m^{-2} and a corresponding geothermal gradient of 33 °C km^{-1} (e.g. Fernandez and Banda, 1989; Fernandez et al., 1998; Fillon and van der Beek, 2012).

3.3. Thermochronometric age predictions

PECUBE predicts thermochronometric ages from the time-temperature histories of rock particles using forward kinetic models (Braun et al., 2012). Apatite (U-Th)/He (AHe) ages are

predicted using the numerical scheme presented in Wolf et al. (1998) and the kinetic parameters proposed by Farley (2000). Apatite (AFT) and zircon (ZFT) fission-track ages can be predicted using several different models and parameterizations. For AFT ages, we have used the model presented by Green et al. (1989) with kinetic parameters modified by Stephenson et al. (2006), while for the ZFT system we have used the annealing model of Galbraith and Laslett (1997) with the annealing parameters proposed by Rahn et al. (2004). We acknowledge that more elaborate models exist both for AFT and AHe age predictions (e.g. Flowers et al., 2009; Gautheron et al., 2009; Ketcham et al., 2007), which take into account compositional controls on annealing/diffusion rates. However, as Fillon and van der Beek (2012) pointed out previously, the characteristics of the observational dataset justify the use of the simpler age-prediction models. In particular, for the AHe data Gibson et al. (2007) and Metcalf et al. (2009) reported effective uranium concentrations of a few tens of ppm, which is within the range where the kinetic parameters of Farley (2000) can be used (Flowers et al., 2009; Gautheron et al., 2009). As concerns the AFT data, Gibson et al. (2007) Metcalf et al. (2009) and Sinclair et al. (2005) reported kinetic indicators close to that of Durango apatite, on which the kinetic parameters of Stephenson et al. (2006) have been calibrated. Moreover, the rapid cooling inferred from the age-elevation profiles (cf. Section 2.3) will minimize any compositional effects on the AFT and AHe ages.

To evaluate the consistency of the restoration with the observed data, predicted thermochronological ages at the sampling location are extracted by interpolation and are compared to the observed ages. An objective function that takes into account the error on the observed ages allows quantifying the fit between the predicted and observed ages (Glotzbach

et al., 2011). The resolution with which the input parameters of the forward models are constrained could, in principle, be assessed by inverse modeling (cf. Braun et al., 2012; Glotzbach et al., 2011; Valla et al., 2010), but these require running large numbers of individual forward models with slightly varying parameters, which is not possible in this case due to the complexity of the structural-kinematic model.

For the available K-feldspar $^{40}Ar/^{39}Ar$ data, we have used the thermal histories predicted by multi-diffusion domain modeling presented in Metcalf et al. (2009). We compare these *t – T* paths qualitatively to the *t – T* paths extracted from our PECUBE models.

4. Results

4.1. Structural-kinematic modeling results

The objective of the structural-kinematic modeling was to reproduce the section restoration presented by Muñoz (1992), in order to verify that it can be quantitatively balanced and to derive a set of velocity fields describing the movement of the crustal blocks through time.

The results of the modeling are compared with the original restoration in Figure 5. The model matches the restoration well for the 30-Ma and the 36-Ma time slices, except for the detailed geometry of the Axial-Zone thrust sheets discussed below, but for the 50-Ma time slice the mismatch becomes significant. The Muñoz (1992) restoration implies internal deformation of the Orri thrust-sheet between 36 Ma and 50 Ma, thinning and elongating it significantly during retrodeformation. As a result, our model requires less convergence for the restoration of the Orri thrust-sheet than the original reconstruction. Moreover, the Muñoz (1992) restoration implies 20% thickening of the Nogueres thrust sheet by internal deformation between 50 Ma

and 60 Ma. Due to the accumulation of internal deformation and the uncertainties arising from the drawing method, such as the small changes in the area of crustal blocks, we could not restore the section beyond its 50-Ma state.

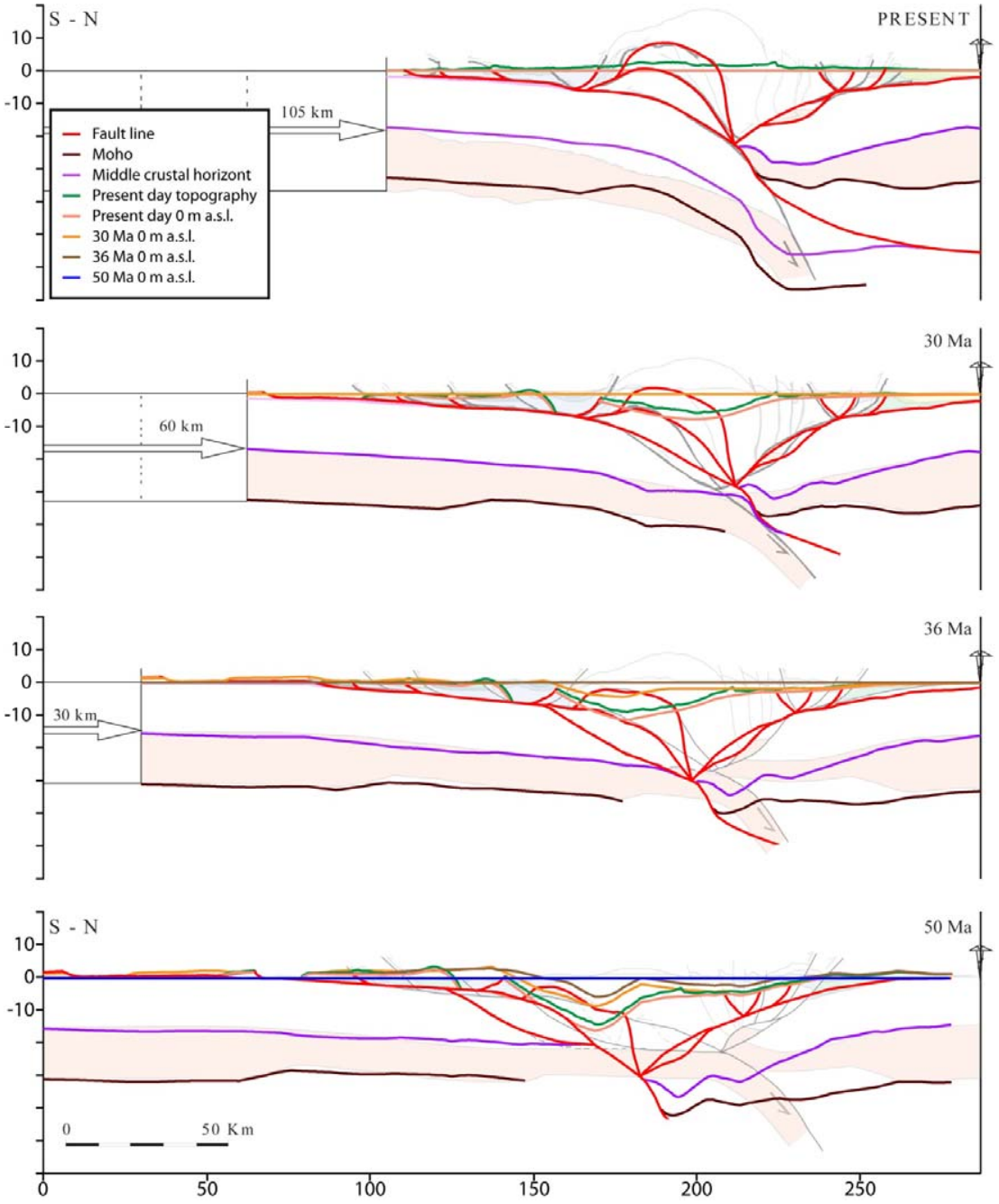

Figure 5. Result of the structural-kinematic modeling using 2D-Move™ for the same four time slices as shown in Figure 2. For comparison, the resulting crustal-scale geometry is plotted on top of the section restoration by *Muñoz* (1992) and *Beaumont et al*. (2000).

4.2. Thermo-kinematic modeling results

All the presented thermo-kinematic models utilize the same set of displacement fields derived from the structural-kinematic modeling. Material and thermal properties used in the thermo-kinematic modeling are given in Table 1. The *t – T* paths predicted for the locations of K-feldspar $^{40}Ar/^{39}Ar$ samples are plotted together with the *t – T* histories inferred by Metcalf et al. (2009) in Figure 6, while the predicted AFT and AHe ages are plotted together with the observed ages in age-elevation plots (Figures 7 and 9).

4.3. Reference model

In the reference model, the present-day topography is kept constant through time, while adopted thermal parameters were the same as those used previously by Fillon and van der Beek (2012).

The reference model does not predict reset ZFT ages in the Nogueres and Marimaña massifs but the two samples from the southern side of the Orri thrust-sheet (from the Maladeta and Barruera units) have predicted ages of ~46 Ma, in contrast to observed ages of 49 and 104 Ma, respectively (Sinclair et al., 2005); the model therefore predicts these to have cooled from somewhat too high temperatures.

The *t – T* paths corresponding to the K-feldspar $^{40}Ar/^{39}Ar$ samples record rapid exhumation between 50 Ma and 20 Ma (Figure 6). The calculated *t – T* paths fit reasonably for the two lower-elevation samples (PY55 and PY56) matching the peak burial temperature, while for the third sample (PY63), the predicted peak burial temperature is much higher than that extracted from the original data.

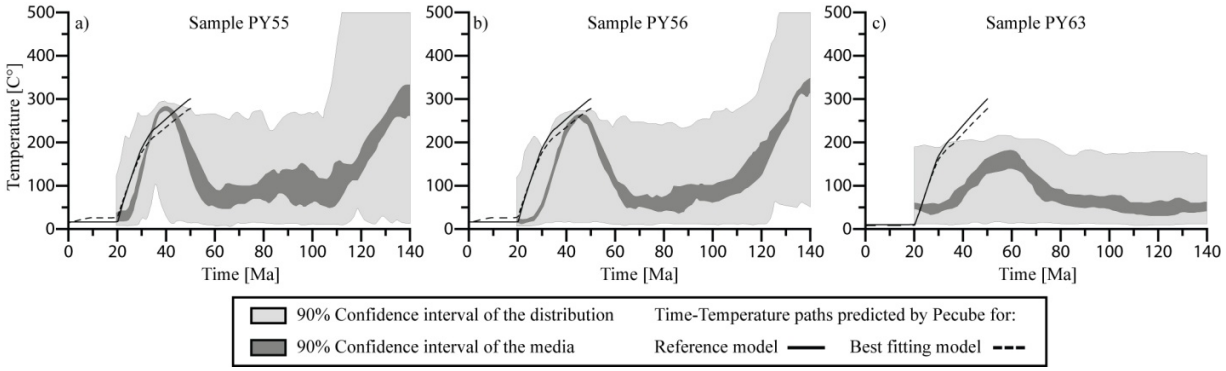

Figure 6. Predicted *t – T* paths plotted against the *t – T* paths inferred by *Metcalf et al*. (2009) from K-feldspar $^{40}Ar/^{39}Ar$ thermochronometry for three samples in the Maladeta unit (modified from *Metcalf et al*., 2009).

The AFT and AHe ages predicted by the reference model (Figure 7) for the profiles in the Axial Zone line up along sub-vertical trends and show ages between 33-27 Ma and between 26-22 Ma respectively, caused by very rapid exhumation. This rapid exhumation results from underplating of the Nogueres and Orri thrust-sheets by the Rialp thrust-sheet between 36 and 20 Ma (Fig. 5; cf. Supplementary Information for details). For the Lacourt profile, the reference model predicts AFT ages around 50 Ma; the samples in this area have been exhumed from shallow depths and are only partially reset.

While predicted AFT ages from the Nogueres block (Figure 7 a) are systematically older than the observed ages for the reference model, the predictions fit the Maladeta and Marimaña profile data reasonably well, especially for the samples taken from higher elevations (Figures 7 b, c). For the Lacourt profile, the AFT-age predictions also fit the observed ages well (Figure 7 c). Overall, 15 out of 40 AFT ages fit the observed ages to within 1σ-error, and 28 to within 2σ. The fit to the AHe data is less satisfactory, with only 8 out of 27 AHe ages fitted to within 1σ.The predictions of the reference model fit the higher-elevation AHe samples reasonably well but

they are systematically older than the observed ages for the lower-elevation samples (Figure 7 d). The predicted ages are significantly younger than the measured AHe ages from the Marimaña profile, as well as some from the East Maladeta profile reported in Gibson et al. (2007), suggesting that these data might be problematic (see also section 2.3).

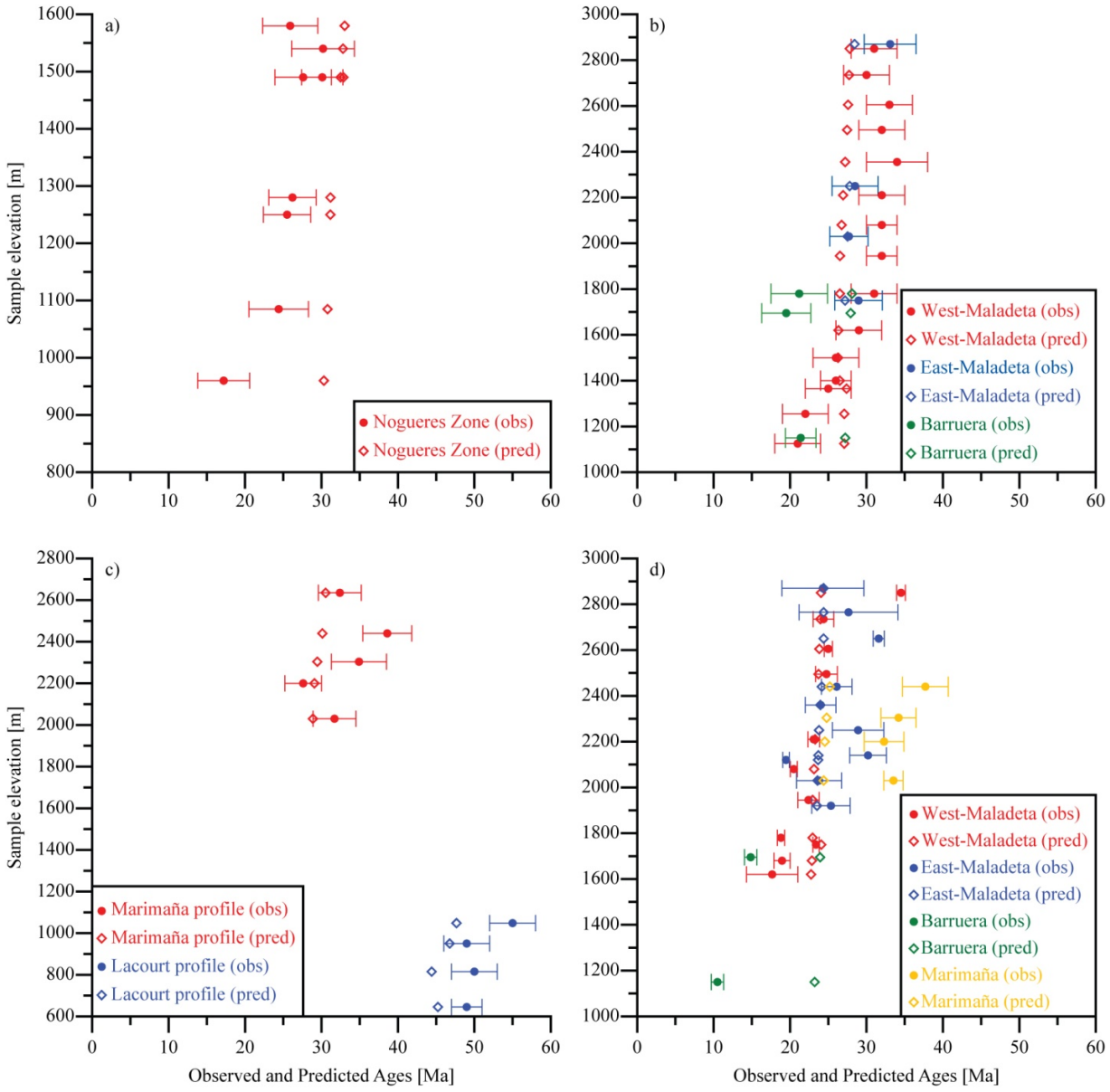

Figure 7. Comparison of predicted (solid symbols) and observed (open symbols with error bars) low-temperature thermochronologic ages for the reference model: **(a)** AFT data from the Nogueres Zone; **(b)** AFT data from Maladeta and Barruera; **(c)** AFT data from Marimaña and Lacourt; **(d)** AHe data from Maladeta and Barruera. See Figures 1 and 3 for locations of sampling profiles.

In summary, the reference model predicts exhumation from somewhat too high temperatures for the ZFT data and one K-feldspar $^{40}Ar/^{39}Ar$ sample, suggesting that it either overpredicts the amount of exhumation or that the adopted thermal structure is not optimal. It also systematically overpredicts AFT and AHe ages for the lower-elevation samples (with the exception of the Lacourt profile), while fitting the higher-elevation samples. This discrepancy may point to significant changes in topography between the active orogenic phase and the present day. We address both these issues in the following sections.

4.4. Parameter sensitivity analysis

We have carried out a simple sensitivity analysis to test whether we can improve the fit of the high-temperature (K-feldspar $^{40}Ar/^{39}Ar$ and ZFT) thermochronometers, while not deteriorating the fit of the low-temperature (AFT and AHe) thermochronometers. We have varied the crustal heat production and the basal temperature while keeping the surface heat flow and the corresponding geothermal gradient close to the present day values of 70 mW m^{-2} and 33°C km^{-1} measured in the foreland basins (e.g. Fernandez and Banda, 1989; Fernandez et al. 1998).

The time-temperature models extracted from K-feldspar $^{40}Ar/^{39}Ar$ degassing experiments by Metcalf et al. (2009) show an onset of rapid cooling at around 45 Ma rather than 50 Ma (Figure 6). To test whether this apparent misfit between the observed and predicted onset of exhumation can be reduced, we have also run a set of models where we have modified the starting time to be 45 Ma, while adjusting the velocities for the first phase accordingly.

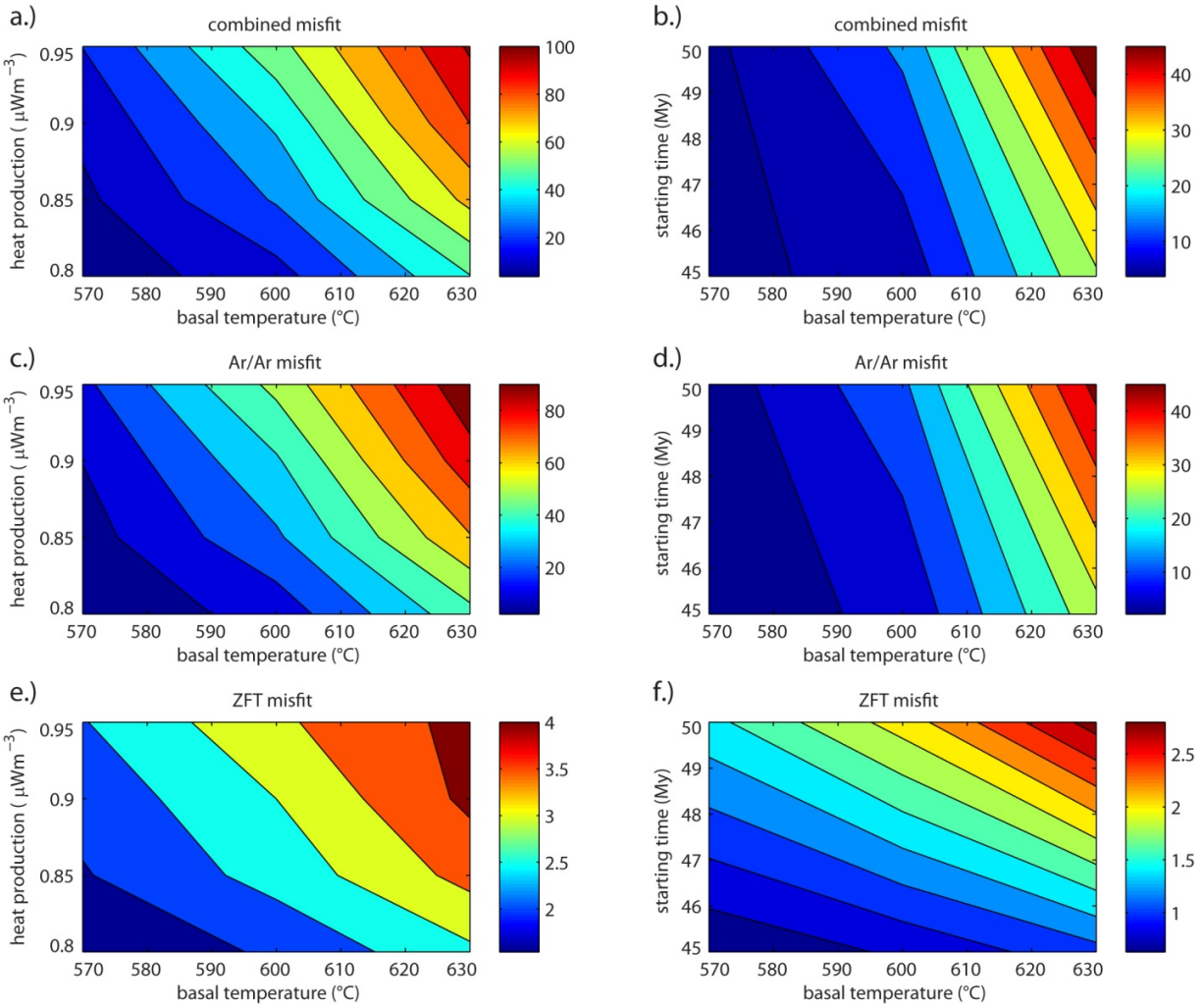

Figure 8. Contour plots showing the result of the sensitivity analysis as the misfit between observed and predicted thermochronologic ages according to Equation (1). **(a, b)** Combined high temperature data (K-feldspar $^{40}Ar/^{39}Ar$ and ZFT); (c, d) K-feldspar $^{40}Ar/^{39}Ar$ data only; **(e, f)** ZFT data only. Misfit is shown as function of basal temperature and heat production in plots (a, c, e) and as function of basal temperature and model starting time in plots (b, d, f).

To evaluate the difference between the modeled and observed ages quantitatively and thus find the best-fitting thermal parameters, we have used the objective function defined by Glotzbach et al. (2011):

$$\mu = \sum_{i=1}^{n} \left(\frac{m_i - o_i}{\sigma_i} \right)^2 \quad (1)$$

where μ is the misfit value, n is the number of data points, and for each data point i, o_i is the observed value, m_i is the modeled value and σ_i is the observed error. The results of the parameter test are presented for the high-temperature data in Figure 8; a full set of misfit values can be found in the Supplementary Information (Supplementary Table 2). Note, however, that the overall misfit is strongly controlled by the misfit to the AHe data.

The high-temperature data clearly suggest a cooler thermal structure than our initial guess: models with a basal temperature of 570 °C and crustal heat production of 0.8 μW m^{-3} provide the best fits to both the ZFT and the $^{40}Ar/^{39}Ar$ data; there is a strong positive correlation between misfit and both basal temperature and heat production. Interestingly, the ZFT data seem to prefer the later onset of exhumation (45 Ma) although this is not so clearly shown by the $^{40}Ar/^{39}Ar$ data. The low-temperature data show more complex trends but their dependence on the thermal structure is less pronounced than that of the high-temperature data.

4.5. Topographic evolution scenario

In an attempt to improve our predictions for the lower-elevation AFT and AHe samples, we have implemented the topographic evolution scenario suggested by Coney et al. (1996) and Fitzgerald et al. (1999). In this scenario, the Ebro foreland basin and the South Pyrenean Unit were backfilled and buried by late-orogenic continental conglomerates in the Late Eocene - Oligocene. Coney et al. (1996) suggested that, starting in the Late Miocene, the Pyrenees were re-exhumed by erosional excavation to the present relief. Recently, Fillon and van der Beek (2012) quantified the timing and amount of backfilling from thermo-kinematic modeling of the same AFT and AHe dataset as that used here. They propose that the sediments gradually filled the valleys of the pro-wedge up to about 2.6 km elevation between 40 Ma and 29 Ma. This

valley fill remained stable until about 9 Ma, when the valleys were gradually re-excavated in response to regressive erosion. We have used the values provided by Fillon and van der Beek (2012) to model the topographic evolution.

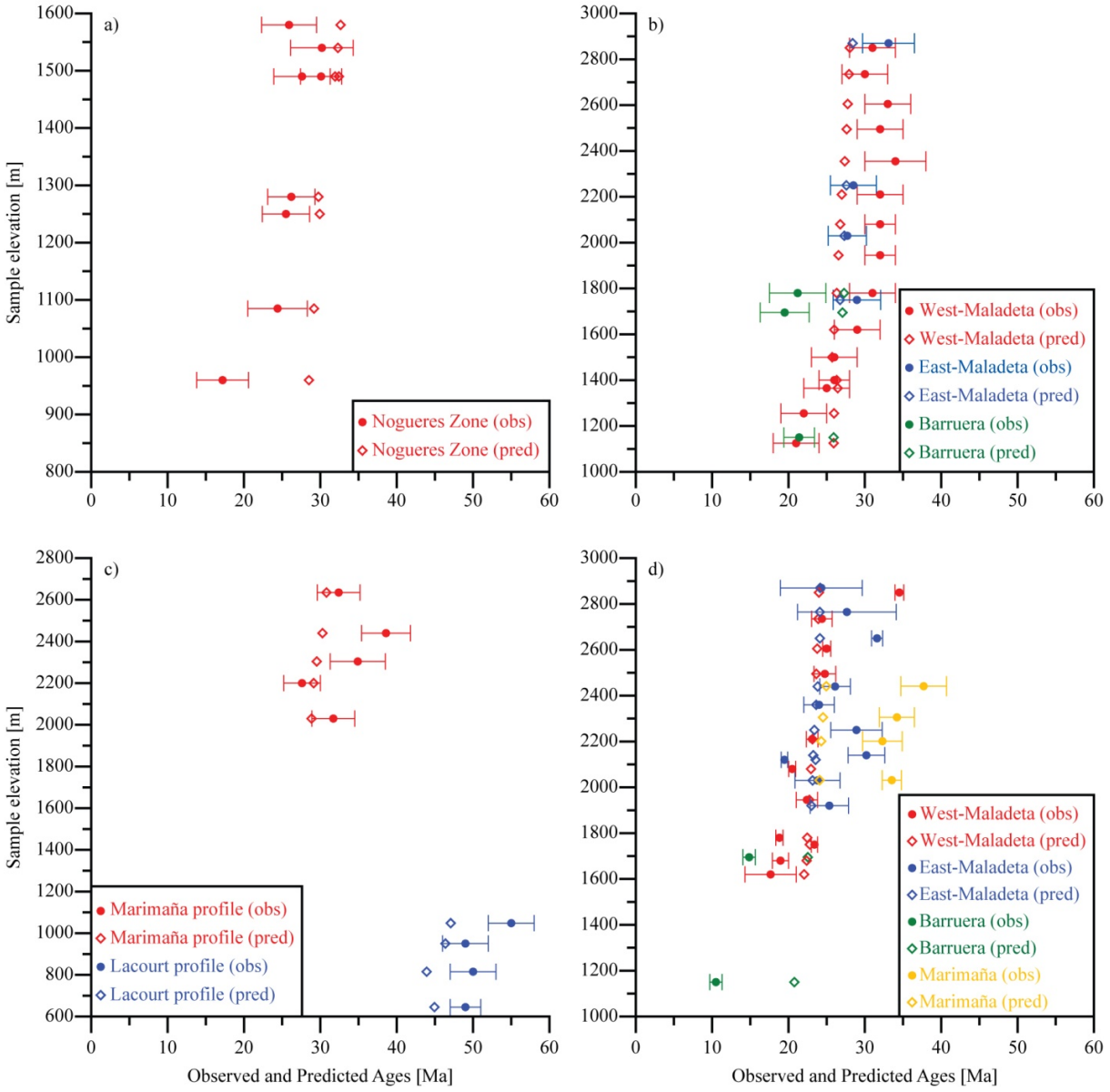

Figure 9. Comparison of predicted (solid symbols) and observed (open symbols with error bars) low-temperature thermochronologic ages for the best fitting model including post-orogenic valley-filling and re-excavation: **(a)** AFT data from the Nogueres Zone; **(b)** AFT data from Maladeta and Barruera; **(c)** AFT data from Marimaña and Lacourt; **(d)** AHe data from Maladeta and Barruera. See Figures 1 and 3 for locations of sampling profiles.

The imposed changes in topography have little effect on the predicted high-temperature thermochronometers; the ZFT samples show only partially reset ages and the *t* – *T* paths corresponding to the K-feldspar $^{40}Ar/^{39}Ar$ samples show very similar characteristics to those predicted by the reference model, in terms of the peak temperature experienced during the model time (Figure 6). However, the imposed topographic scenario significantly improves the fit of the predicted AFT ages in the Nogueres Zone (Figure 9 a, Supplementary Table 2). The improvement is also evident for some of the lower-elevation samples from the Maladeta and Barruera profiles, while the fit of higher-elevation samples from the Maladeta and Marimaña massifs does not change dramatically (Figures 9 b and c). For the samples from the Lacourt profile, north of the drainage divide, keeping the present-day topography constant throughout the modeled time period provides the best fit to the data. This is an expected outcome, as there is no evidence for syn- or post-orogenic burial of the northern flank of the orogen. Imposing an evolving post-orogenic topography also improves the fit of the AHe age predictions for most of the lower-elevation samples in the Maladeta and Barruera profiles, although it increased the misfit for some of the higher-elevation samples (Figure 9 d).

5. Discussion

5.1. Limitations of the approach

Before starting the interpretation of our results, it is essential to discuss the limitations of the proposed method and explore their possible effects on our findings.

Most balanced section restorations are drawn by hand and minor inaccuracies can lead to inconsistencies in the shapes of crustal blocks. The eclectic shifting of the North Pyrenean sub-

vertical faults through time (Figure 2) provides an example of the possible inconsistencies arising from the hand-drawn nature of the restoration. While the structural-kinematic models are internally consistent, they also represent a simplification with respect to the original hand-restored cross section. However, the generation of a set of consistent, quantitative velocity fields is required for using PECUBE and implies the use of a quantitative restoration tool such as 2D-Move.

Movements along faults with highly complex geometries are modeled with simple shear. This simple algorithm models deformation of the hanging-wall by moving each point by the same horizontal distance following a path parallel to the fault (Waltham, 1989; White et al., 1986). The algorithm is generally applicable for a wide range of fault kinematics. However, the method is incapable of handling internal (pure-shear) deformation of the blocks. Processes such as internal thickening and thinning cannot be reproduced with this model. The reconstruction presented by Muñoz (1992) displays significant internal thickening of the Nogueres thrust-sheet (Figure 2), preventing the assessment of the pre-50-Ma reconstruction.

The use of the vectorial sum of the displacements to calculate the velocity field in each of the time intervals means that it is impossible to separate the effect of rapid, short-lived faulting events from the effect of those that were active throughout the entire interval. This implies that if the time intervals of the restoration are long, a relatively short faulting event with high exhumation rates and a longer faulting event with lower exhumation rates will yield similar velocity fields. The length of the time intervals is limited by the temporal resolution of the modeled section restoration. In our case the temporal resolution of the section restoration is

mainly dictated by the sedimentary record in the southern Pyrenean fold-and-thrust belt (Muñoz, 1992; Beaumont et al., 2000).

While the age-prediction models – especially those for the low-temperature thermochronometers – are sensitive to the topographic changes, the paleo-topography is hard to reconstruct with reasonable accuracy. In the presented case study, a very simple topographic evolution model has been implemented. The only currently available data that constrain the paleo-topography of the Pyrenees suggest that they rose to their current elevation during the Eocene, between ~49 and ~41 Ma (Huyghe et al., 2012). We have therefore assumed the initial topography to be the same as the present-day topography. In addition, the evolution of morphology and relief is rather simple, as we only impose a changing minimum elevation of the topography. This means that the model linearly fills up or erodes the topography to the specified minimum elevation (see Fillon and van der Beek, 2012 for a detailed discussion). Published provenance data for the preserved late-orogenic conglomerates suggest that planform drainage patterns have been relatively stable since the Eocene on the southern flank of the Pyrenees (Vincent, 2001) and while there is no such evidence from the northern flank, the limited tectonic activity of the retro-wedge also supports our simplified topographic evolution history.

Finally it is necessary to point out that velocity fields derived with the same method from a different restoration could also provide predictions that would fit the observations. This non-uniqueness means that by using the method it is possible to invalidate a restoration, but it is not possible to tell if a restoration that is consistent with the thermochronological data is

absolutely correct. To use the words of Oreskes et al. (1994), “confirming observations do not demonstrate the veracity of a model hypothesis, they only support its probability”.

5.2. Viability of the section reconstruction

It is essential to show that the section reconstruction is kinematically viable, before proceeding with the thermo-kinematic modeling and the evaluation of its consistency with the available thermochronological data.

In our case study, we had to make a number of minor modifications on the present-day time slice in order to be able to reproduce the general features of the 30 Ma and 36 Ma time slices of the section restoration (Figure 5). A detailed description of these modifications can be found in the Supplementary Information. The internal deformation of the Orri thrust-sheet implied by the section restoration between 36 Ma and 50 Ma made it difficult to reproduce the 50-Ma time slice with high accuracy. The elongation and thinning of the Orri thrust-sheet on the original restoration resulted in more displacement along the basal decollement and significantly more contraction along the section than we infer from our section balancing (Figure 5). Despite the obvious discrepancies between the original restoration and our modeling, we have included the 50-Ma time slice in our thermo-kinematic modeling, as it captures the general features (e.g. the juxtaposition of the Orri and the Rialp blocks and the shallow position of the Orri thrust-sheet) reasonably well. The inclusion of the 50-Ma time slice is important for the thermo-kinematic modeling, as it is required to predict the ages of the available high-temperature (ZFT and K-feldspar $^{40}Ar/^{39}Ar$) thermochronometers.

The 20 % thickening of the Nogueres thrust-sheet resulting from internal deformation between 50 Ma and 60 Ma (Figure 2) prevents the assessment of the section reconstruction beyond the 50-Ma time slice.

5.3. Implications of the thermo-kinematic modeling

Despite its limitations, the proposed method is capable of quantitatively evaluating a section restoration using both low- and high-temperature thermochronology data, providing an independent test on the consistency of both datasets. In case of the Pyrenees, the different deformation events are very well constrained owing to the large amount of geological and geophysical data and the unusually well preserved thrust structures and related syn-orogenic sediments. In other geological settings, the method described here can help to test different hypotheses on the timing of deformation phases, or on structural interpretations, by quantitative comparison of different scenarios with available thermochronology datasets.

In our case study, the kinematic history inferred from the balanced-section restoration is compatible with the available thermochronological datasets. The two predicted reset ZFT ages are not significantly younger then the model time suggesting that they might be only partially reset; a feature that is notoriously difficult to identify, as ZFT data usually do not include a kinetic parameter. Moreover, reset ZFT ages have been reported locally from Axial Zone massifs to the east and west of our study area (e.g., Canigou, Néouvieille, cf. Whitchurch et al., 2012 and references therein). Out of the three $t - T$ paths inferred from K-feldspar $^{40}Ar/^{39}Ar$ thermochronometry by Metcalf et al. (2009), two (PY55 and PY56, from elevations of 1400 m and 1760 m respectively; Figure 6 a and b) are in good agreement with the model predictions. However, while our model predicts similar maximum reheating (~280 °C) for all three samples,

the results of Metcalf et al. (2009) imply significantly lower maximum reheating (~175 °C) for the highest-elevation sample (PY63 from an elevation of 2850 m; Figure 6 c). Such a large difference in the maximum temperature experienced during burial would imply an unrealistically high geothermal gradient of ~100 °C/km, questioning the validity of the *t* – *T* path inferred from sample PY63. As Metcalf et al. (2009) noted, the Ar-release spectrum of this sample was not very well fit by the thermal model. Our models point to an onset of rapid exhumation at around 45 Ma rather than 50 Ma.

The predicted low-temperature thermochronometric ages generally show a reasonable fit with the observations, except for lower-elevation samples from the Axial Zone (Figure 7). We have therefore included the post-orogenic topographic evolution scenario initially proposed by Coney et al. (1996), using the timing and topographic constraints inferred by Fillon and van der Beek (2012). According to this model, the southern flank of the Pyrenees was gradually buried in syn-tectonic sediments by 29 Ma up to an elevation of 2.6 km, before being re-excavated again after 9 Ma. Such burial affects the lower-elevation samples significantly while having very little effect on samples from higher elevations. With this scenario, the thermo-kinematic modeling yielded AFT and AHe ages fitting both the higher- and the lower-elevation samples of the Axial Zone reasonably well (Figure 9). It is also consistent with thermal-history models for low-elevation samples derived from track-length data (Metcalf et al., 2009).

6. Conclusions

We have presented a method that allows quantitative comparison of orogen kinematics inferred from balanced section restorations with independent thermochronological datasets.

We have applied our method to the balanced section restoration presented by Muñoz (1992) and Beaumont et al. (2000) for the Central Pyrenees as a case study. Our structural-kinematic modeling could reproduce the section restoration with high accuracy up to the 36-Ma time slice and with limited accuracy up to the 50-Ma time slice. The thermochronometric ages predicted by the modeling are generally in reasonably good agreement with both the high- and low-temperature thermochronology data available in the Central Pyrenees; hence we conclude that the restoration is to a first order consistent with these datasets. The high-temperature data suggest a somewhat later onset of underthrusting and rapid exhumation, as well as a somewhat cooler crustal thermal structure, than what we initially imposed. The fit of the low-temperature data improved by taking into account late-stage burial and re-excavation of the southern flank of the Pyrenean wedge using the topographic evolution scenario presented by Fillon and van der Beek (2012). The method can be applied on section restorations from other orogens as well, with the aim of evaluating the consistency of the restoration with an independent dataset. We propose that the method can also be used to improve constraints on the timing of deformation phases along a restored balanced cross-section.

Acknowledgements

This study is supported by the Norwegian Research Council that funded the Norwegian component of the European Science Foundation Eurocores TOPO-Europe project PyrTec. We thank Jean Braun, Charlotte Fillon and Josep Anton Muñoz for helpful discussions and comments on various stages of the work, and Paul Fitzgerald and Hugh Sinclair for providing details on sample locations. The Bergen Center of Computational Science is acknowledged for access to computational infrastructure. Detailed and insightful comments by James Metcalf and

Peter DeCelles on the manuscript, as well as by an anonymous reviewer on an earlier version, helped to improve it significantly.

References

Beaumont, C., J.A. Muñoz, J. Hamilton, and P. Fullsack (2000), Factors controlling the Alpine evolution of the Central Pyrenees inferred from a comparison of observations and geodynamical models, J. Geophys. Res., 105, 8121-8145.

Braun, J. (2002), Quantifying the effect of recent relief changes on age-elevation relationships, Earth Planet. Sci. Lett., 200, 331-343.

Braun, J. (2003), Pecube: a new finite-element code to solve the 3D heat transport equation including the effects of a time-varying finite amplitude surface topography, Comp. Geosci., 29, 787–794.

Braun, J., P. van der Beek, and G.E. Batt (2006), Quantitative Thermochronology. Numerical methods for the interpretation of Thermochronological data, Cambridge University Press, Cambridge, 258 pp.

Braun, J., P. van der Beek, P. Valla, X. Robert, F. Herman, C. Glotzbach, V. Pedersen, C. Perry, T. Simon-Labric, and C. Prigent (2012), Quantifying rates of landscape evolution and tectonic processes by thermochronology and numerical modeling of crustal heat transport using PECUBE, Tectonophysics, 524-525, 1-28.

Capote, R., J.A. Muñoz, J.L. Simon, C.L. Liesa, and L.E. Arlegui (2002), Alpine tectonics I: The alpine system north of the Betic Cordillera. in: Gibbon, W., Moreno T. (eds.), The Geology of Spain. The Geological Society, London, pp. 367–400.

Coney, P.J., J.A. Muñoz, K.R. McClay, and C.A. Evenchick (1996), Syntectonic burial and post-tectonic exhumation of the southern Pyrenees foreland fold-thrust belt, J. Geol. Soc. London, 153, 9-16.

Cook, F. A., J. L. Varsek, R. M. Clowes, E. R. Kanasewich, C. S. Spencer, R. R. Parrish, R. L. Brown, S. D. Carr, B. J. Johnson, and R. A. Price (1992), Lithoprobe crustal reflection cross section of the southern Canadian Cordillera, 1, Foreland thrust and fold belt to Fraser River Fault, Tectonics, 11, 12–35.

Dahlstrom, C.D.A. (1969), Balanced cross sections, Can. J. Earth Sci. 6, 743-757.

DeCelles, P.G., D.M. Robinson, J. Quade, T.P. Ojha, C.N. Garzione, P. Copeland, and B.N. Upreti (2001), Stratigraphy, structure, and tectonic evolution of the Himalayan fold-thrust belt in western Nepal, Tectonics, 20, 487-509.

ECORS Pyrenees Team (1988), The ECORS deep reflection seismic survey across the Pyrenees, Nature, 331, 508–511.

Egan S.S., S. Kane, T.S. Buddin, G.D. Williams, and D. Hodgetts (1999), Computer modelling and visualisation of the structural deformation caused by movement along geological faults, Comp. Geosci., 25, 283-297

Farley, K.A. (2000), Helium diffusion from apatite: general behavior as illustrated by Durango fluorapatite, J. Geophys. Res., 105, 2903-2914.

Fernandez, M., and E. Banda (1989), An approach to the thermal field in northeastern Spain, Tectonophysics, 164, 259-266.

Fernandez, M., I. Marzan, A. Correia, and E. Ramalho (1998), Heat flow, heat production, and lithospheric thermal regime in the Iberian Peninsula, Tectonophysics, 291, 29-53.

Fillon, C., and P. van der Beek (2012), Post-orogenic evolution of the southern Pyrenees: constraints from inverse thermo-kinematic modelling of low-temperature thermochronology data, Basin Res., 24, 418-436.

Fillon, C., R.S. Huismans, P. van der Beek, and J.A. Muñoz (2013), Syntectonic sedimentation controls on the evolution of the southern Pyrenean fold-and-thrust belt: Inferences from coupled tectonic-surface processes models, J. Geophys. Res., 118, 5665-5680, doi: 10.1002/jgrb.50368.

Fitzgerald, P.G., J.A. Muñoz, P.J. Coney, and S.L. Baldwin (1999), Asymmetric exhumation across the Pyrenean orogen: implications for the tectonic evolution of a collisional orogen, Earth Planet. Sci. Lett., 173, 157-170.

Flowers, R.M., R.A. Ketcham, D.L. Shuster, and K.A. Farley (2009), Apatite (U-Th)/He thermochronometry using a radiation damage accumulation and annealing model. Geochim. Cosmochim. Acta, 73, 2347-2365.

Galbraith, R., G. Laslett (1997), Statistical modeling of thermal annealing of fission tracks in zircon. Chem. Geol., 140, 123-135.

Gautheron, C., L. Tasson-Got, J. Barbarand, and M. Pagel (2009), Effect of alpha-damage annealing on apatite (U-Th)/He thermochronology. Chem. Geol., 266, 157-170.

Gibson, M., H.D. Sinclair, G.J. Lynn, and F.M. Stuart (2007), Late- to post-orogenic exhumation of the Central Pyrenees revealed through combined thermochronological data and modelling. Basin Res., 19, 323-334.

Green, P., I. Duddy, G. Laslett, K. Hegarty, A. Gleadow, and J.F. Lovering (1989), Thermal annealing of fission tracks in apatite 4. Quantitative modelling techniques and extension to geological timescales. Chem. Geol., 79, 155-182.

Glotzbach, C., P. van der Beek, and C. Spiegel (2011), Episodic exhumation of the Mont Blanc massif, Western Alps: constraints from numerical modelling of thermochronology data. Earth Planet. Sci. Lett., 304, 417-430.

Herman, F., P. Copeland, J.P. Avouac, L. Bollinger, G. Mahéo, P. Le Fort, S. Rai, D. Foster, A. Pecher, K. Stüwe, and P. Henry (2010), Exhumation, crustal deformation, and thermal structure of the Nepal Himalaya derived from the inversion of thermochronological and thermobarometric data and modeling of the topography. J. Geophys. Res., 115, B06407, doi: 10.1029/2008JB006126.

Huyghe, D., F. Mouthereau, and L. Emmanuel (2012), Oxygen isotopes of marine mollusc shells record Eocene elevation change in the Pyrenees, Earth Planet. Sci. Lett., 345-348, 131-141.

Ketcham, R.A., A. Carter, R.A. Donelick, J. Barbarand, and A.J. Hurford (2007), Improved modeling of fission-track annealing in apatite, Am. Mineral., 92, 789–798.

Lock, J., and S. Willett (2008), Low-temperature thermochronometric ages in fold-and-thrust belts, Tectonophysics, 456, 147-162.

Long, S., N. McQuarrie, T. Tobgay, and D. Grujic (2011), Geometry and crustal shortening of the Himalayan fold-thrust belt, eastern and central Bhutan, Geol. Soc. Am. Bull., 123, 1427-1447.

Long, S.P., N. McQuarrie, T. Tobgay, I. Coutand, F.J. Cooper, P.W. Reiners, J.-A. Wartho, and K.V. Hodges (2012), Variable shortening rates in the eastern Himalayan thrust belt, Bhutan: Insights from multiple thermochronologic and geochronologic data sets tied to kinematic reconstructions, Tectonics, 31, TC5004, doi: 10.1029/2012tc003155.

McQuarrie, N. (2002), The kinematic history of the central Andean fold-thrust belt, Bolivia: implications for building a high plateau, Geol. Soc. Am. Bull., 14, 950-963.

McQuarrie, N., J.B. Barnes, and T.A. Ehlers (2008), Geometric, kinematic, and erosional history of the central Andean Plateau, Bolivia (15-17°S), Tectonics, 27, TC3007, doi: 10.1029/ 2006TC002054.

Metcalf, J.R., P.G. Fitzgerald, S.L. Baldwin, and J.A. Muñoz (2009), Thermochronology of a convergent orogen: Constraints on the timing of thrust faulting and subsequent exhumation of the Maladeta Pluton in the Central Pyrenean Axial Zone, Earth Planet. Sci. Lett., 287, 488–503.

Muñoz, J.A., A. Martínez, and J. Vergés (1986), Thrust sequences in the Spanish Pyrenees, J. Struct. Geol., 8, 399–405.

Muñoz, J.A. (1992), Evolution of a continental collision belt: ECORS Pyrenees crustal balanced cross section. in: McClay, K.R. (ed.). Thrust Tectonics, Chapman & Hall, London, 235–246.

Oreskes, N., K. Shrader-Frechette, and K. Belitz (1994), Verification, validation, and confirmation of numerical models in the earth sciences, Science, 263, 641-646.

Puigdefabregas, C., J.A. Muñoz, and M. Marzo (1986), Thrust belt development in the eastern Pyrenees and related depositional sequences in the southern foreland basin, in: Allen, Ph., Homewood, P. (eds.), Foreland basins, Int. Assoc. Sedimentol. Spec. Publ., 8, 229-246.

Puigdefabregas, C., J.A. Muñoz, and J. Vergés (1992), Thrusting and foreland basin evolution in the southern Pyrenees, In: McClay, K.R. (ed.), Thrust Tectonics, Chapman & Hall, London, 247-254.

Rahn, M. K., M. T. Brandon, G. E. Batt, and J. I. Garver (2004), A zero-damage model for fission track annealing in zircon, Am. Mineral., 89, 473–484.

Reiners, P. W., and M. T. Brandon (2006), Using thermochronology to understand orogenic erosion, Ann. Rev. Earth Planet. Sci., 34, 419-466.

Robert, X., P. van der Beek, J. Braun, C. Perry, and J.L. Mugnier (2011), Control of detachment geometry on lateral variations in exhumation rate in the Himalaya: Insights from low-temperature thermochronology and numerical modeling, J. Geophys. Res., 116, B05202, doi: 10.1029/2010JB007893.

Robinson, D.M., P.G. DeCelles, and P. Copeland (2006), Tectonic evolution of the Himalayan thrust belt in western Nepal: Implications for channel flow models, Geol. Soc. Am. Bull., 118, 865–885.

Roest, W.R., and S.P. Srivastava (1991), Kinematics of the plate boundaries between Eurasia, Iberia and Africa in the North Atlantic from the late Cretaceous to the present, Geology, 19, 613–616.

Rosenbaum, G., G.S. Lister, and C. Duboz (2002), Relative motions of Africa, Iberia and Europe during Alpine orogeny, Tectonophysics, 359, 117-129.

Roure, F., F. Bergerat, B. Damotte, J.-L. Mugnier, and R. Polino (1996), The ECORS-CROP alpine seismic traverse, Mémoire de la Société Géologique de France, 170, 113 pp.

Rushlow, C.R., J.B. Barnes, T.A. Ehlers, and J. Vergés (2013), Exhumation of the southern Pyrenean fold-thrust belt (Spain) from orogenic growth to decay, Tectonics, 32, 843-860, doi: 10.1002/tect.20030.

Schmid, S.M., O.A. Pfiffner, N. Froitzheim, G. Schönborn, and E. Kissling (1996), Geophysical-geological transect and tectonic evolution of the Swiss-Italian Alps, Tectonics, 15, 1063-1064.

Séguret, M., and M. Daignières (1986), Crustal scale balanced cross sections from the Pyrenees; discussion, Tectonophysics, 129, 303-318.

Sinclair, H.D., M. Gibson, M. Naylor, and R.G. Morris (2005), Asymmetric growth of the Pyrenees revealed through measurement and modeling of orogenic fluxes, Am. J. Sci., 305, 369-406.

Stephenson, J., K. Gallagher, and C.C. Holmes (2006), A Bayesian approach to calibrating apatite fission track annealing models for laboratory and geological timescales, Geochim. Cosmochim. Acta, 70, 5183-5200

ter Voorde, M., C.H. de Bruijne, S.A.P.L. Cloetingh, and P.A.M. Andriessen (2004), Thermal consequences of thrust faulting: simultaneous versus successive fault activation and exhumation, Earth Planet. Sci. Lett., 223, 395-413.

Valla, P.G., F. Herman, P. van der Beek, and J. Braun (2010), Inversion of thermochronological age-elevation profiles to extract independent estimates of denudation and relief history -- I: Theory and conceptual model, Earth Planet. Sci. Lett., 295, 511-522.

Vergés, J., and J.A. Muñoz (1990), Thrust sequences in the southern Central Pyrenees, Bull. Soc. Géol. Fr., 8, 265-271

Vincent, S.J. (2001), The Sis palaeovalley: a record of proximal fluvial sedimentation and drainage basin development in response to Pyrenean mountain building, Sedimentology, 48, 1235-1276.

Vissers, R.L.M. and P.T. Meijer (2012), Iberian plate kinematics and Alpine collision in the Pyrenees, Earth Sci. Rev., 114, 61-83.

Waltham, D. (1989), Finite difference modelling of hangingwall deformation, J. Struct. Geol., 11, 433-437.

Waltham, D., and S. Hardy (1995), The velocity description of deformation. Paper 1: theory, Mar. Petrol. Geol., 12, 153-163

Whipp, D.M., T.A. Ehlers, A. Blythe, K.W. Huntington, K.Hodges, and D.W. Burbank (2007), Plio-Quaternary exhumation history of the central Nepalese Himalaya: 2. Thermokinematic and thermochronometer age prediction model, Tectonics, 26, TC3003, doi: 10.1029/ 2006TC001991.

Whitchurch, A.L., A. Carter, H.D. Sinclair, R.A. Duller, A.C. Whittaker, and P.A. Allen (2011), Sediment routing system evolution within a diachronously uplifting orogen: Insights from detrital zircon thermochronological analyses from the South-Central Pyrenees, Am. J. Sci., 311, 442-482, doi: 10.2475/05.2011.03

White, N.J., J.A. Jackson, and D.P. McKenzie (1986), The relationship between the geometry of normal faults and that of sedimentary layers in their hanging-walls, J. Struct. Geol., 8, 897-910.

Withjack, M.O., and E.T. Peterson (1993), Prediction of normal-fault geometries – a sensitivity analysis, Am. Assoc. Petrol. Geol. Bull., 77, 1860-1873.

Wolf, R.A., K.A. Farley, and D.M. Kass (1998), Modeling of the temperature sensitivity of the apatite (U-Th)/He thermochronometer, Chem. Geol., 148, 105-114.

Supplementary Information for paper 1

Supplementary Information

Detailed modifications to the initial structural-kinematic model

Apart from the extension of the decollement below the northern side of the section, detailed in the methods section, a number of minor modifications and simplifications have been applied to the initial model setup in order to achieve the best match between the model and the section restoration.

Only the major faults have been restored, as the expected effect of the minor faults on the thermal structure is negligible. We did not restore the small internal structures of the South Pyrenean Unit as there is no thermochronometric data available from these units; instead we used the basal decollement to transfer the displacements of the Axial Zone to the surface. The northern tip-zone of the Orri and Rialp blocks has also been slightly modified to reduce complexity. Finally the amount of subducting upper-crustal material had to be slightly increased and redistributed in order to be able to reproduce the basal decollement of the pre-dating time slices.

Restored faulting events

The restoration indicates tectonic quiescence between 20 Ma and the present day so the marker field is undeformed and the derived velocity field consists of null vectors only. Between 30 Ma and 20 Ma, 43.5 km displacement is applied along the base of the Rialp block, running out to the South Pyrenean Unit. 30 km of the displacement is accommodated at the tip of the Serres Marginales unit (representing a more distributed deformation taking place in the various

small sub-units of the South Pyrenean Unit) while the rest of the displacement is accommodated in the Bóixols unit, along the Morreres back-thrust. In the northern part of the section the up-thrusted lower-crustal wedge is active. 4 km downwards directed displacement is applied on its base and the same amount of upwards directed displacement is applied on its roof. Between 36 Ma and 30 Ma the deformation along the base of the Rialp is continued with 18 km displacement applied, running out to the South Pyrenean Unit. Similarly, in the North Pyrenean Unit, the slow deformation of the up-thrusted lower crustal wedge is continued with 2 km downwards-directed displacement applied on its base and the same amount of upwards-directed displacement applied on its roof. Finally, between 50 Ma and 36 Ma the main activity takes place along the base of the Orri block (on top of the Rialp block), with 14 km displacement applied, running out to the South Pyrenean Unit. In the mean time, the slow deformation of the up-thrusted lower crustal wedge is still present with 1.8 km downwards directed displacement applied on its base of it and the same amount of upwards-directed displacement applied on its roof.

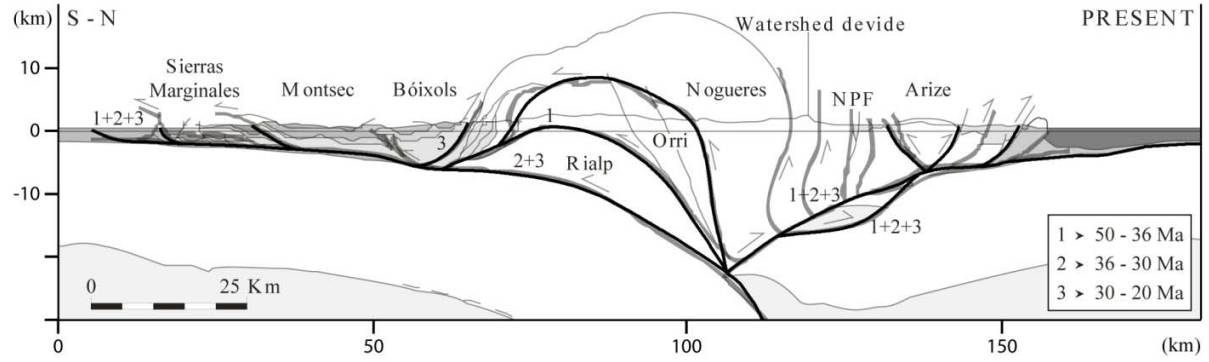

Supplementary Figure 1. Main active faults in the ECORS cross-section and their respective periods of activity throughout the structural-kinematic modeling

Sample ID	Elevation	AHe age	Reference	AFT age	Reference	ZFT age	Reference
Nogueres samples							
Col-00/1540	1540 m	n.a.		30,2 ± 4,1	Gibson	n.a.	
Col-00/1490	1490 m	n.a.		27,6 ± 3,7	Gibson	n.a.	
Esc-02/1250	1250 m	n.a.		15,5 ± 3,1	Gibson	n.a.	
Sas-02/1580	1580 m	n.a.		25,9 ± 3,6	Gibson	n.a.	
Sas-02/1490	1490 m	n.a.		30,1 ± 2,7	Gibson	n.a.	
Mon-02/1280	1280 m	n.a.		26,2 ± 3,1	Sinclair	n.a.	
Mon-02/1085	1085 m	n.a.		24,4 ± 3,9	Sinclair	n.a.	
Mon-02/960	960 m	n.a.		17,2 ± 3,4	Sinclair	n.a.	
Mon-02/805	805 m	n.a.		n.a.		159 ± 33	Sinclair
Maladeta profiles							
PY63	2850 m	34,52 ± 0,57	Metcalf	31,0 ± 3,0	Fitzgerald	n.a.	
PY64	2735 m	24,38 ± 1,35	Metcalf	30,0 ± 3,0	Fitzgerald	n.a.	
PY65	2605 m	25,00 ± 0,53	Metcalf	33,0 ± 3,0	Fitzgerald	n.a.	
PY66	2495 m	24,76 ± 1,42	Metcalf	32,0 ± 3,0	Fitzgerald	n.a.	
PY67	2355 m	n.a.		34,0 ± 4,0	Fitzgerald	n.a.	
PY68	2210 m	23,10 ± 0,76	Metcalf	32,0 ± 3,0	Fitzgerald	n.a.	
PY53	2120 m	19,47 ± 0,43	Metcalf	n.a.		n.a.	
PY69	2080 m	20,49 ± 0,46	Metcalf	32,0 ± 2,0	Fitzgerald	n.a.	
PY70	1945 m	22,41 ± 1,40	Metcalf	32,0 ± 2,0	Fitzgerald	n.a.	
PY56	1780 m	18,81 ± 0,48	Metcalf	31,0 ± 3,0	Fitzgerald	n.a.	
PY57	1680 m	18,95 ± 1,06	Metcalf	n.a.		n.a.	
PY58	1620 m	17,66 ± 3,35	Metcalf	29,0 ± 3,0	Fitzgerald	n.a.	
PY59	1500 m	n.a.		26,0 ± 3,0	Fitzgerald	n.a.	
PY55	1400 m	n.a.		26,0 ± 2,0	Fitzgerald	n.a.	
PY61	1365 m	n.a.		25,0 ± 3,0	Fitzgerald	n.a.	
PY62	1255 m	n.a.		22,0 ± 3,0	Fitzgerald	n.a.	
PY60	1125 m	n.a.		21,0 ± 3,0	Fitzgerald	n.a.	
Mal-00/2870	2870 m	24,30 ± 5,37	Gibson	33,1 ± 3,4	Sinclair	n.a.	
Mal-00/2765	2765 m	27,65 ± 6,47	Gibson	n.a.		n.a.	
Mal-00/2650	2654 m	31,60 ± 0,73	Gibson	n.a.		n.a.	
Mal-00/2440	2440 m	26,10 ± 2,00	Gibson	n.a.		n.a.	
Mal-00/2360	2360 m	24,00 ± 2,00	Gibson	n.a.		n.a.	
Mal-00/2250	2250 m	28,90 ± 3,37	Gibson	28,5 ± 3,0	Sinclair	n.a.	
Mal-00/2140	2140 m	30,20 ± 2,40	Gibson	n.a.		n.a.	
Mal-00/2030	2030 m	23,80 ± 2,95	Gibson	27,7 ± 2,5	Sinclair	n.a.	
Mal-00/1920	1920 m	25,35 ± 2,51	Gibson	n.a.		n.a.	
Mal-00/1750	1750 m	23,40 ± 0,41	Gibson	28,96 ± 3,1	Sinclair	49,3 ± 3,1	Sinclair
Barruera profile							
Bar-02/1780	1780 m	n.a.		21,2 ± 3,7	Sinclair	n.a.	
Bar-02/1695	1695 m	14,85 ± 1,03	Gibson	19,5 ± 3,2	Sinclair	n.a.	
Bar-02/1150	1150 m	10,50 ± 0,85	Gibson	21,4 ± 2,0	Sinclair	104 ± 7	Sinclair

Sample ID	Elevation	AHe age	Reference	AFT age	Reference	ZFT age	Reference
Marimaña profile							
MM-02/2635	2634 m	n.a.		32,4 ± 2,8	Sinclair	49,7 ± 3,1	Sinclair
MM-02/2440	2440 m	37,70 ± 3,00	Gibson	38,6 ± 3,2	Sinclair	n.a.	
Mar-00/2304	2304 m	34,20 ± 2,30	Gibson	34,9 ± 3,6	Sinclair	n.a.	
Mar-00/2200	2200 m	32,30 ± 2,60	Gibson	27,6 ± 2,4	Sinclair	n.a.	
Mar-00/2030	2030 m	33,53 ± 1,26	Gibson	31,7 ± 2,8	Sinclair	n.a.	
Lacourt profile							
PY2	1048 m	n.a.		55,0 ± 3,0	Fitzgerald	n.a.	
PY3	950 m	n.a.		49,0 ± 3,0	Fitzgerald	n.a.	
PY7	815 m	n.a.		50,0 ± 3,0	Fitzgerald	n.a.	
PY6	645 m	n.a.		49,0 ± 2,0	Fitzgerald	n.a.	
PY5	470 m	n.a.		37,0 ± 1,0	Fitzgerald	n.a.	

Supplementary Table 1. The complete list of thermochronologic data used in the thermo-kinematic modeling (data from Fitzgerald et al. (1999), Sinclair et al. (2005), Gibson et al. (2007) and Metcalf et al. (2009)).

model	AHe_wmal	AHe_emal	AHe_barr	AFT_wmal	AFT_emal	AFT_barr	AFT_nog	AFT_mar	AFT_lac	ZFT	ArAr	AHe_misfit	AFT_misfit	Sum_misfit
hetp08_bt570	487.037	215.365	380.591	30.916	1.339	28.183	43.184	7.486	2.249	1.539	2.169	1082.993	113.357	1200.057
hetp08_bt600	482.529	212.493	371.399	31.862	1.463	26.460	39.183	8.405	4.216	2.089	13.951	1066.420	111.588	1194.048
hetp08_bt630	479.075	210.017	362.335	33.229	1.660	24.590	35.649	9.496	7.059	2.894	46.696	1051.426	111.684	1212.701
hetp095_bt570	470.229	205.783	338.785	36.052	1.955	20.514	33.644	10.308	5.488	2.472	17.725	1014.797	107.961	1142.954
hetp095_bt600	469.267	204.166	330.437	38.068	2.260	18.886	30.615	11.555	8.701	3.410	52.979	1003.870	110.085	1170.343
hetp095_bt630	476.086	207.819	350.565	35.184	1.971	22.320	31.579	10.815	11.180	4.161	97.438	1034.469	113.050	1249.118
uf_hetp08_bt570	448.404	209.035	220.492	34.569	2.541	13.381	20.985	11.118	10.518	1.814	2.907	877.931	93.112	975.764
uf_hetp08_bt600	450.806	207.924	206.662	37.212	3.101	11.800	17.505	12.648	15.509	2.471	18.092	865.392	97.775	983.731
uf_hetp08_bt630	454.494	207.205	192.227	40.136	3.663	10.319	14.498	14.238	21.962	3.435	54.730	853.926	104.817	1016.907
uf_hetp095_bt570	452.529	208.015	198.862	38.423	3.347	11.020	15.972	13.169	16.892	2.601	17.978	859.405	98.823	978.808
uf_hetp095_bt600	456.609	207.451	185.124	41.384	3.987	9.700	13.329	14.675	23.452	3.586	53.439	849.185	106.527	1012.736
uf_hetp095_bt630	461.514	207.233	171.721	44.321	4.577	8.538	11.214	16.146	30.985	5.021	109.179	840.468	115.781	1070.450
45_hp08_bt570	489.494	211.619	387.884	35.552	1.300	29.239	55.837	7.506	1.284	0.629	3.089	1088.997	130.718	1223.432
45_hp08_bt600	485.167	208.555	378.527	36.822	1.369	27.366	49.190	8.299	2.354	0.834	5.855	1072.249	125.401	1204.339
45_hp08_bt630	481.894	205.895	369.296	38.331	1.516	25.462	44.630	9.259	3.850	1.128	28.040	1057.085	123.048	1209.301
45_hp095_bt570	483.313	207.793	373.649	37.338	1.410	26.390	46.830	8.572	2.586	0.891	6.433	1064.754	123.126	1195.205
45_hp095_bt600	480.898	205.529	365.724	38.788	1.570	24.828	43.100	9.459	3.994	1.174	27.027	1052.151	121.739	1202.092
45_hp095_bt630	479.177	203.442	357.213	40.591	1.779	23.110	39.382	10.456	5.901	1.610	69.739	1039.832	121.219	1232.400
45_uf_hp08_bt570	454.532	195.113	283.231	36.976	1.662	18.413	32.916	9.543	6.871	0.671	3.054	932.875	106.381	1042.982
45_uf_hp08_bt600	455.132	193.445	271.618	39.369	1.953	16.562	27.332	10.913	9.798	0.889	5.987	920.195	105.927	1032.998
45_uf_hp08_bt630	456.863	192.145	259.766	42.052	2.333	14.846	22.980	12.366	13.489	1.202	28.364	908.774	108.067	1046.407
45_uf_hp095_bt570	455.835	193.255	264.913	40.509	2.163	15.649	24.941	11.379	10.567	0.952	6.569	914.004	105.208	1026.733
45_uf_hp095_bt600	457.810	192.194	254.641	42.997	2.501	14.195	21.385	12.671	14.027	1.253	27.334	904.645	107.777	1041.009
45_uf_hp095_bt630	460.934	191.395	243.142	45.932	2.961	12.667	17.958	14.106	18.507	1.715	70.254	895.471	112.132	1079.573

Supplementary Table 2. Misfit of predicted and observed thermochronological ages, calculated using Eq. (1) for different subsets of the data as well as the entire dataset, for the different models run. Key: uf: models including valley filling; hetp: heat production; bt: basal temperature; 45: models assuming a 45 My onset time.

Paper II

First order control of syntectonic sedimentation on crustal-scale structure of mountain belts

Zoltán Erdős[1,2], Ritske S. Huismans[1] and Peter van der Beek[2]

[1]Department of Earth Sciences, University of Bergen, Bergen, N-5007, Norway

[2]Institut des Sciences de la Terre (ISTerre), Université Joseph Fourier, Grenoble, 38041, France

Corresponding author: Zoltán Erdős, University of Bergen, N-5007 Bergen, Norway (zoltan.erdos@geo.uib.no)

Abstract

The first-order characteristics of orogenic mountain belts and the potential feedback with surface processes are predicted by critical taper theory. While the feedback between erosion and mountain-belt structure has been fairly intensively studied, little attention has been given to the potential role of synorogenic deposition. For thin-skinned fold-and-thrust belts, recent studies indicate a strong control of syntectonic deposition on structure, as sedimentation tends to stabilize the thin-skinned wedge. However, the factors controlling basement deformation below such belts, as evident for example in the Zagros or in the Swiss Alps, remain largely unknown. Previous work has suggested that such variations in orogenic structure may be explained by the thermo-tectonic "age" of the deforming lithosphere and hence its rheology. Here we demonstrate that sediment loading of the foreland basin area provides an alternative control and may explain the variable basement involvement in orogenic belts. We identify two end-members: 1) sediment-starved orogenic systems with thick-skinned basement deformation in an axial orogenic core and thin-skinned deformation in the bordering forelands; and 2) sediment-loaded orogens with thick packages of synorogenic deposits, derived from the axial basement zone, deposited on the surrounding foreland fold-and-thrust belts and characterized by basement deformation below the foreland. Using thermo-mechanical models of unprecedented resolution, we demonstrate a strong feedback between deposition and crustal scale thick-skinned deformation. Our results show that the loading effects of syntectonic deposition lead to long crustal scale thrust sheets beneath the orogenic foreland and explain the contrasting characteristics of sediment-starved and sediment-loaded orogens, showing for the first time how both thin- and thick-skinned crustal deformation are linked to sediment

deposition in these orogenic systems. We show that the observed model behavior is consistent with observations from a number of natural orogenic systems.

1. Introduction

Foreland fold-and-thrust belts develop in the depressions bordering mountain belts that result from lithospheric loading and involve a varying amount of sediments and basement rocks. Understanding the evolution of foreland fold-and-thrust belts is of key importance for resource exploration, storage of CO_2, as well as seismic risk assessment (Alavi, 2007; Avouac, 2003; Brooks et al., 2011; Guellec et al., 1990). These tectonic structures display a wide range of characteristics, many of which remain poorly understood.

The potential role of surface processes on mountain building has been debated for nearly three decades (e.g. Whipple, 2009), since the initial recognition of their potential importance through the development of critical-wedge theory (Dahlen, 1990; Davis et al., 1983). A large number of numerical and analogue modelling experiments have explored the strong localizing feedback of erosion on the orogenic hinterland (Koons, 1990; Stolar et al., 2006; Willett, 1999) and the effect of sedimentation on the shallow structures of foreland fold-and-thrust belts (Bonnet et al., 2007; Fillon et al., 2012; Ford, 2004). The governing controls of basement deformation below foreland fold-and-thrust belts as observed, for instance, in the European Alps (Madritsch et al., 2010; Roure, 2008) or the Zagros (Alavi, 2007; Berberian, 1995) remain, however, poorly understood and little attention has been given to the potential role of synorogenic deposition in controlling such deformation. This problem has not been specifically addressed before because it requires combining locally high resolution (< 1 km) and large spatial (lithospheric)

scales, which has until recently been beyond the capability of both numerical and analogue models.

In this study we use high resolution, two-dimensional thermo-mechanical numerical model experiments to study the effects of sedimentation and erosion on an orogenic system in which thick-skinned deformation (i.e. involving the basement) of the orogenic hinterland and foreland fold-and-thrust belt development co evolve. We offer a novel interpretation that accounts for observations from two contrasting styles of orogenic belts and their forelands that we term “sediment-starved” and “sediment-loaded” orogens. We show, using numerical models with unprecedented resolution allowing addressing both the lithospheric and fold-and-thrust belt scale that the structural style of these end members depends on the amount of syntectonic sedimentation in the orogenic foreland basins, which has a controlling effect on the style of basement deformation in mountain belts. We show in addition that the observed behaviour is fully consistent with and expected from simple scaling analysis arguments. We compare our results to a number of orogens from around the globe to show that our results are in good correlation with observed behavior of various natural systems.

2. Methods

2.1. Numerical Model Description

We use a modified version of the Arbitrary Lagrangean-Eulerian finite element code FANTOM (Thieulot, 2011), which solves the Stokes equation coupled to the heat-transport equation. We model thermo-mechanically coupled, plane-strain, incompressible viscous-plastic creeping flows to investigate the behavior of a layered lithosphere with frictional-plastic and thermally

activated power-law viscous rheologies in a contractional regime. When stress is below yield, deformation occurs by viscous flow and follows temperature-dependent nonlinear power-law rheologies. The effective viscosity η_{eff} is specified as:

$$\eta_{eff} = f.A^{-1/n}.\dot{\varepsilon}^{(1-n)/2n}.exp\left(\frac{Q+Vp}{nRT}\right) \quad (1)$$

Where *A* is the pre-exponential scaling factor, *n* is the power-law exponent, $\dot{\varepsilon}$ is the second invariant of the deviatoric strain rate tensor, *Q* is the activation energy, *V* is the activation volume, *p* is the pressure, *T* is the temperature and *R* is the universal gas constant. Values for the parameters *A*, *n*, *Q* and *V* are based on laboratory measurements carried out on 'wet' and 'dry' olivine and 'wet' quartzite, respectively (Gleason and Tullis, 1995; Karato and Wu, 1993); these values are given in Table 1 for each model material. The effective viscosity of quartz-dominated rocks is characterized by large uncertainties due to compositional differences (Huismans and Beaumont, 2003). The applied viscosity scaling, using the scaling factor *f* represents a simple technique that can be used to create strong frictional lower-crust bonded to the strong upper mantle lithosphere without recourse to additional flow laws, each with its own uncertainties.

Frictional-plastic yielding is modeled with a pressure-dependent Drucker-Prager yield criterion, equivalent to the Coulomb yield criterion in two dimensions. Yielding occurs when

$$(J_2')^{1/2} = p\ sin\phi_{eff} + C\ cos\phi_{eff} \quad (2)$$

Where J_2' is the second invariant of the deviatoric stress, ϕeff is the effective internal angle of friction, given as psin(ϕeff) = (p-pf)sin(ϕ) for pore-fluid pressure pf, and C is cohesion. With appropriate choice of C and ϕeff this yield criterion approximates the effect of pore fluid

pressure and frictional sliding in rocks. We note that ϕeff ≈15° corresponds to the effective ϕ when the pore-fluid pressure is approximately hydrostatic. Mechanisms, such as fluid pressure variations (Sibson, 1990), and mineral transformations (Bos and Spiers, 2002) may reduce the brittle and frictional strength. To account for such processes the effect of plastic strain softening is introduced by a linear decrease of the internal angle of friction from 15° to 2° and a simultaneous decrease of cohesion from 20 MPa to 4 MPa for strains between 0.5 and 1.5 (Huismans and Beaumont, 2003).

In addition to solving the Stokes equations for viscous-plastic flows, the heat-transport equation is also solved. The mechanical and thermal systems are coupled through the temperature dependent rheologies and densities; they are solved sequentially for each model time step. The initial temperature field is laterally uniform and increases parabolically with depth from the surface (T_0 = 0 °C) to the base of the crust (T_m = 550 °C), and then linearly to the base of mantle lithosphere (T_b =1330 °C). The temperature of the sublithospheric mantle is initially uniform at T =1330 °C. The temperature distribution is influenced by crustal heat production (h_c=0.8 10^{-6} W m^{-3}). The lateral boundaries are insulated, while the basal boundary is set to a constant temperature T_b= 1330 °C.

The densities of salt, crust, mantle lithosphere and sub-lithospheric mantle at reference temperature T_0 = 0 °C, are given in Table 1. The temperature dependent density is given by $\rho(T) = \rho_0(1 - \alpha(T - T_0))$, with the thermal expansion coefficient α = 3.1x10^{-6} °C^{-1} for the sediments and the crust, and α = 0 °C^{-1} for mantle materials.

2.2. Model setup

The models are set up as an idealized representation of the lithosphere and the sublithospheric mantle in a 600-km high and 1200-km wide box (Figure 1). The lithosphere consists of a 25 km thick upper crust and a 10 km thick lower crust overlying an 85 km thick lithospheric mantle, with the sublithospheric mantle below. The upper 3 km of the crust are formed by a pre-orogenic sedimentary package, separated from the crust below by a 1 km thick weak layer, representing a décollement horizon and having the mechanical properties of evaporates (Table 1). This setup allows for modelling the (thin-skinned) behavior of pre-orogenic sedimentary sequences as well as the (thick-skinned) deformation of the underlying continental basement, providing a unique opportunity to investigate the coexisting thin-skinned and thick-skinned tectonic regimes.

The Eulerian grid consists of 2400 nodes in the horizontal and 300 nodes in the vertical dimension, respectively. The distribution of the nodes is irregular in the vertical direction with 125 nodes in the upper crust, 125 nodes in the lower crust and mantle lithosphere, and 50 nodes in the sublithospheric mantle. Consequently, the resolution in the horizontal direction is equal to 500 m for the entire model domain, while the resolution in the vertical direction is 200 m in the upper crust, 800 m in the lower crust and mantle lithosphere, and 9.5 km in the sublithospheric mantle.

A free surface at the top of the numerical model allows for tracking directly the evolution of topography. Velocity boundary conditions are imposed on both sides of the models (v = 0.5 cm/yr on each side), while at the base of the model a free-slip condition is imposed.

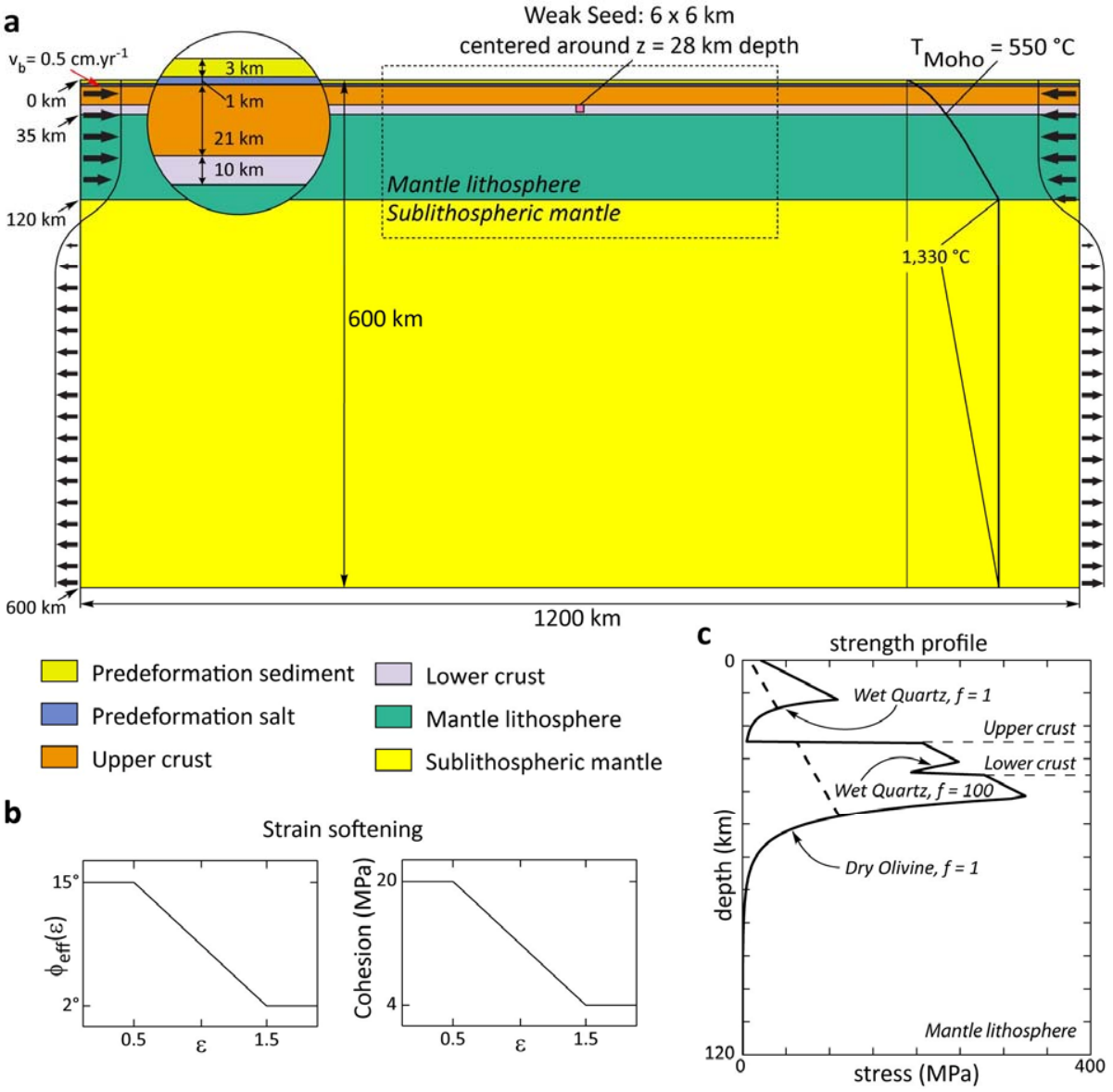

Figure 1. Numerical model design. a) Model material setup with the position of weak seed, velocity boundary conditions, and initial temperature conditions. **b)** Strain softening of frictional-plastic rheology **c)** Initial strength profile of the models.

2.3. Surface processes

The reference model (Model 1 Figure 2a-d) does not include sedimentation and erosion. The top of the model is acting as a free surface with minimal surface smoothing applied to prevent numerical instabilities.

Units	Salt	Upper Crust + Precollision Sediment	Lower Crust	Mantle Lithosphere	Sublithospheric Mantle
			Mechanical Parameters		
Thickness (km)	1	21 + 3	10	85	480
Reference density (kg m^{-3})	2300	2800		3360	3300
Friction angle (deg)	-		15° - 2°		
Cohesion (Pa)	-		2.10^7 - 2.10^6		
Flow law		Wet Quartz		Dry Olivine	Wet Olivine
Reference		Gleason and Tullis (1995)		Karato and Wu (1993)	
scaling factor	-	1	100	1	1
A (Pa^{-n} s^{-1})	-	$8.574\ 10^{-28}$	$8.574\ 10^{-28}$	$2.4168\ 10^{-15}$	$1.393\ 10^{-14}$
Q (J mol^{-1})	-	$222.815\ 10^3$	$222.815\ 10^3$	$540.41\ 10^3$	$429.83\ 10^3$
n	-	4	4	3.5	3
V (m^3 mol^{-1})	-	$3.1\ 10^{-6}$	$3.1\ 10^{-6}$	$25\ 10^{-6}$	$15\ 10^{-6}$
R (J mol^{-1} $°C^{-1}$)			8.3144		
			Thermal Parameters		
Thermal diffusivity (m^2 s^{-1})			$1\ 10^{-6}$		
Thermal exansion (K^{-1})		$3.1\ 10^{-5}$		0	
Heat productivity (μW m^{-3})		$0.8\ 10^{-6}$		0	

Table 1. Mechanical and thermal parameters used in the models.

In Models 2, 3 and 4 (Figure 2e-h and Figure 3a-h), a simple sedimentation algorithm is applied. Starting after 100 km of crustal shortening, all topography below a reference base level is filled with sediments at the end of every time step. The sediments and the upper crust have identical material properties. The delayed initiation of sedimentation gives time for the development of an orogen with a more than 2 km high mean topography that could provide a source for the sediments. This representation of sedimentation is very simple but the resulting geometry of the basin fill is consistent with natural foreland basin systems (DeCelles and Giles, 1996).

Models 5, 6, and 7 (figure 4a-c) moreover employ a simple elevation-dependent erosion rule: $\Delta h/\Delta t = h.E_r$, where h is the elevation, Δt is the time and E_r is an erosional rate constant (t^{-1}). E_r is set so that a 2 km high topography erodes by 1 km in 10 Myr.

3. Results

3.1. Reference model: Model 1

Our model of mountain building in the absence of syntectonic sedimentation occurs in three main phases (Figure 2a-d; see also Supplementary Movie 1): 1) Contraction results in the uplift of a symmetrical keystone structure with foreland depressions developing on either side. Shortening is accommodated within the strong lower crust and mantle lithosphere by subduction into the sub-lithospheric mantle. 2) With continued crustal deformation, thin-skinned thrust sheets form in the footwall of the keystone structure, rooting in a shallow detachment in the pre-orogenic salt layer, while deformation in the crust propagates towards the foreland with the formation of new basement thrust sheets building a crustal-scale pro-wedge (Figure 2a; note that we use the terms “pro” and “retro” wedge following Ellis et al. (1998)). 3) Subsequently, contraction is accommodated by episodic formation of new basement thrust sheets propagating to the foreland, and by development of thin-skinned thrusts in the pre-orogenic sediments rooting in the footwall of the active basement thrust sheet (Figure 2b). The overriding plate remains relatively undeformed throughout the model evolution, showing no significant basement deformation and only limited thin-skinned deformation of the retro-wedge (Figure 2c).

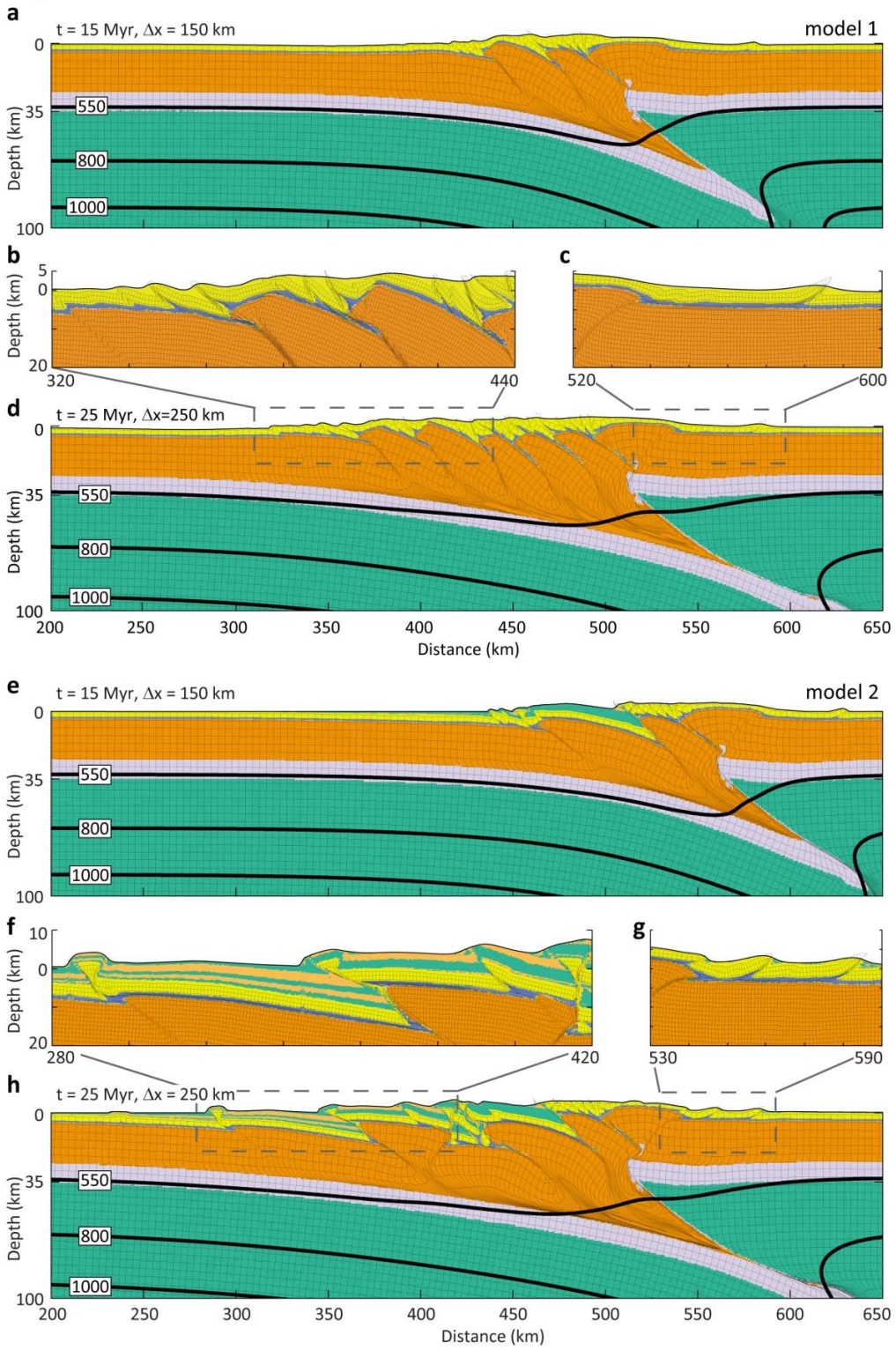
a
t = 15 Myr, Δx = 150 km
model 1
Depth (km)
0
35
100
550
800
1000
b
c
5
0
20
320
440
520
600
d
t = 25 Myr, Δx=250 km
200
250
300
350
400
450
500
550
600
650
Distance (km)
e
t = 15 Myr, Δx = 150 km
model 2
f
g
10
280
420
530
590
h
t = 25 Myr, Δx = 250 km

Figure 2. The effect of syntectonic sedimentation on the development of mountain belts. a-d) Reference model A with no surface processes, showing deformed Lagrangean mesh and sample isotherms after **(a)** 15 Myr (Δx = 150 km) contraction and **(d)** 25 Myr (Δx = 250 km) contraction respectively; **(b)** and **(c)** show extracts from Figure 2d showing the small-scale deformation patterns in the foreland fold-and-thrust belts. **e-h)** Model 2 including a simple sedimentation algorithm with base level set to 0 m, showing deformed Lagrangean mesh and sample isotherms after **(e)** 15 Myr (Δx = 150 km) contraction and **(h)** 25 Myr (Δx = 250 km) contraction respectively; **(f)** and **(g)** show extracts from Figure 2h showing the small-scale deformation patterns in the foreland fold-and-thrust belts.

3.2. The effect of syntectonic sedimentation: Model 2

Model 2 has the same model setup as the reference model with the additional inclusion of syntectonic sedimentation up to a base level of 0 m. The evolution of the model experiment can also be described in three phases (Figure 2e-h). Phases 1 and 2 are identical to that of Model 1, with uplift of a symmetrical keystone structure, initiation of continental subduction and formation of an initial basement thrust sheet, as syntectonic deposition is effective only after formation of initial topography. Phase 3 includes syntectonic deposition and shows markedly different behavior (Figure 2e-h; see also Supplementary Movie 2). Initially a wide and deep sediment filled foreland basin forms in the footwall of the active basement thrust sheet. As a result, the deformation zone remains active for a longer time, accommodating more displacement while the subsequent new basement thrust forms much more externally below the foreland, creating a longer thrust sheet (Figure 2e). This elongated deformation cycle is then repeated. Sedimentation also affects thin-skinned deformation, creating a complex set of long thrust sheets and pop-up structures, with significant displacement along the base of individual units (Figure 2f). The overriding plate exhibits slightly more deformation than in Model 1, with limited basement deformation and out-of-sequence thin-skinned thrust development (Figure 2g).

3.3. Varying the amount of deposition: Models 3 and 4

Models 3 and 4 (Figure 3a-h) represent two intermediate scenarios capturing the model behavior of orogenic systems positioned between the end-member models, Model 1 and 2. The amount of sedimentation is controlled through limiting the space available for deposits to fill. This is achieved by setting the base level of sedimentation in Models 3 and 4 to -500 m and -250 m, respectively.

When base level is set low (-500 m), only minor syntectonic deposition occurs (Model 3; Figure 3a-d). The resulting large-scale deformation pattern is very similar to that of the reference model, with basement thrust sheets exhibiting only minor lengthening (especially in the external parts of the orogen). In contrast, the thin-skinned thrust sheets are significantly longer compared to the reference model (Figure 3b). When increasing the amount of space available for syntectonic deposition to fill (Model 4; Figure 3e-f), the effect of syntectonic sedimentation, elongating both the thin-skinned and the basement thrust sheets, is evident (Figure 3e-h and Supplementary Video 3), resulting in a structure similar to that of Model 2.

Figure 3. Intermediate model scenarios presenting the nonlinear effect of syntectonic sedimentation on the development of mountain belt. a-d) Model 3 including a simple sedimentation algorithm with base level set to -500 m, showing deformed Lagrangean mesh and sample isotherms after **(a)** 15 Myr (Δx = 150 km) contraction and **(d)** 25 Myr (Δx = 250 km) contraction respectively; **(b)** and **(c)** show extracts from Figure 2d showing the small-scale deformation patterns in the foreland fold-and-thrust belts. **e-h)** Model 4 including a simple sedimentation algorithm with base level set to -250 m, showing deformed Lagrangean mesh and sample isotherms after **(e)** 15 Myr (Δx = 150 km) contraction and **(h)** 25 Myr (Δx = 250 km) contraction respectively; **(f)** and **(g)** show extracts from Figure 2h showing the small-scale deformation patterns in the foreland fold-and-thrust belts.

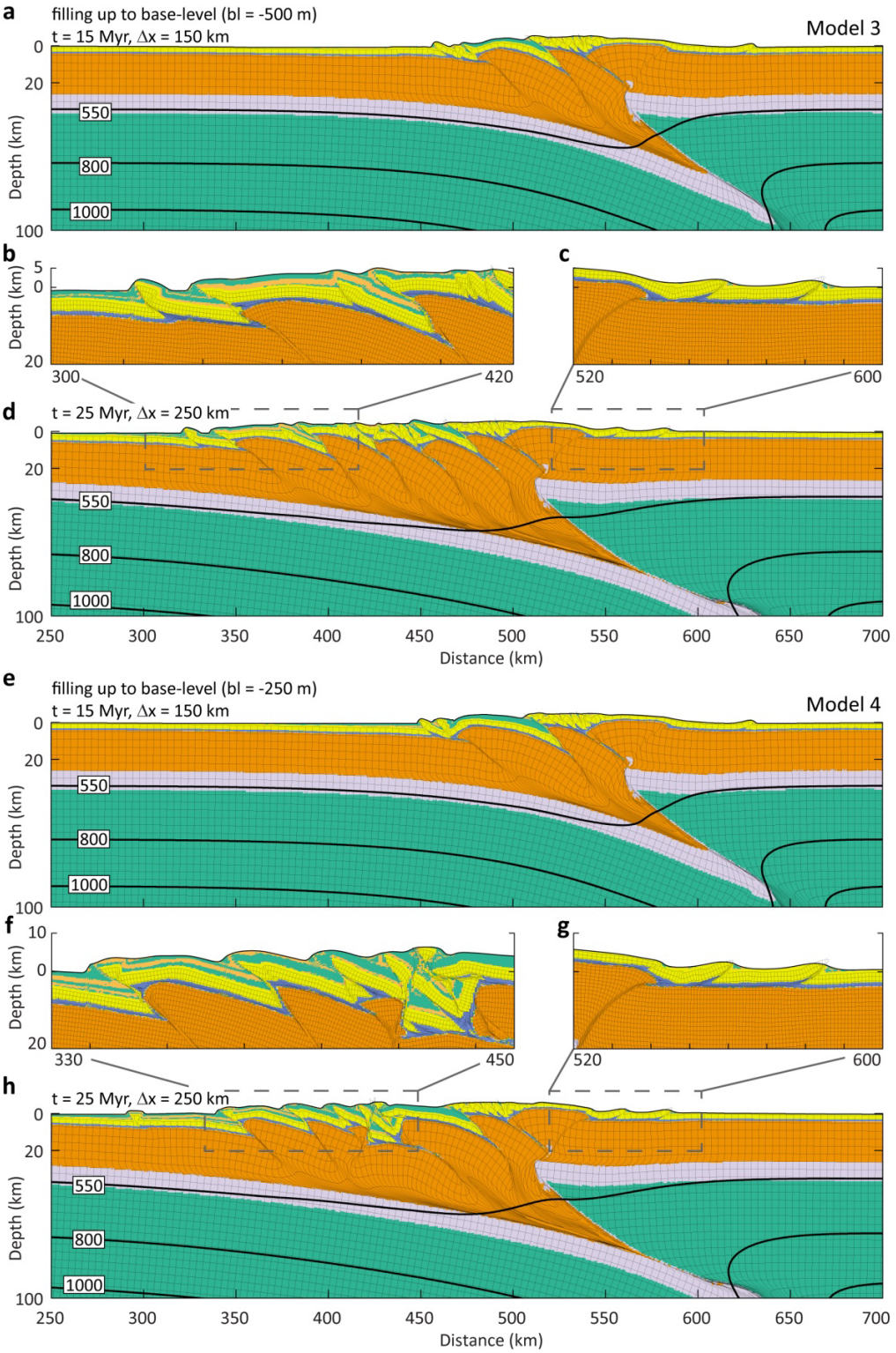
a
filling up to base-level (bl = -500 m)
t = 15 Myr, Δx = 150 km
Model 3
Depth (km)
0
20
100
550
800
1000
b
c
5
0
20
300
420
520
600
d
t = 25 Myr, Δx = 250 km
250
300
350
400
450
500
550
600
650
700
Distance (km)
e
filling up to base-level (bl = -250 m)
t = 15 Myr, Δx = 150 km
Model 4
f
g
10
330
450
h
t = 25 Myr, Δx = 250 km

3.4. Sensitivity to erosion: Models 5 to 7

The next set of models explores the sensitivity to erosion, by applying a simple elevation-dependent erosion algorithm (see Section 2.3). In Model 5 (Figure 4a), sedimentation is not allowed for (corresponding model without erosion is Model 1), while in Models 6 and 7 (Figure 4b-c) the same simple sedimentation algorithm is enabled as in our previous models with the base level set to -250 m and 0 m respectively.

Model 5 shows very similar behavior to that of our reference model, with the uplift of an initial keystone structure followed by the subduction of the lower crust attached to the mantle lithosphere, repeated formation of upper crustal basement thrust sheets in a frontal/basal accretion cycle, and the development of thin-skinned thrust sequences in the pre-orogenic sediments rooting in the footwall of the active basement thrust. As a result of erosion, the thin-skinned structures developing in the pre-orogenic sediments are gradually removed from the internal part of the orogen, exposing the keystone structure and the abandoned basement thrust sheets (Figure 4a).

When allowing for a moderate amount of sedimentation along with erosion (Model 6; Figure 4b), the general style of deformation is not altered significantly. The cyclic formation of basement thrust sheets and the coupled development of thin-skinned thrust sheets in the footwall of the active basement thrust dominates the orogen but the thin-skinned thrust sheets are significantly longer than in the reference model. This behavior is very similar to that of Model 4.

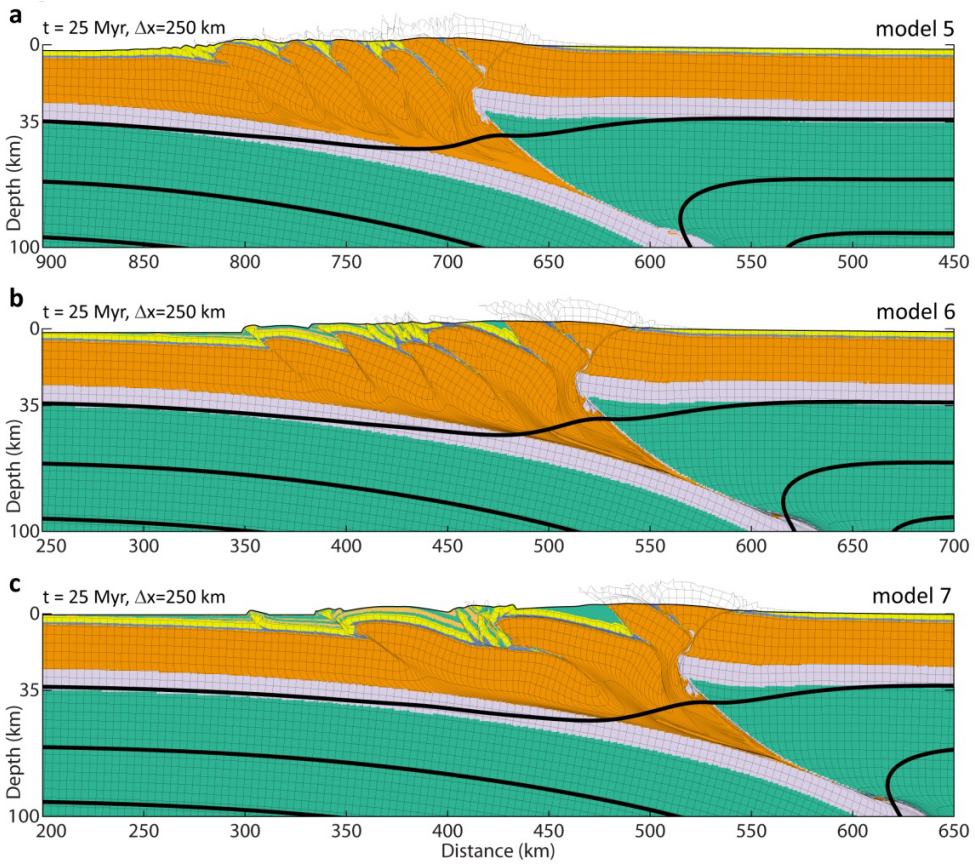

Figure 4. Models 5 to 7 presenting the model sensitivity to erosion. a) Model 5 allowing for an elevation dependent erosion process but not allowing for sedimentation, showing deformed Lagrangean mesh and sample isotherms after 25 Myr (dx = 250 km) contraction. **b)** Model 6 allowing for moderate amount of sedimentation with base level set to -500 m, and an elevation dependent erosion process, showing deformed Lagrangean mesh and sample isotherms after 25 Myr (dx = 250 km) contraction. **c)** Model 7 allowing for full sedimentation with base level set to 0 m, and an elevation dependent erosion process, showing deformed Lagrangean mesh and sample isotherms after 25 Myr (dx = 250 km) contraction.

However, the sedimentary basins formed early on in the history, together with the pre-orogenic sediments, are removed from the internal parts of the orogen. Erosion also prevents the development of a notable foreland depression in the footwall of the keystone structure in the retro-wedge.

When allowing for strong sedimentation along with erosion (Model 7; Figure 4c) the observed deformation style is very similar to that of Model 2. Both the developing thin-skinned and thick-skinned thrust sheets are elongated compared to the reference model. Basement is only exposed in the most internal part of the orogen with the applied erosion algorithm unable to remove thick layers of syn-orogenic sediments deposited on top of the more external basement thrust-sheets.

4. Discussion

Our numerical modeling results lead us to consider a framework in which two types of orogenic foreland fold-and-thrust belts, which we term sediment-starved and sediment-loaded orogens, are end-members with regard to their basement structure and its development below the foreland.

Sediment-starved orogens (Figure 5a), such as the Urals (Brown et al., 1997a; Brown et al., 1997b), show the following characteristics: (1) short, narrowly spaced basement thrust sheets with relatively small displacement along the individual basement thrusts in the orogenic core, flanked by; (2) short thin-skinned thrust sheets in the foreland if pre-orogenic sediments and a décollement layer are present; (3) no or limited basement deformation below the foreland and; (4) a relatively narrow orogen resulting from basement deformation restricted to the central orogenic core.

In contrast, sediment-loaded orogens (Figure 5b), such as the Swiss Alps (Roure, 2008), have the following markedly different characteristics: (A) long basement thrust sheets with a large amount of displacement along the individual thrusts below thick foreland-basin deposits; (B)

long thin-skinned thrust sheets in the sedimentary fold-and-thrust belt with large displacement along the individual thrust faults; (C) major basement deformation below the foreland; (D) a significantly wider orogenic wedge, as a result of thick-skinned basement deformation in the foreland.

4.1. Syntectonic sedimentation control

We propose that the contrasting characteristics of sediment-starved and sediment-loaded orogen-foreland systems are a direct consequence of syntectonic deposition during the formation of the mountain belt. The numerical models demonstrate that syntectonic sedimentation provides a first-order control not only on thin-skinned deformation, as suggested previously by several authors (Bonnet et al., 2007; Dahlen, 1990; Fillon et al., 2012; Storti and McClay, 1995), but also on thick-skinned basement deformation in orogenic mountain belts and their associated foreland fold-and-thrust belts. Mouthereau et al. (2013) have recently suggested that such variations in orogenic structure can be explained by the thermo-tectonic “age” of the deforming lithosphere and hence its rheology; young, hot and weak lithosphere favoring thick-skinned deformation while orogens in which a significant part of the shortening is taken up by thin-skinned fold-and-thrust belts above a basal décollement would occur primarily on old, cold and strong lithosphere. Our results suggest an alternative control that follows directly from minimum-work principles as presented by Hardy et al. (1998) and Masek and Duncan (1998). This theory predicts that a new thrust should occur at the locus where the total work required for slip on the viscous mid-crustal décollement and breakthrough to the surface is minimized. The main effect of syntectonic sedimentation is to

increase the frictional work required to create a new thick-skinned crustal scale thrust. Consequently, the formation of a new thrust is favored where sediments taper out.

The effect of varying the reference level for sedimentation is not linear, as is evident from the intermediate model scenarios (Model 3 and 4). To better understand the relationship between the length of the basement thrust sheets and the syntectonic sediment thickness, we present a simple analytical scaling argument.

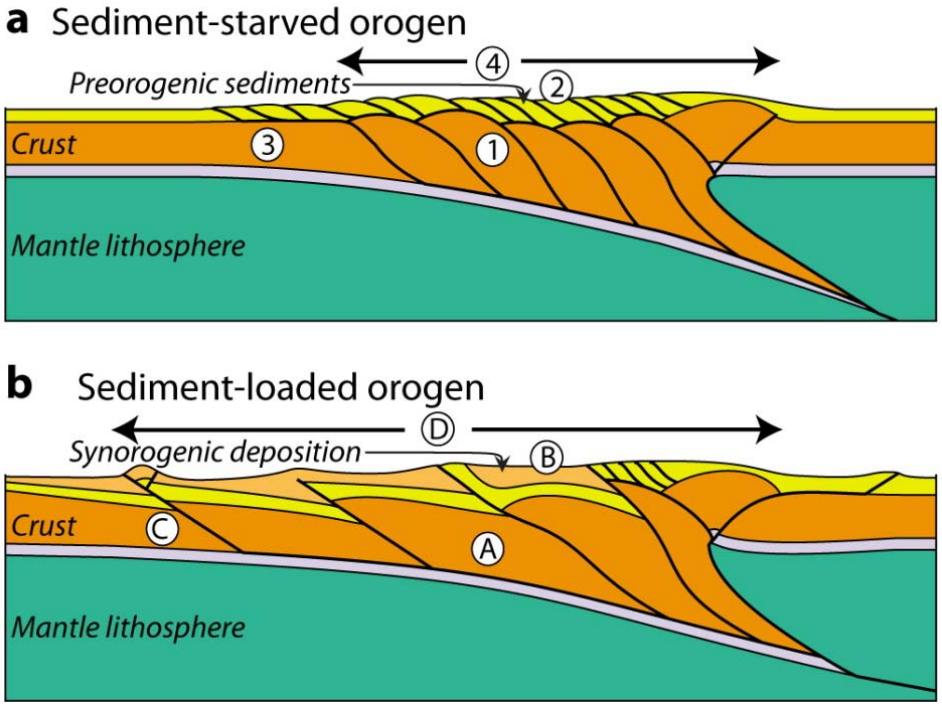

Figure 5. Characteristic properties of sediment-starved and sediment-loaded orogens. a) Sediment-starved orogen: (1) short, narrowly spaced basement thrust sheets, (2) short thin-skinned thrust sheets in the foreland, (3) no or limited basement deformation below the foreland and, (4) basement deformation restricted to the central orogenic core. **b)** Sediment-loaded orogen: (A) long basement thrust sheet below thick foreland-basin deposits, (B) long thin-skinned thrust sheet in the sedimentary fold-and-thrust belt, (C) major basement deformation below the foreland, (D) wide orogenic wedge.

4.2. Scaling analysis

Let us consider a simplified characteristic system (Figure 6), with sediment thickness *S*, thickness of the brittle crust z_B, increased brittle layer thickness at the locus of sedimentation $z_B + S$, coefficient of friction μ, crustal and sediment density ρ, the increase in length of the viscous mid crustal decoupling shear zone ΔL, viscosity of the mid crust η, and average strain-rate on the mid crustal shear zone $\dot{\varepsilon}$.

Note that our analysis assumes that sediments are at surface temperature and therefore directly control the depth to the brittle-ductile transition, a reasonable assumption for rapid synorogenic sedimentation. The three main elements in a simple minimum-work argument are: 1) the integrated strength of the brittle crust without syntectonic deposition, F_B; 2) the integrated strength of the brittle crust with syntectonic deposition, $F_B + \Delta F_B$; 3) the integrated strength of the mid-crustal viscous shear zone, ΔF_D. It can be easily shown that in order for a new brittle crustal scale fault to form in the foreland the following force balance should hold:

$$\mathrm{F_B} + \Delta \mathrm{F_D} = \mathrm{F_B} + \Delta \mathrm{F_B} \qquad (3)$$

that is, ΔF_D and ΔF_B should balance. Using $\Delta F_D = \Delta L 2\eta\dot{\varepsilon}$ and $\Delta F_B = \frac{1}{2}\mu\rho g(S^2 + 2Sz_B)$ indicates that the increase in basement thrust spacing is expected to depend quadratically on differential syntectonic sediment thickness and on the depth and strength of the mid crustal shear zone as:

$$\Delta \mathrm{L} \approx \frac{\frac{1}{2}\mu\rho g\left(\mathrm{S}^2 + 2\mathrm{S}z_{\mathrm{B}}\right)}{2\eta\dot{\varepsilon}} \qquad (4)$$

Using the following values, differential sediment thickness S = 5 km, depth of brittle-ductile transition in the range z_B = 10-20 km, friction coefficient at hydrostatic fluid pressure μ = 0.3,

density ρ = 2800 kg m^{-3}, gravity g = 10 ms^{-2}, viscosity $\eta = 2 * 10^{21}$ Pas, and strain rate $\dot{\varepsilon} = 1 * 10^{-14}\, s^{-1}$, the analysis suggests that 5 km of syntectonic sediments would lead to the increase of thrust length with ~20 km, to first order consistent with our models and with observed thrust-sheet lengths (Figure 8). It is important to point out that strain weakening of the frictional-plastic shear zones is accounted for in our models and provides an additional feedback, promoting continued deformation, and hence resulting in a longer active lifecycle of the thrust sheets. We also note, that the above scaling relationship is particularly sensitive to effective viscosity and strain rate values; parameters described with high uncertainties in nature.

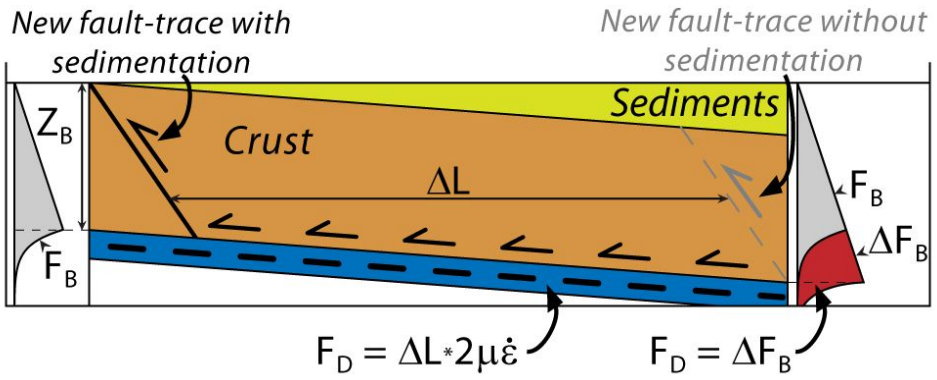

Figure 6. Theoretical section showing the physical rela-tionships resulting from the minimum-work analysis. Blue area represents basal décollement, black line represents the position of a new fault forming in the presence of syntectonic sediments; gray dashed line representing the position of a new fault that would form in the absence of syntectonic sediments.

4.3. System sensitivity to erosion

It is widely accepted, that erosion promotes the formation of narrower orogenic wedges (e.g., Davis et al., 1983; Konstantinovskaia and Malavieille, 2005; Stolar et al., 2006). Models 5 - 7 (Figure 4a-c), which include elevation-dependent erosion, demonstrate this feedback. Model 5 does not include deposition (corresponding model without erosion is Model 1). Both

sedimentation and erosion are included in Models 6 and 7 with -250 m and 0 m base levels respectively and correspond to the Models 4 and 2 without erosion. These models demonstrate that although, as expected, erosion promotes a narrower orogen, the lengthening effect of sedimentation on both the thin-skinned and the basement thrust sheets is largely unaffected by the implemented elevation dependent erosion algorithm, as the latter mainly affects the core of the developing mountain belt and has little effect on the external parts of the orogen.

5. Comparison with natural systems

Model predictions are consistent with observed characteristic basement thrust-sheet lengths and syntectonic sediment thicknesses for a range of mountain belts (Figures 7 and 8). Cross-sections of three different orogens (Urals, Zagros and Swiss Alps) illustrate the correlation between the amount of syntectonic sedimentation and the characteristic length of the underlying thick-skinned basement thrust sheets (Figure 7). Very little syntectonic sedimentation occurred during the development of the Urals foreland fold-and-thrust belt and the characteristic basement thrust-sheet length is of the order of 10 km (Brown et al., 1997a; Brown et al., 1997b)(Figure 7). The Zagros belt represents an intermediate example with syntectonic sediment thickness reaching up to 4 km, while the average basement thrust sheet length is of the order of 20 km (Berberian, 1995)(Figure 7).

A good example of orogenic fold-and-thrust belts characterized by high syntectonic sedimentation is provided by the Swiss Alpine foreland (Bonnet et al., 2007; Mosar, 1999), where up to 8 km of syntectonic sediments must have been present during active deformation, accounting for strong syn- to post-orogenic erosion (Cederbom et al., 2011). The basement

structure below the Alpine foreland varies laterally but seismic activity within the upper crust supports active deformation at depth (e.g., Mosar, 1999; Madritsch et al., 2010), with basement thrust-sheet length reaching up to ~50 km below the Swiss Molasse basin (Roure, 2008)(Figure 7).

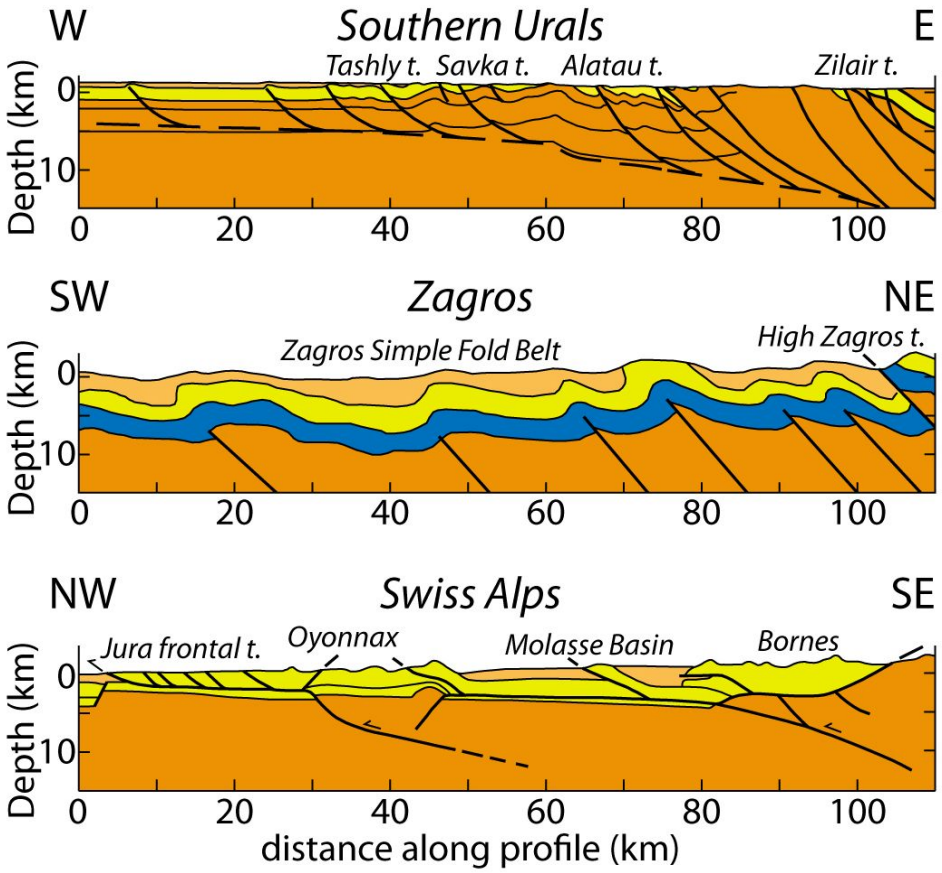

Figure 7. Comparison of results to natural examples. Examples of balanced cross-sections through mountain belts with a varying amount of syntectonic sedimentation. From top to bottom: Southern Urals (Brown et al., 1997a; Brown et al., 1997b); Zagros (Berberian, 1995); Swiss Alps (Roure, 2008).

A global compilation of average thrust-sheet length versus syntectonic sediment thickness of a number of orogens confirms the predicted relationship (Figure 8, Table 2). Although the tectonic settings of these belts show significant variation, a clear positive correlation between the average thrust-sheet length and syntectonic sediment thickness is evident.

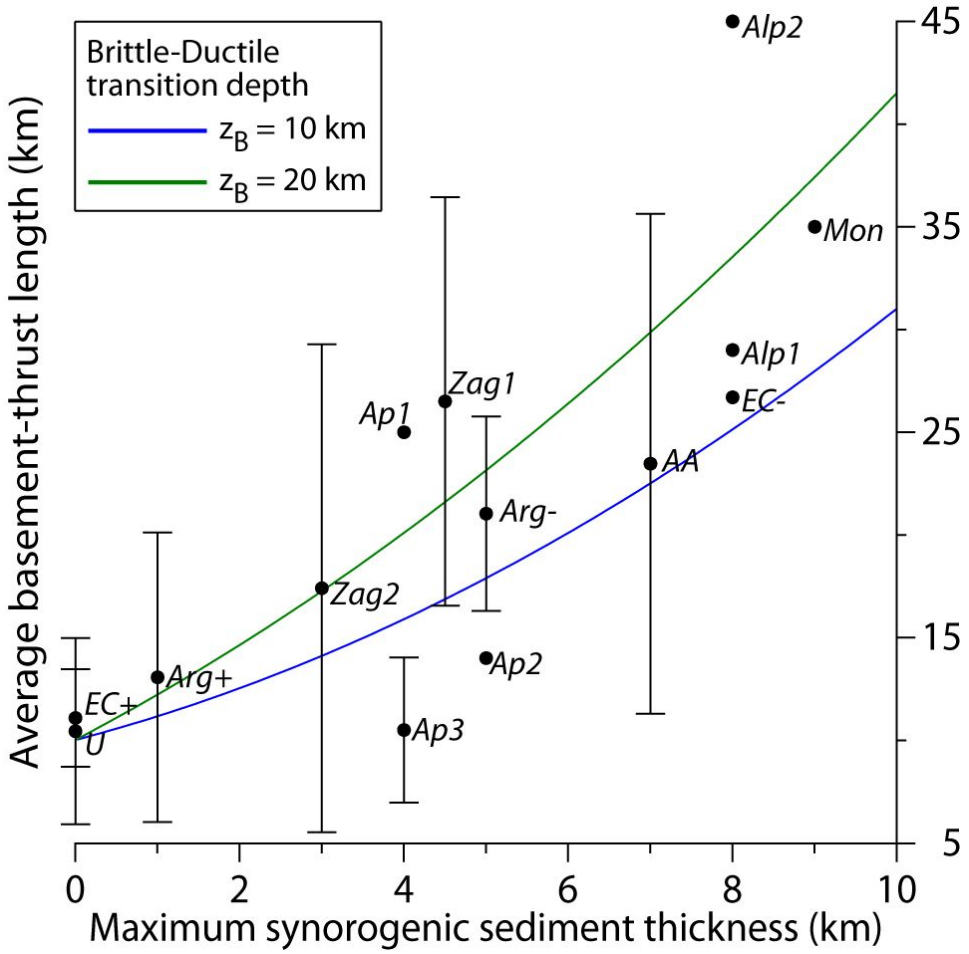

Figure 8. Cross-plot showing basement thrust-sheet length vs. syntectonic sediment thickness for a number of natural orogens. Points: Average basement thrust-sheet length plotted against the maximum syntectonic sediment thickness for the Alps (Alp1, Alp2), the Anti-Atlas (AA), the Apennines (Ap1, Ap2, Ap3), the Eastern-Cordillera (EC-, EC+), North-Monagas (Mon), the Puna plateau (Arg-, Arg+), Urals (U), Zagros (Zag1, Zag2). In case of uneven sedimentation along a section the loaded and the unloaded thrusts are plotted separately. See Table 2 for values and references. **Lines:** Basement thrust-sheet length vs. syntectonic sediment thickness relationship predicted from equation 4. See text for parameter values used.

The depositional characteristics of the natural systems are controlled by the rates of sediment produced in the orogenic system, by the sediment routing system, and by the propensity of the sediments produced to be either stored in or to bypass the orogenic foreland basin. Orogenic sediment production is partly controlled by climatic factors such as precipitation that affect erosion rates.

Mountain belt	maximum synorogenic sediment thickness	average basement thrust length	standard deviation (in case of multiple thrust sheets)	Reference
Zagros 1	3,0	17,40	11,88	Berberian (1995)
Zagros 2	4,5	26,50	9,95	Molinaro et al (2005)
Apennines 1	4,0	25,00	-	Coward et al (1999)
Apennines 2	5,0	14,00	-	Coward et al (1999)
Apennines 3	4,0	10,50	3,54	Coward et al (1999)
Puna plateau (sediment loaded)	5,0	21,03	4,74	Coutand et al (2001)
Puna plateau (sediment deprived)	1,0	13,07	7,05	Coutand et al (2001)
North Monagas thrust belt	9,0	35,00	-	Roure et al (1994)
Eastern Cordillera (sediment loaded)	8,0	26,70	-	Carrapa et al (2011)
Eastern Cordillera (sediment deprived)	0,0	11,08	2,38	Carrapa et al (2011)
Anti-Atlas	7,0	23,47	12,17	Burkhard et al (2006)
Swiss Alps 1	8,0	29,00	-	Willett & Schlunegger (2010)
Swiss Alps 2	8,0	45,00	-	Roure (2008)
Ural	0,0	10,44	4,53	Brown et al. (1997)

Table 2. Maximum synorogenic sediment thickness values (measured at the thickest point of the sediment cover), average basement thrust-sheet lengths and standard deviation of the average basement thrust-sheet lengths (if measured on more than one thrust sheet) for natural fold-and-thrust belts. In case of the Eastern Cordillera and the Puna plateau, where large variations in the sediment loading of the individual basement thrust sheets are present, we have distinguished between sediment-loaded and sediment-starved areas. References: (Berberian, 1995; Brown et al., 1997a; Burkhard et al., 2006; Carrapa et al., 2011; Coutand et al., 2002; Coward et al., 1999; Molinaro et al., 2005; Roure, 2008; Willett and Schlunegger, 2010)

For example, orographic precipitation may lead to asymmetries in erosion (Willett, 1999), and in the production, transport, and deposition of sediments, which in turn may lead to

asymmetric basement involvement in orogens. The sediment-storage potential of foreland basins, on the other hand, is mainly controlled by its drainage characteristics, with internally draining endorheic systems allowing for high sediment-storage capacity and consequent feedbacks on orogenic structure. The sediment-storage capacity of the foreland basin systems is also affected by evolving structure, with natural barriers forming as a consequence of thin-skinned external fold-and-thrust belt activity providing for creation of internally drained sediment sinks, resulting in a positive feedback into thick-skinned crustal-scale orogenic deformation (e.g. Sobel et al., 2003; Strecker et al., 2007).

6. Conclusions

The contrasting characteristics of sediment-starved and sediment-loaded orogens and their associated fold-and-thrust belts can be explained by the effects of syntectonic deposition as demonstrated by the numerical models presented here. While earlier research has predominantly focused on the effects of erosion on mountain building and on sedimentation controls on thin-skinned deformation, we have shown here that sediment loading on the external parts of an orogen provides a first-order control on its crustal-scale structural style and significantly changes its dynamics. In sediment-starved orogens, basement deformation is mostly limited to the axial orogenic zone with thin-skinned deformation in the adjacent foreland basins, whereas in sediment-loaded orogens, thick-skinned crustal-scale deformation occurs both in the axial zone and beneath the foreland with long basement thrust sheets. The presented models suggest that erosion, while strongly affecting the width of the orogenic core, has limited direct effects on the evolution of the orogenic foreland.

Our simple analytical scaling analysis indicates that basement thrust length depends quadratically on differential syntectonic sediment thickness, and on the depth and strength of the mid-crustal shear zone. Results are to first order consistent with our numerical model predictions as well as with natural observations.

The models are consistent with characteristics of numerous orogens and their associated foreland fold-and-thrust belts, and indicate a first-order control of deposition on crustal-scale structural style in these natural systems.

Acknowledgements

This study is supported by the Norwegian Research Council that funded the Norwegian component of the European Science Foundation Eurocore TOPO-Europe project PyrTec. The Bergen Center of Computational Science is acknowledged for access to computational infrastructure. We thank Cedric Thieulot for his help during the early stages of designing and setting up the model experiments.

References

Alavi, M., 2007. Structures of the Zagros fold-thrust belt in Iran. American Journal of Science 307, 1064-1095.

Avouac, J.P., 2003. Mountain building, erosion and the seismic cycle in the Nepal Himalaya. Adv. Geophys. 46, 1-79.

Berberian, M., 1995. Master Blind Thrust Faults Hidden under the Zagros Folds - Active Basement Tectonics and Surface Morphotectonics. Tectonophysics 241, 193-224.

Bonnet, C., Malavieille, J., Mosar, J., 2007. Interactions between tectonics, erosion, and sedimentation during the recent evolution of the Alpine orogen: Analogue modeling insights. Tectonics 26.

Bos, B., Spiers, C.J., 2002. Frictional-viscous flow of phyllosilicate-bearing fault rock: Microphysical model and implications for crustal strength profiles. J Geophys Res 107.

Brooks, B.A., Bevis, M., Whipple, K., Ramon Arrowsmith, J., Foster, J., Zapata, T., Kendrick, E., Minaya, E., Echalar, A., Blanco, M., Euillades, P., Sandoval, M., Smalley, R.J., 2011. Orogenic-wedge deformation and potential for great earthquakes in the central Andean backarc. Nature Geoscience 4, 380-383.

Brown, D., Alvarez-Marron, J., Perez-Estaun, A., 1997a. Preservation of a subcritical wedge in the south Urals foreland thrust and fold belt. J Geol Soc London 154, 593-596.

Brown, D., Alvarez-Marron, J., Perez-Estaun, A., Gorozhanina, Y., Baryshev, V., Puchkov, V., 1997b. Geometric and kinematic evolution of the foreland thrust and fold belt in the southern Urals. Tectonics 16, 551-562.

Burkhard, M., Caritg, S., Helg, U., Robert-Charrue, C., Soulaimani, A., 2006. Tectonics of the Anti-Atlas of Morocco. Comptes Rendus Geoscience 338, 11-24.

Carrapa, B., Trimble, J.D., Stockli, D.F., 2011. Patterns and timing of exhumation and deformation in the Eastern Cordillera of NW Argentina revealed by (U-Th)/He thermochronology. Tectonics 30.

Cederbom, C.E., van der Beek, P., Schlunegger, F., Sinclair, H.D., Oncken, O., 2011. Rapid extensive erosion of the North Alpine foreland basin at 5-4Ma. Basin Research 23, 528-550.

Coutand, I., Strecker, M.R., Arrowsmith, J.R., Hilley, G., Thiede, R.C., Korjenkov, A., Omuraliev, M., 2002. Late Cenozoic tectonic development of the intramontane Alai Valley, (Pamir-Tien Shan region, central Asia): An example of intracontinental deformation due to the Indo-Eurasia collision. Tectonics 21, 3-1-3-19.

Coward, M.P., De Donatis, M., Mazzoli, S., Paltrinieri, W., Wezel, F.-C., 1999. Frontal part of the northern Apennines fold and thrust belt in the Romagna-Marche area (Italy): Shallow and deep structural styles. Tectonics 18, 559-574.

Dahlen, F.A., 1990. Critical Taper Model of Fold-and-Thrust Belts and Accretionary Wedges. Annual Review of Earth and Planetary Sciences 18, 55-99.

Davis, D., Suppe, J., Dahlen, F.A., 1983. Mechanics of Fold-and-Thrust Belts and Accretionary Wedges. Journal of Geophysical Research 88, 1153-1172.

DeCelles, P.G., Giles, K.A., 1996. Foreland basin systems. Basin Research 8, 105-123.

Ellis, S., Beaumont, C., Jamieson, R.A., Quinlan, G., 1998. Continental collision including a weak zone: the vise model and its application to the Newfoundland Appalachians. Can J Earth Sci 35, 1323-1346.

Fillon, C., Huismans, R.S., van der Beek, P., 2012. Syntectonic sedimentation effects on the growth of fold-and-thrust belts. Geology 41, 83-86.

Ford, M., 2004. Depositional wedge tops: interaction between low basal friction external orogenic wedges and flexural foreland basins. Basin Research 16, 361-375.

Gleason, G.C., Tullis, J., 1995. A Flow Law for Dislocation Creep of Quartz Aggregates Determined with the Molten-Salt Cell. Tectonophysics 247, 1-23.

Guellec, S., Lajat, D., Mascle, A., Roure, F., Tardy, M., 1990. Deep seismic profiling and petroleum potential in the western Alps: Constraints with ECORS data, balanced cross-sections and hydrocarbon modeling, in: Pinet, B., Bois, C. (Eds.), The Potential of Deep Seismic Profiling for Hydrocarbon Exploration. Edition Technip, Paris, pp. 425-437.

Hardy, S., Duncan, C., Masek, J., Brown, D., 1998. Minimum work, fault activity and the growth of critical wedges in fold and thrust belts. Basin Research 10, 365-373.

Huismans, R.S., Beaumont, C., 2003. Symmetric and asymmetric lithospheric extension: Relative effects of frictional-plastic and viscous strain softening. J Geophys Res 108.

Karato, S., Wu, P., 1993. Rheology of the upper mantle: a synthesis. Science 260, 771-778.

Konstantinovskaia, E., Malavieille, J., 2005. Erosion and exhumation in accretionary orogens: Experimental and geological approaches. Geochemistry Geophysics Geosystems 6.

Koons, P.O., 1990. Two-sided orogen: Collision and erosion from the sand box to the Southern Alps, New Zealand. Geology 18, 679-682.

Madritsch, H., Fabbri, O., Hagedorn, E.M., Preusser, F., Schmid, S.M., Ziegler, P.A., 2010. Feedback between erosion and active deformation: geomorphic constraints from the frontal Jura fold-and-thrust belt (eastern France). International Journal of Earth Sciences 99, S103-S122.

Masek, J.G., Duncan, C.C., 1998. Minimum-work mountain building. Journal of Geophysical Research 103, 907.

Molinaro, M., Leturmy, P., Guezou, J.C., Frizon de Lamotte, D., Eshraghi, S.A., 2005. The structure and kinematics of the southeastern Zagros fold-thrust belt, Iran: From thin-skinned to thick-skinned tectonics. Tectonics 24, 3.

Mosar, J., 1999. Present-day and future tectonic underplating in the western Swiss Alps: reconciliation of basement/wrench-faulting and decollement folding of the Jura and Molasse basin in the Alpine foreland. Earth and Planetary Science Letters 173, 143-155.

Mouthereau, F., Watts, A.B., Burov, E., 2013. Structure of orogenic belts controlled by lithosphere age. Nature Geoscience 6, 785-789.

Roure, F., 2008. Foreland and Hinterland basins: what controls their evolution? Swiss Journal of Geosciences 101, 5-29.

Sibson, R.H., 1990. Conditions for fault-valve behaviour. Geol. Soc. Spec. Publ. 54, 15–28.

Sobel, E.R., Hilley, G.E., Strecker, M.R., 2003. Formation of internally drained contractional basins by aridity-limited bedrock incision. Journal of Geophysical Research 108, 2344, doi:2310.1029/2002JB001883.

Stolar, D.B., Willett, S.D., Roe, G.H., 2006. Climatic and tectonic forcing of a critical orogen. Geological Society of America Special Paper 398, 241-250.

Storti, F., McClay, K., 1995. Influence of Syntectonic Sedimentation on Thrust Wedges in Analog Models. Geology 23, 999-1002.

Strecker, M.R., Alonso, R.N., Bookhagen, B., Carrapa, B., Hilley, G.E., Sobel, E.R., Trauth, M.H., 2007. Tectonics and Climate of the Southern Central Andes. Annual Review of Earth and Planetary Sciences 35, 747-787.

Thieulot, C., 2011. FANTOM: Two- and three-dimensional numerical modelling of creeping flows for the solution of geological problems. Physics of the Earth and Planetary Interiors 188, 47-68.

Whipple, K.X., 2009. The influence of climate on the tectonic evolution of mountain belts. Nature Geoscience 2, 97-104.

Willett, S.D., 1999. Orogeny and orography: The effects of erosion on the structure of mountain belts. J Geophys Res 104, 28957-28981.

Willett, S.D., Schlunegger, F., 2010. The last phase of deposition in the Swiss Molasse Basin: from foredeep to negative-alpha basin. Basin Research 22, 623-639.

Paper III

Extensional inheritance and surface processes as controlling factors of mountain belt structure

Zoltán Erdős[1,2], Ritske S. Huismans[1], and Peter van der Beek[2]

[1]Department of Earth Sciences, University of Bergen, Bergen, N-5007, Norway

[2]Institut des Sciences de la Terre (ISTerre), Université Joseph Fourier, Grenoble, 38041, France

Corresponding author: Zoltán Erdős, University of Bergen, N-5007 Bergen, Norway (zoltan.erdos@geo.uib.no)

Key Points

We use 2D thermo-mechanical models to study multi-scale inversion tectonics.

Extensional inheritance facilitates the deformation of the overriding plate.

Basement deformation has a control on thin-skinned fold-and-thrust belts.

Abstract

Surface processes and inherited structures are widely regarded as factors that strongly influence the evolution of mountain belts. The first-order effects of these parameters have been studied extensively throughout the last decades, but their relative importance remains notoriously difficult to assess and document. We use lithospheric scale plane-strain thermo-mechanical model experiments to study the effects of surface processes and extensional inheritance on the internal structure of contractional orogens and their foreland basins. Extensional inheritance is modeled explicitly by forward modeling the formation of a rift basin before reversing the velocity boundary conditions to model its inversion. Surface processes are modeled through the combination of a simple sedimentation algorithm, where all negative topography is filled up to a prescribed reference level, and an elevation-dependent erosion model. An additional sensitivity test to upper crustal strength is included. Our results show that (1) extensional inheritance facilitates the propagation of basement deformation in the retro-wedge and (2) increases the width of the orogen; (3) sedimentation increases the length-scale of both thin-skinned and thick-skinned thrust sheets and (4) results in a wider orogen; (5) erosion helps to localize deformation resulting in a narrower orogen; (6) a weaker than average upper crust results in a wider orogen with lower topography. A comparison of the modeled

behaviors to the High Atlas, the Pyrenees and the Central Alps, three extensively studied natural examples characterized by different stages of inversion, is presented and confirms the predicted controls of surface processes and extensional inheritance on orogenic structure.

Index terms and Keywords

Continental contractional orogenic belts and inversion tectonics, Rheology: crust and lithosphere, Tectonics and landscape evolution

Numerical modeling, Surface processes

1 Introduction

The crustal structure of collisional orogens around the world shows a wide range of deformation styles from narrow, asymmetric doubly vergent wedges like the Pyrenees (Muñoz, 1992) to wide, plateau-like orogens such as the Zagros mountain belt in Iran (Mouthereau et al., 2007). Recently, Jamieson and Beaumont (2013) proposed a conceptual temperature-magnitude framework for orogenesis in terms of the progression from small-cold to large-hot orogens. In this framework, small-cold orogens are defined to be those in which the upper part of the lithospheric mantle subducts with little internal deformation and bulk shortening and where crustal thickening and heating are limited, while large-hot orogens are typically composed of a central elevated plateau underlain by thick crust and underthrusted continental lithosphere, and characterized by major internal deformation, strong heating and ductile flow of the middle-lower crust.

In this framework, the most important controlling factor on the size and overall structure of an orogen is the amount of convergence between the colliding plates. However, in addition to the

amount of convergence, several other factors have been proposed to provide a first-order control on the structural development of mountain belts, including bulk crustal strength, inherited weaknesses, and the efficiency of surface process. While these parameters have been studied extensively in the last decades (e.g., Buiter, 2012; Jammes and Huismans, 2012; Mouthereau et al., 2013; Mugnier et al., 1997; Stolar et al., 2006; Willett et al., 1993) their relative importance remains largely unexplored.

Numerous studies have shown that the strength of the crust and the mantle lithosphere provide first-order controls on the structural style in both extensional (Bassi et al., 1993; Buck, 1991; Buck et al., 1999; Huismans and Beaumont, 2003; 2011; Huismans et al., 2005; Jammes and Huismans, 2012) and contractional (Beaumont et al., 1994; Ellis et al., 1998; Jammes and Huismans, 2012; Willett et al., 1993) settings. In addition, as Jammes and Huismans (2012) pointed out recently, the strength of the crust is highly dependent on inherited compositional and structural weaknesses. Although most orogens initiate by inversion of passive margins or rifted basins, little is known about how inherited extensional structures affect the evolution of these orogens. Jammes and Huismans (2012) demonstrated that rifting inheritance can explain the presence of a lower crustal or mantle lithospheric body at shallow depth, as inferred for the Pyrenees (Muñoz, 1992) and European Alps (Schmid and Kissling, 2000) for example. Extensional inheritance also appears to facilitate the propagation of deformation to the retro-wedge of the orogen (Jammes and Huismans, 2012). However, their modeling study focused mainly on the thick-skinned crustal scale evolution of mountain belts with numerical model resolution insufficient to properly address the link with thin-skinned structures and processes acting at the Earth's surface.

Following the realization that erosion and mountain building are coupled, i.e. that, erosion is not only a superficial process driven by mountain building but that it has potentially strong feedbacks on the development of the internal structure of orogens (Beaumont et al., 1992; Willett, 1999), the effects of erosional processes on the tectonic evolution of mountain belts have been extensively studied (see Whipple, 2009 and references therein). It has also been shown that syntectonic sedimentation has a strong control on the structure of thin-skinned fold-and-thrust belts (e.g., Bonnet et al., 2007; Fillon et al., 2012; Ford, 2004; Storti and McClay, 1995), where the erosion products from the orogenic hinterland can stabilize the belt in accordance with critical-taper theory (Dahlen, 1990). However, despite our improved understanding of the control exerted by surface processes on the evolution of contractional orogens it is still unclear how they might affect mountain building in the presence of inherited extensional structures. Neither has much work been done to decipher which aspects of orogenic structure and evolution can be ascribed to tectonic inheritance or to surface processes specifically, and which of these provide the prime control on the structure of individual mountain belts.

Here we study the effect and relative importance of inherited extensional structures and surface processes on the deformation style of collisional orogens as well as their adjacent foreland fold-and-thrust belts. We investigate the effects of extensional inheritance by modeling the formation of a continental rift basin explicitly before the velocity boundary conditions are inverted to create a contractional environment for the development of a doubly vergent orogen. In this “accordion” modeling approach (using the term coined by Jammes and Huismans (2012)) the structure predicted by an extensional model is used as the initial

conditions for modeling inversion tectonics. The effects of sedimentation are included using a simple model where the topography is filled up with sediments to a reference level while erosion is modeled with an elevation-dependent algorithm. A first-order comparison of our model results with natural examples from the High Atlas, the Pyrenees and the European Alps suggests that our model experiments can be used to explain characteristic features of these and other natural systems.

2 Methodology

2.1 Basic principles

We use a modified version of the Arbitrary Lagrangean-Eulerian finite-element code FANTOM to solve the Stokes and the heat-transport equations in a fully coupled manner (Thieulot, 2011). We model thermo-mechanically coupled, plane-strain, incompressible viscous-plastic creeping flows to investigate the behavior of a layered lithosphere with frictional-plastic and thermally activated power-law viscous rheologies in both extensional and contractional regimes.

When stress is below the yield criterion, the deformation is viscous; frictional-plastic deformation is activated when the stress exceeds the yield criterion. The numerical accuracy of the finite-element code has been verified through benchmarking against a wide range of analytical and numerical studies (Thieulot, 2011).

Viscous-flow deformation follows temperature-dependent nonlinear power-law rheologies. The effective viscosity η_{eff} is specified as:

$$\eta_{eff}=fA^{-1/n}.\dot{\varepsilon}^{(1-n)/2n}.\exp\left(\frac{Q+Vp}{nRT}\right) \quad (1)$$

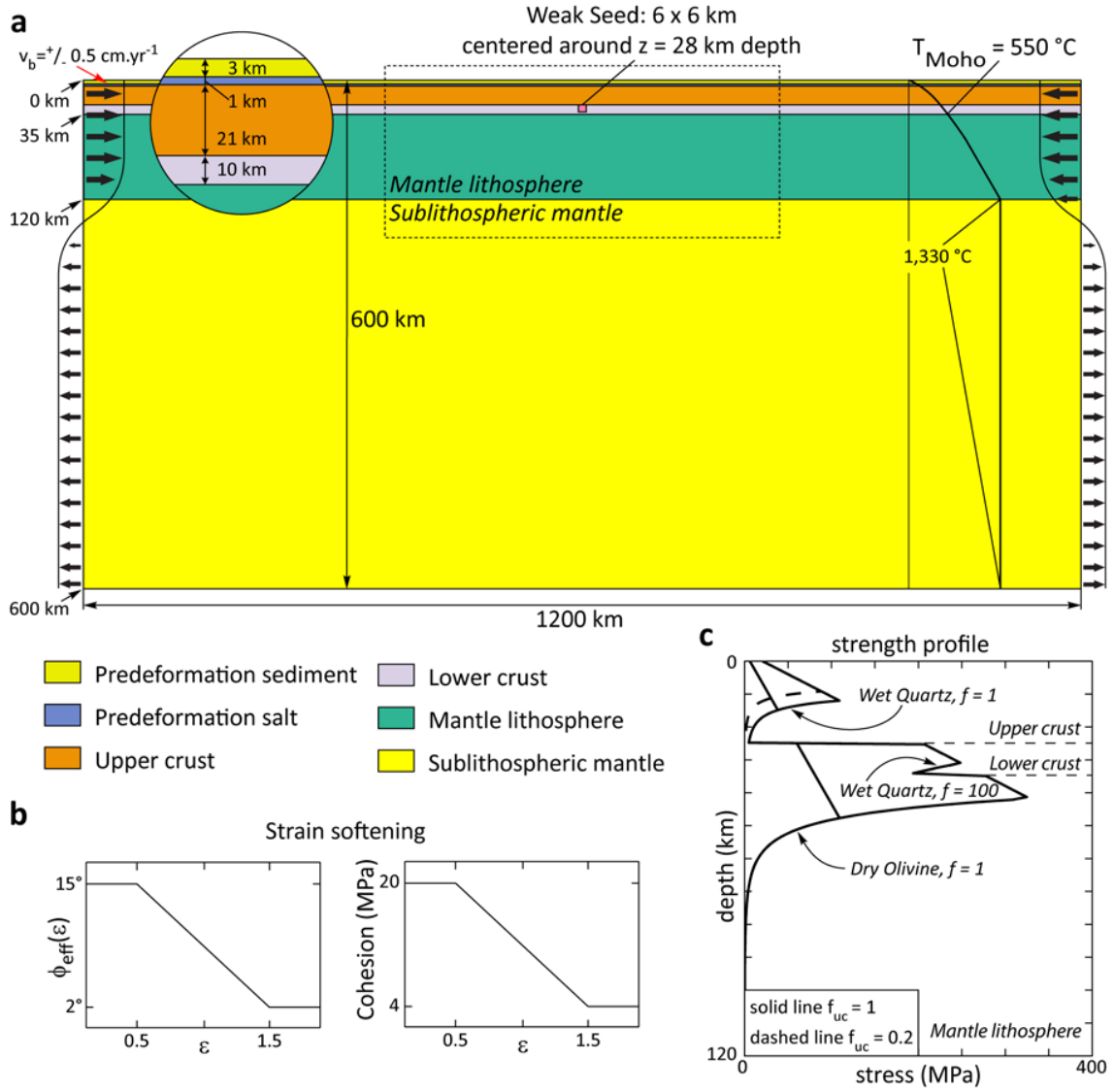

Figure 1 (a) Model geometry showing layer thicknesses, the position and size of the weak seed, the lateral velocity boundary conditions and the initial temperature profile. All values used for the mechanical and thermal parameters are listed in Table 1. The lateral velocity boundary condition is set up to achieve mass balance. Extension and contraction are driven by the velocity boundary conditions and seeded by a small strain-weakened region. **(b)** Frictional plastic strain softening is achieved through a linear decrease of ϕ_{eff} from 15° to 2° with a simultaneous decrease of C from 20 MPa to 4 MPa. **(c)** The initial strength profiles of the models. The continuous and dashed lines represent the profile of models with wet quartz upper crust using a scaling factor f_{uc}=1 and f_{uc}=0.2, respectively.

Where A is the pre-exponential scaling factor, n is the power-law exponent, $\dot{\varepsilon}$ is the second invariant of the deviatoric strain rate tensor, Q is the activation energy, V is the activation volume, p is the pressure, T is the temperature and R is the universal gas constant. A, n, Q and V are derived from laboratory measurements carried out on 'wet' and 'dry' olivine and 'wet' quartzite (Gleason and Tullis, 1995; Karato and Wu, 1993) and are given in Table 1. The factor f is used to scale viscosities calculated from the reference 'wet' quartzite flow law for the lower crust. The effective viscosity of the crust remains largely unconstrained (Huismans and Beaumont, 2003); the applied viscosity scaling represents a simple technique that can be used to create strong lower crust without recourse to additional flow laws that are subject to significant uncertainties.

Frictional-plastic yielding is modeled with a pressure-dependent Drucker-Prager yield criterion, equivalent to the Coulomb yield criterion, when modeling incompressible deformation in plane-strain. Yielding occurs when:

$$(J_2^{'})^{1/2} = p \sin\phi_{eff} + C \cos\phi_{eff} \qquad (2)$$

Where $J_2^{'}$ is the second invariant of the deviatoric stress, φ_{eff} is the effective internal angle of friction given as $psin(\phi_{eff}) = (p-p_f)sin(\phi)$ for pore fluid pressure p_f, and cohesion C. With appropriate choice of C and ϕ_{eff} this yield criterion can approximate the effect of pore fluid pressure and frictional sliding in rocks. High transient or static fluid pressures or mineral transformations can cause the weakening of frictional-plastic faults and shear zones (Bos and Spiers, 2002; Sibson, 1990; Streit, 1997). In the model, these strain-softening effects are accounted for through a linear decrease of ϕ_{eff} from 15° to 2° with a simultaneous decrease of

C from 20 MPa to 4 MPa for strain values between 0.5 and 1.5 (Figure 1b). We note that $\phi_{eff}(\varepsilon) \approx 15°$ corresponds to the effective ϕ when the pore fluid pressure is approximately hydrostatic.

The mechanical and thermal systems are coupled through the temperature-dependent rheologies and are solved sequentially for each model time step. The temperature dependence of the densities is given by:

$$\rho(T)=\rho_0(1-\alpha(T-T_0)) \quad (3)$$

with the thermal expansion coefficient $\alpha = 3.1 \times 10^{-6}$ °C^{-1} for the crust and $\alpha = 0$ °C^{-1} for the mantle. The reference densities of the individual materials at $T_0 = 0$ °C temperature are given in Table 1. A compositional density contrast of 60 kg m^{-3} between the mantle lithosphere and sublithospheric mantle is applied in order to avoid small-scale mantle-flow instabilities.

2.2 Model setup

The models are set up as an idealized representation of the lithosphere and the sublithospheric mantle in a 600 km high and 1200 km wide box (Figure 1a). The lithosphere consists of a 35 km thick crust (25 km upper crust, 10 km lower crust) and 85 km mantle lithosphere overlying the sublithospheric mantle. The top 4 km of the crust represent pre-rift sediments composed of a 3 km thick frictional upper layer overlying a 1 km thick weak layer representing a décollement level (e.g., evaporite). This setup allows for modeling the behavior of pre-rift sedimentary sequences as well as the deformation of the underlying continental basement, providing insight into the potential coupling and interaction of thin-skinned and thick-skinned tectonic regimes.

The Eulerian grid consists of 2400 elements in the horizontal and 300 elements in the vertical dimension, respectively. The distribution of the elements is irregular in the vertical direction, with 125 elements in the upper crust, 125 elements in the lower crust and mantle lithosphere, and 50 elements in the sublithospheric mantle. Consequently, the resolution in the horizontal direction is equal to 500 m for the entire model domain, while the vertical resolution is 200 m in the upper crust, 800 m in the lower crust and mantle lithosphere, and 9.5 km in the sublithospheric mantle.

Units	Salt	Upper Crust + Pre-collision Sediment	Lower Crust	Mantle Lithosphere	Sublithospheric Mantle
			Mechanical Parameters		
Thickness (km)	1	21 + 3	10	85	480
Reference density (kg m^{-3})	2300	2800	2800	3360	3300
Internal friction angle $\phi_{eff}(\varepsilon)$	2°	15° - 2°	15° - 2°	15° - 2°	15° - 2°
Strain range of softening	-	0.5-1.5	0.5-1.5	0.5-1.5	0.5-1.5
Cohesion (Pa)	-	2.10^7 - 4.10^6	2.10^7 - 4.10^6	2.10^7 - 4.10^6	2.10^7 - 4.10^6
Flow law	-	Wet Quartz[2]		Dry Olivine[3]	Wet Olivine[3]
scaling factor (f)	-	1, 0.2	100	1	1
A (Pa^{-n} s^{-1})	-	$8.574\ 10^{-28}$	$8.574\ 10^{-28}$	$2.4168\ 10^{-15}$	$1.393\ 10^{-14}$
Q (J mol^{-1})	-	$222.81\ 10^3$	$222.81\ 10^3$	$540.41\ 10^3$	$429.83\ 10^3$
N	-	4	4	3.5	3
V (m^3 mol^{-1})	-	$3.1\ 10^{-6}$	$3.1\ 10^{-6}$	$25\ 10^{-6}$	$15\ 10^{-6}$
R (J mol^{-1} °C^{-1})			8.3144		
			Thermal Parameters		
Thermal diffusivity (m^2 s^{-1})	$1\ 10^{-6}$	$1\ 10^{-6}$	$1\ 10^{-6}$	$1\ 10^{-6}$	$1\ 10^{-6}$
Thermal expansion (K^{-1})	$3.1\ 10^{-5}$	$3.1\ 10^{-5}$	$3.1\ 10^{-5}$	0	0
Heat productivity (W m^{-3})	$0.8\ 10^{-6}$	$0.8\ 10^{-6}$	$0.8\ 10^{-6}$	0	0

Table 1. Mechanical and thermal parameters used in the model experiments.

A free surface at the top of the numerical model allows for tracking directly the evolution of the topography. All model experiments utilize a simple numerical diffusion-based surface

smoothing algorithm to prevent numerical instabilities. Velocity boundary conditions are imposed on both vertical sides of the model while a free slip condition is applied at its base. In extensional mode, material is flowing out through both sidewalls of the model in the lithosphere with a velocity v = 0.5 cm/yr, while material is flowing in through both sidewalls in the sublithospheric mantle with a velocity scaled to balance the outflow of lithospheric material (Figure 1a). In convergence mode, the side boundary conditions are inverted.

The lateral boundaries are thermally insulated (i.e., heat flow is not allowed through the boundary), while the top and basal boundaries are set to a constant temperature (Figure 1a). The initial temperature field is laterally uniform and increases parabolically with depth from the surface (T_0 = 0 °C) to the base of the crust (initial Moho temperature, T_m = 550 °C) as a result of heat production in the crust (h_c=0.8 10^{-6} Wm^{-3}). Below the Moho, temperature follows a linear gradient to the base of mantle lithosphere (initially at T = 1330 °C); the temperature of the sublithospheric mantle is initially constant and uniform.

The numerical models have a depth-dependent rheology in which the crust is characterized by the viscous creep parameters for wet quartz (Gleason and Tullis, 1995). A scaling factor f_{lc}=100 is used to obtain a strong lower crust. The mantle lithosphere is characterized by the viscous flow parameters of dry olivine (Karato and Wu, 1993) while the sublithospheric mantle is characterized by viscous flow parameters for wet olivine (Karato and Wu, 1993). Using these parameters in the reference model, the upper crust (including the pre-collision sediments), the upper part of the strong lower crust and the top of the mantle lithosphere undergo frictional-plastic deformation, while the middle crust, the lower part of the lower crust, and the lower mantle lithosphere and sub-lithospheric mantle deform viscously (Figure 1c).

Model	Upper Crustal Scaling Factor	Lower Crustal Scaling Factor	Amount of extension	Sedimentation (start)	Erosion (rate)	Figure
M1 (reference)	1	100	50 km	-	-	Figure 2
M2	1	100	-	-	-	Figure 3
M3	1	100	100 km	-	-	Figure 4
M4	1	100	50 km	20 My	-	Figure 5
M5	1	100	50 km	20 My	$4.35*10^{-15}$	Figure 6
M6	1	100	50 km	20 My	$8.7*10^{-15}$	Figure 7
M7	0.2	100	50 km	-	-	Figure 8

Table 2. List of model experiments and their varying parameters.

2.3 Surface processes

The reference model (Model 1) does not account for sedimentation and erosion. The top of the model is acting as a free surface with only minimal surface smoothing applied to prevent numerical instabilities (see previous section).

In models M2-M4, a simple sedimentation model is applied. Deposition starts after 100 km of crustal shortening has taken place beyond full inversion, and is modeled by filling all topography below a reference level with sediments at the end of each time step. The delayed initiation of sedimentation allows for the development of a more than 2-km high orogenic core that could provide a source for the sediments. This representation of sedimentation is very simple but the resulting geometry of the basin fill is consistent with natural foreland basin systems (DeCelles and Giles, 1996).

In models M3 and M4, an elevation-dependent erosion algorithm is implemented following the equation $\Delta h/\Delta t = h.E_r$, where h is elevation, Δt is time (s) and E_r is the characteristic inverse erosional timescale (s^{-1}). E_r is scaled such that in model M3 a 4-km high topography erodes by 1

km in 2 Myr, while in model M4 this will take place in 1 Myr. Note that material that was initially deposited in the model can be eroded when elevated above the reference base level.

3 Results

A full list of models presented and their key parameters is provided in Table 2. Following the reference model (model M1; Figure 2), a set of models is presented that investigates the effect of varying the amount of initial extension on lithosphere-scale inversion and contraction (models M2 and M3; Figures 3 to 4). Subsequently, the effects of surface processes (erosion/deposition) on the evolution of an orogen formed by inversion of a rift basin are explored (models M4 to M6; Figures 5, 6 and 7). Finally, a model with weakened upper crust is presented to test the sensitivity of orogenic development to upper crustal strength (model M7; Figure 8).

3.1 Reference model: model M1

The reference model starts in extensional mode with 50 km extension applied in 5 Myr before the velocity boundary conditions are reversed, creating contraction for the rest of the model experiment. The reference model has a moderately weak decoupling horizon in the middle crust and a strong lower crust, with crustal scaling factors f_{uc}=1 and f_{lc}=100. Neither sedimentation nor erosion are allowed for during the experiment. The model run can be divided into four phases that each display fundamentally different behavior (Figure 2). During Phase 1, extension leads to the formation of a largely symmetric continental rift basin bounded by two well-defined frictional-plastic normal shear zones. By the end of this phase (at t=5 Myr and 50 km extension) the strong lower crust is ruptured (Figure 2a), the rift basin is about 4 km

deep at its deepest point, while the rift shoulders reach up to 1 km above the reference level. The pre-rift sediments display very little deformation.

Phase 2 starts with the inversion of the velocity boundary conditions. By t=10 Myr (after 50 km contraction, equal to the amount of initial extension), the extensional basin is fully inverted. A mildly asymmetric keystone structure with a lower-crustal/mantle-lithospheric root is uplifted along the inverted frictional-plastic shear zones (Figure 2b).

At this point, one of the inherited frictional-plastic shear zones is preferred over the other, leading to the initiation of continental subduction. The pre-rift sediment layer on top of the keystone structure gradually thins out as material slides down along the décollement layer towards the foredeep depressions on either side of the keystone block. At the same time, the first thin-skinned thrust sheets form in the footwall of the uplifted central block.

During Phase 3, deformation migrates into the subducting plate and starts building up the pro-wedge as a result of the continuing contraction (note that we use the terms pro-wedge and retro-wedge to define the deformed parts of the lower and upper plate, respectively, as defined by Ellis et al. (1998)). An outward propagating sequence of basement thrust sheets forms (Figure 2c) with thin-skinned deformation focused in the footwall of the active basement thrusts throughout the entire model experiment (see also Figures 2d and 2e). The sequence is only disrupted by the formation of a crustal-scale pop-up structure early on in its development, after abandonment of the first basement thrust sheet. The initial keystone structure that makes up the bulk of the retro-wedge is slowly translated along the inverted normal fault bounding the overriding plate, with thin-skinned deformation occurring in the footwall of the basement

fault above the shallow décollement. The overriding plate itself remains relatively undeformed until 30 Myr.

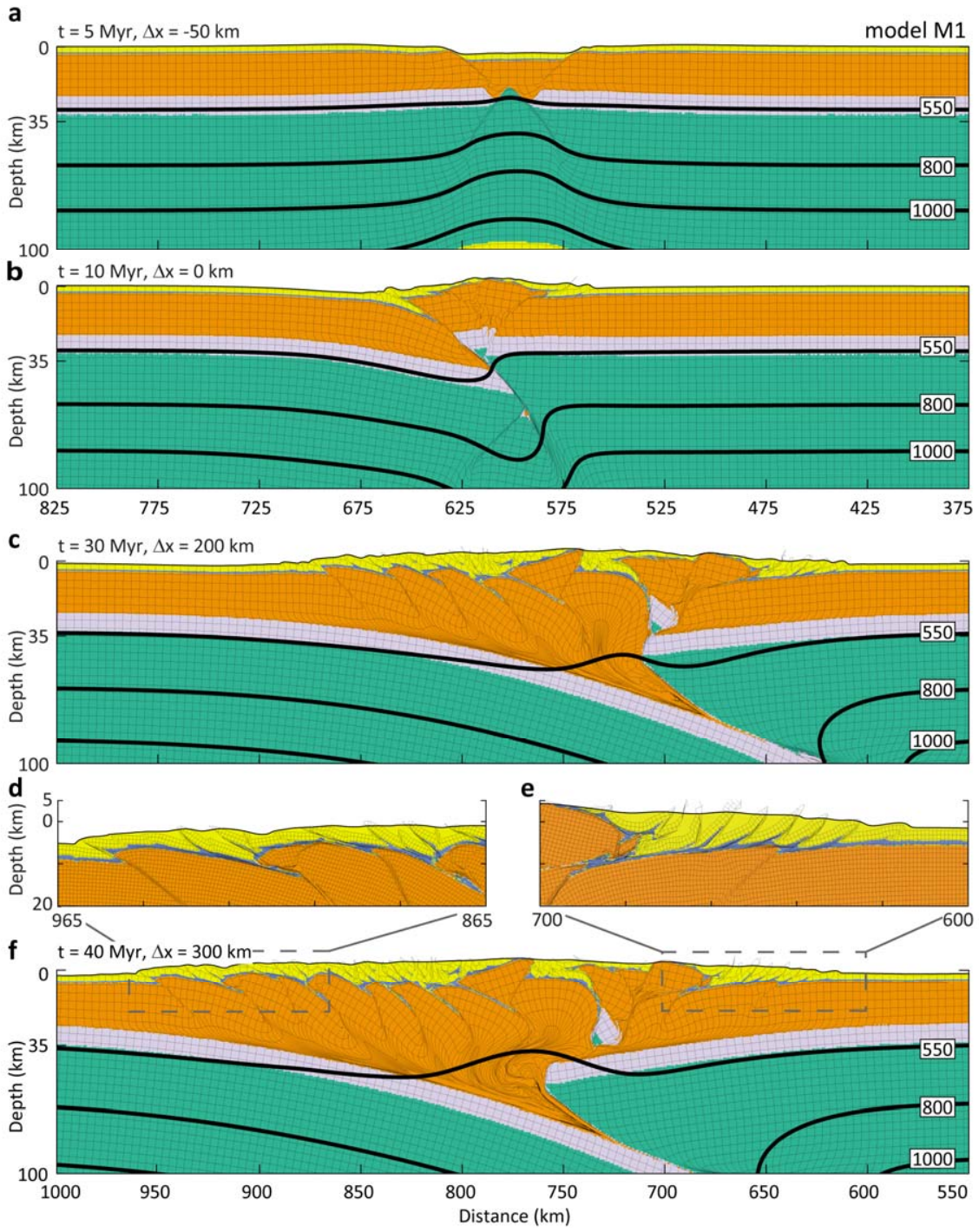

Figure 2. Reference model (M1) with no surface processes, showing deformed Lagrangean mesh and sample isotherms after **(a)** 5 Myr (Δx = -50 km) extension **(b)** 10 Myr (Δx = 0 km) full inversion **(c)** 30 Myr (Δx = 200 km) contraction and **(f)** 40 Myr (Δx = 300 km) contraction for dashed area in Figure 1. **(d)** and **(e)** are zoomed extracts from Figure 2f to show the small-scale deformation patterns in the foreland fold-and-thrust belts. (Animations of model evolutions can be found in the online Supplementary Material)

During the final phase, pro-wedge deformation continues while the entire mass of the initial keystone structure including its lower-crustal root is thrusted onto the overriding plate, bending it gently down towards the subduction zone. Deformation penetrates the previously undeformed basement of the overriding plate and two thick-skinned thrust sheets form, widening the retro-wedge significantly (Figure 2f). The displacement along the individual basement thrusts in the retro-wedge is notably less than in the pro-wedge.

3.2 Model sensitivity to the amount of extension: models M2 and M3

Models M2 and M3 test the effect of the amount of extension on the structural style of lithospheric inversion. In model M2, the effect of extensional inheritance is removed by running the model in contractional mode only (model M2; Figure 3). In model M3, in contrast, the extensional mode is run until full crustal break-up before inverting the velocity boundary conditions (model M3; Figure 4). Neither sedimentation nor erosion is allowed for in both these experiments. These two models can be considered as opposite end-members in terms of the amount of inherited extensional structures.

3.2.1 Pure contraction: model M2

The effects of extensional inheritance on mountain building can be understood best in comparison to a purely contractional model. In the absence of extension, the development of model M2 (Figure 3) can be divided into two phases. During Phase 1, shortening results in the

uplift of a symmetrical keystone structure, narrower than in the reference model with extension, with foreland depressions developing on either side. The keystone structure incorporates very little lower-crustal material and no mantle lithosphere at all. Continental subduction is initiated as soon as deformation localizes preferentially on one of the shear-zones bounding the keystone structure, accommodating shortening within the strong lower crust and mantle lithosphere. The small lower-crustal root of the keystone structure remains close to the top of the undeformed lower crust of the overriding plate throughout the model experiment.

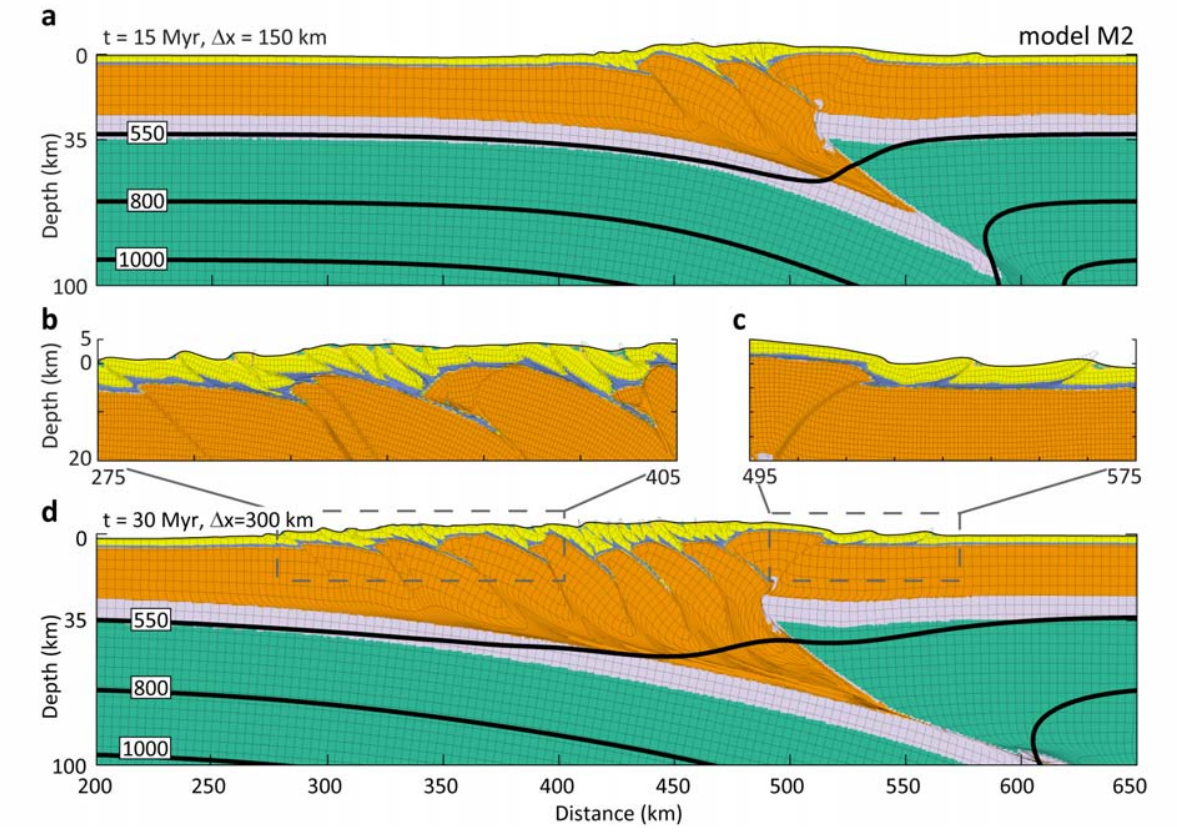

Figure 3. Pure contractional model M2 after **(a)** 15 Myr (Δx = 150 km) contraction and **(d)** 30 Myr (Δx = 300 km) contraction respectively; **(b)** and **(c)** are zoomed extracts from Figure 3d to show the small-scale deformation patterns in the foreland fold-and-thrust belts. Sedimentation and erosion are not accounted for.

With continued crustal shortening, thin-skinned thrust sheets form in the footwall of the keystone structure, detaching in the décollement layer at the base of the pre-orogenic sediments, while deformation in the crust propagates towards the foreland in the subducting plate with the formation of a basement thrust sheet (Figure 3a).

Subsequently, contraction is accommodated in turn by the formation of new basement thrust sheets propagating to the foreland, and by the formation of thin-skinned thrusts in the pre-collision sediments in the footwall of the active basement thrust sheet (Figure 3b-d). The overriding plate remains relatively undeformed throughout the model evolution, developing a single basement thrust sheet and only limited thin-skinned deformation after 300 km of contraction (Figure 3c-d).

3.2.2 Full break-up: model M3

In model M3, 100 km of initial extension results in full continental break-up (Figure 4a). The model experiment can be divided into four phases (Figure 4a-f). During the first phase, early rupture of the strong lower crust is followed by the formation of a wide, asymmetric rift basin with three rotated upper-crustal fault blocks that are situated directly on top of the extended mantle lithosphere. This phase ends with full crustal break-up after 10 Myr and 100 km of extension, leading to exhumation of mantle lithosphere (Figure 4a). The rift basin is about 5 km deep at its deepest point, while the rift flanks reach elevations up to 1.5 km. The pre-rift sediments display only minor deformation as they slide off from the tilted corners of the rotated fault blocks. No significant thin-skinned fault activity is apparent at this stage. Phase 2 starts at the onset of inversion. During this phase, which lasts until 20 Myr, inversion of the pre-existing extensional structures leads to a wider and more complex asymmetric keystone

structure, which is uplifted along the most external inverted normal faults. Several smaller inversion structures develop in between these master faults, reflecting the complex structure of the rift basin (Figure 4b). The keystone structure involves only a marginally larger amount of lower crust and mantle lithosphere at its root, in comparison with the reference model that experienced less extension (Figure 2b). Thin-skinned deformation of the pre-rift sediments is minimal at this stage, with a few thrusts developing in the footwalls of the inverted extensional structures.

Phase 3 of the model evolution and onward is very similar to that of the reference model (Figure 4c-d). Deformation migrates into the subducting plate, building up the pro-wedge through an outward-propagating sequence of basement thrust sheets. This sequence is again temporarily interrupted by the formation of a crustal-scale pop-up structure (Figure 4c; compare to Figure 2c). Thin-skinned deformation in the pro-wedge is concentrated in the footwall of the active basement thrusts. The keystone structure forming the retro-wedge is progressively transported along the inverted normal fault bounding the overriding plate, with minor thin-skinned deformation in the footwall of the basement fault above the shallow décollement. During the final phase, the keystone structure and adjacent thick-skinned basement thrusts are transported onto the overriding plate, bending it down towards the subduction zone. At this stage, slightly later than in the reference model, a new thick-skinned thrust forms in the previously undeformed basement of the overriding plate (Figure 4f). The displacement along the individual basement thrusts in the retro-wedge is notably less than in the pro-wedge.

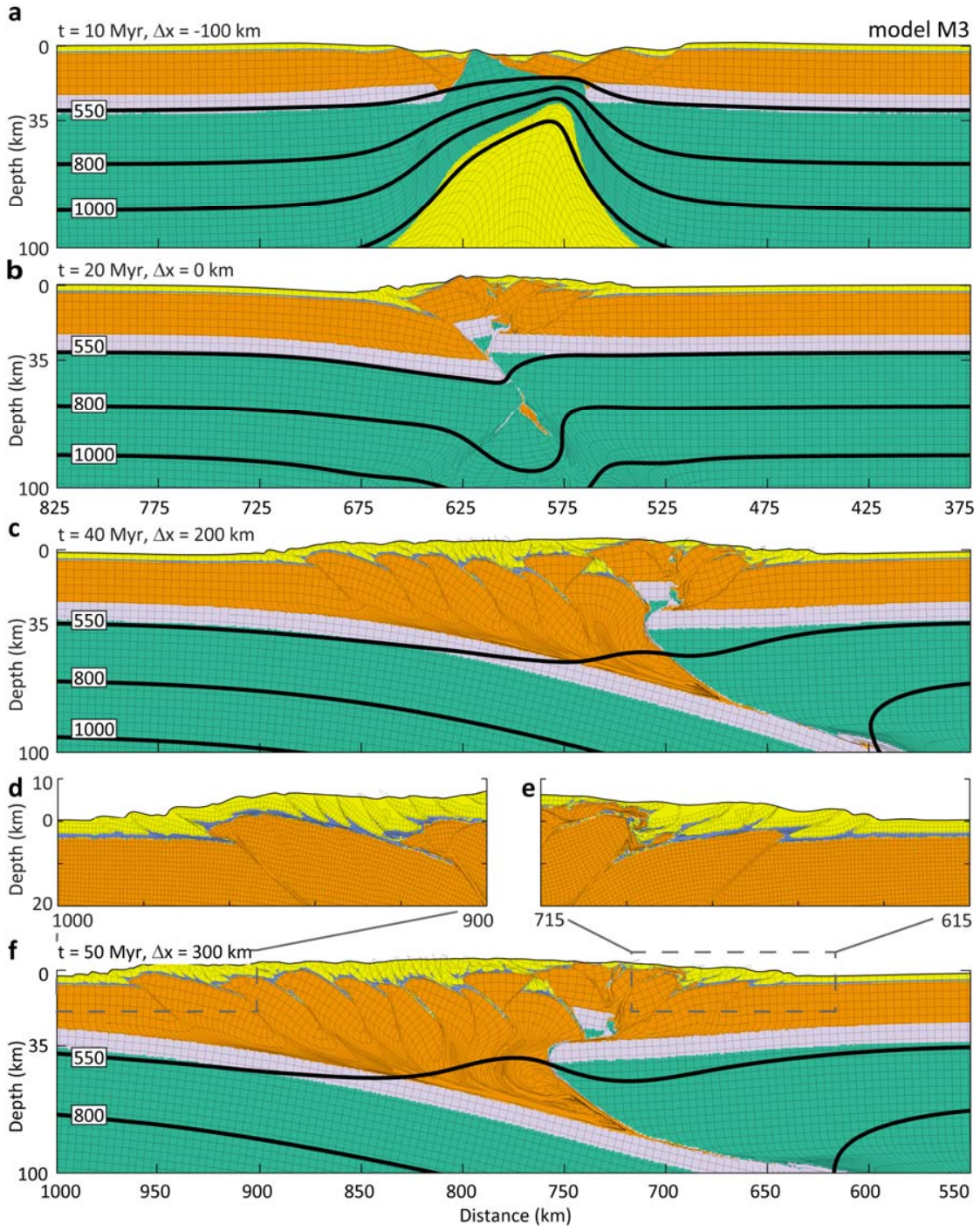

Figure 4. Model M3 undergoes extension until full crustal breakup before activating the inversion mode. Sedimentation and erosion are not accounted for. Presenting the same model properties as in the reference model (Figure 2) after **(a)** 10 Myr (Δx = -100 km) extension **(b)** 20 Myr (Δx = 0 km) after full inversion **(c)** 40 Myr (Δx = 200 km) contraction and **(f) 5**0 Myr (Δx = 300 km) contraction respectively. **(d)** and **(e)** are zoomed extracts from **(f)** to show the small-scale deformation patterns in the foreland fold-and-thrust belts.

3.3 The effect of sedimentation: model M4

Model M4 has a similar rheology to the reference model, with decoupling in the middle crust, a scaling factor f_{uc}=1 for the upper crust and f_{lc}=100 for the lower crust (Figure 5). Sedimentation is included, while erosion is not accounted for in this model. Starting from 20 Myr (i.e. 10 Myr and 100 km convergence after full inversion, where full inversion refers to the stage when the amount of initial extension is equaled by the subsequent contraction) all topography below a fixed reference height, representing base level, is filled with sediments.

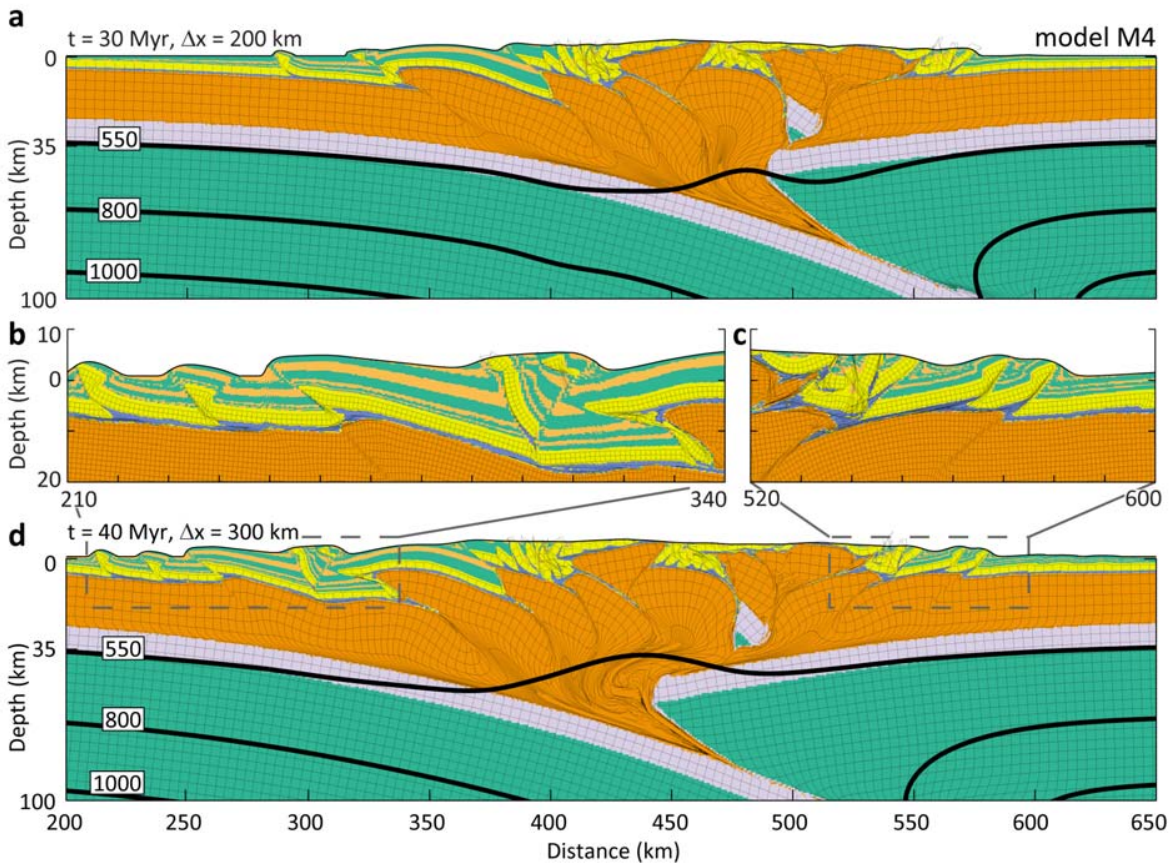

Figure 5. Model M4 including a simple sedimentation model. Starting at 100 km crustal shortening beyond full inversion, all topography below a reference level is filled with sediments at the end of every time step. Presenting the same model properties as in the reference model (Figure 2) after **(a)** 30 Myr (Δx = 200 km) contraction and **(d)** 40 Myr (Δx = 300 km) contraction. **(b)** and **(c)** are zoomed extracts from Figure 5f showing the small-scale deformation patterns in the foreland fold-and-thrust belts.

The experiment can be divided into four different phases, similar to the reference model. As sedimentation is only initiated after full inversion, the first two phases are identical to those of the reference model, with formation of a symmetric rift basin during extension and subsequent inversion resulting in the uplift of a mildly asymmetric keystone structure. The main characteristics of the third phase are similar to the reference model, with an outward propagating basement-thrust sequence building up the pro-wedge. However, both the thin-skinned and thick-skinned thrust sheets forming after the onset of sedimentation are significantly longer than those in the reference model (Figure 5a-c). Upon the onset of deposition, a wide and deep foreland basin forms in the footwall of the active basement thrust sheet. In comparison with the reference model without sedimentation, this basement thrust remains active for a longer time and accommodates more displacement, while the subsequent basement thrust forms further out below the foreland. During the final phase, the initial keystone structure migrates slightly further into the overriding plate compared to the reference model and the basement thrusts forming in the retro-wedge accommodate more displacement, resulting in a more strongly developed retro-wedge and an overall wider orogen (Figure 5d).

3.4 Effect of erosion: models M5 and M6

Models M5 (Figure 6) and M6 (Figure 7) have the same basic setup as model M4 but include elevation-dependent erosion in addition to deposition. Erosion is active from the model start but it has negligible effect in the extensional and inversion phases, as high-elevation topography is only present after uplift of the keystone structure. This means that the initial extension and the early inversion phases are practically identical to those of the reference model.

3.4.1 Moderate erosion rate: model M5

When applying a moderate erosion rate combined with deposition (model M5; Figure 6), a wide domain of basement thrust sheets forming in the third phase becomes exposed in the internal part of the orogen. At the same time, the foreland basins are shallower than the ones observed in model M4, resulting in the deposition of thinner sedimentary successions (Figure 6a).

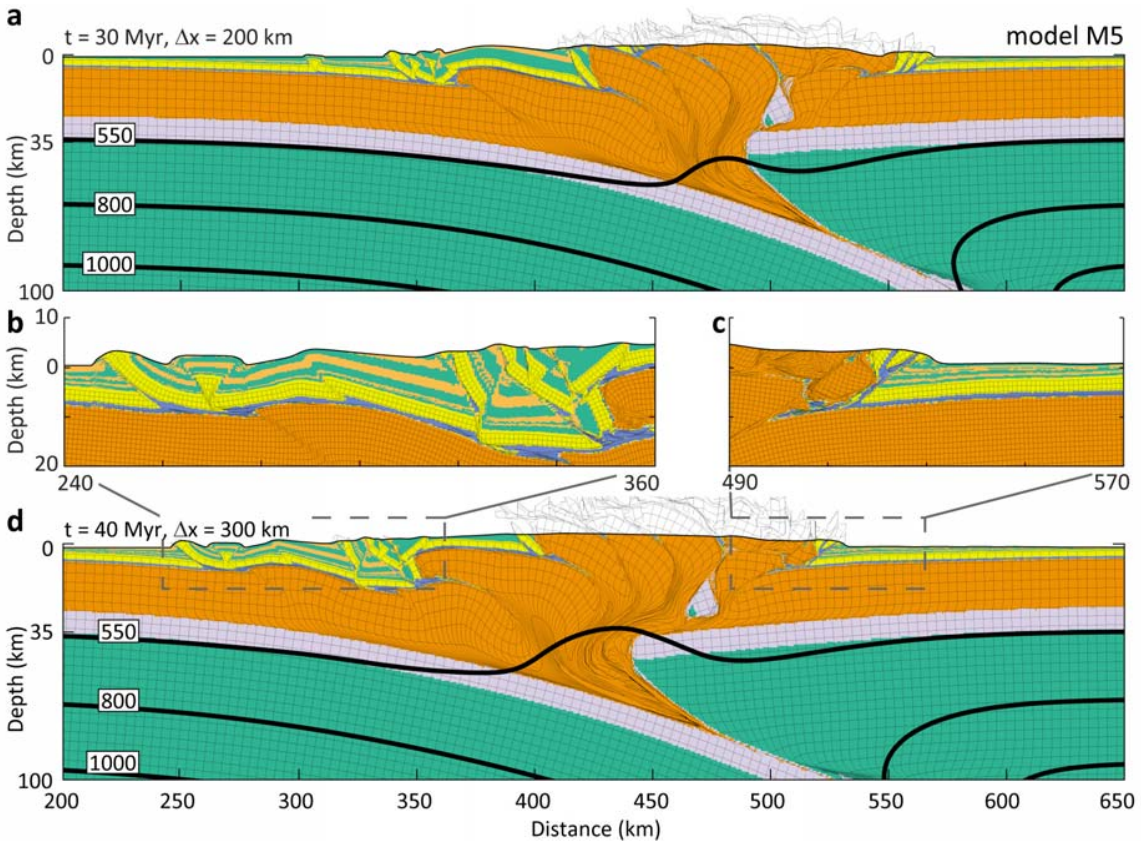

Figure 6. Model M5 including simple sedimentation and erosion models. Sedimentation is accounted for with the same algorithm as in model M2. Erosion is modeled using a simple elevation-dependent algorithm We have scaled the erosion rate so that a 4 km high topography would erode 1 km in 2 Myr. Presenting the same model properties as in the reference model (Figure 2) after **(a)** 30 Myr (Δx = 200 km) contraction and **(d)** 40 Myr (Δx = 300 km) contraction. **(b)** and **(c)** are zoomed extracts from Figure 6f showing the small-scale deformation patterns in the foreland fold-and-thrust belts.

Both the thick-skinned and thin-skinned thrust sheets developing in this model are marginally shorter than in model M4, but still significantly longer than in the reference model. The main effect of erosion is that the developing orogen is narrower (see also Figure 9). The initial keystone structure migrates more rapidly into the overriding plate and thick-skinned basement deformation in the retro-wedge starts 3 Myr earlier than in the reference model. Despite a significant amount of erosion of the retro-wedge, the lower-crustal root of the initial keystone structure is brought only slightly closer to the surface (Figure 6d) in comparison to the previous models.

3.4.2 High erosion rate: model M6

In case of more efficient erosion (model M6), the surface exposure of basement structures is more extensive, and the orogen is narrower than in model M5 with moderate erosion (Figure 7 and 9). The initial keystone structure is almost completely removed by erosion and, as a result, the retro-wedge is extremely narrow with all displacement focused along the inverted normal fault. The lower-crustal root of the keystone structure has been translated up the inverted normal fault ramp, thrusted over the weak décollement layer and exposed at the surface sliced in between two basement units at a very external position. The load of the retro-wedge is significantly less than in the previous models, resulting in a shallow retro-foreland basin with little thin-skinned deformation. Moreover, there is no basement deformation penetrating the overriding plate, resulting in the absence of the fourth phase described in the previous models.

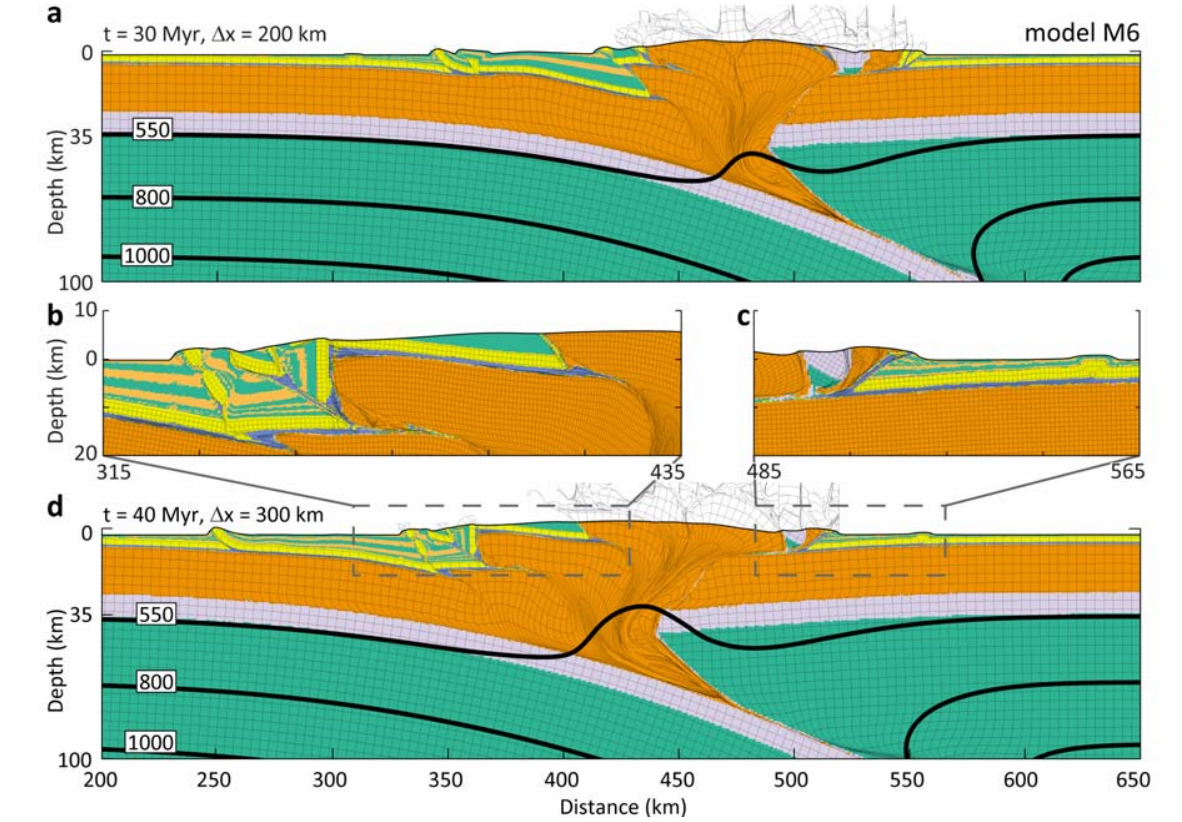

Figure 7. Model M6 allowing for simple sedimentation and erosion processes. Sedimentation erosion is accounted for using the same algorithms as in model M5, but we have scaled the erosion rate so that in this model a 4 km high topography would erode 1 km in 1 Myr. Presenting the same model properties as in the reference model (Figure 2) after **(a)** 30 Myr (Δx = 200 km) contraction and **(d)** 40 Myr (Δx = 300 km) contraction. **(b)** and **(c)** are zoomed extracts from Figure 7f showing the small-scale deformation patterns in the foreland fold-and-thrust belts.

3.5 Sensitivity to upper crustal strength: model M7

In model M7, we test the effect of a weaker upper crust, resulting in more efficient decoupling between the upper and lower crust, on the topographic and structural evolution by using an upper crustal viscosity scaling factor f_{uc}=0.2. Sedimentation and erosion are not included in this model experiment in order to isolate the effect of upper-crustal viscous strength.

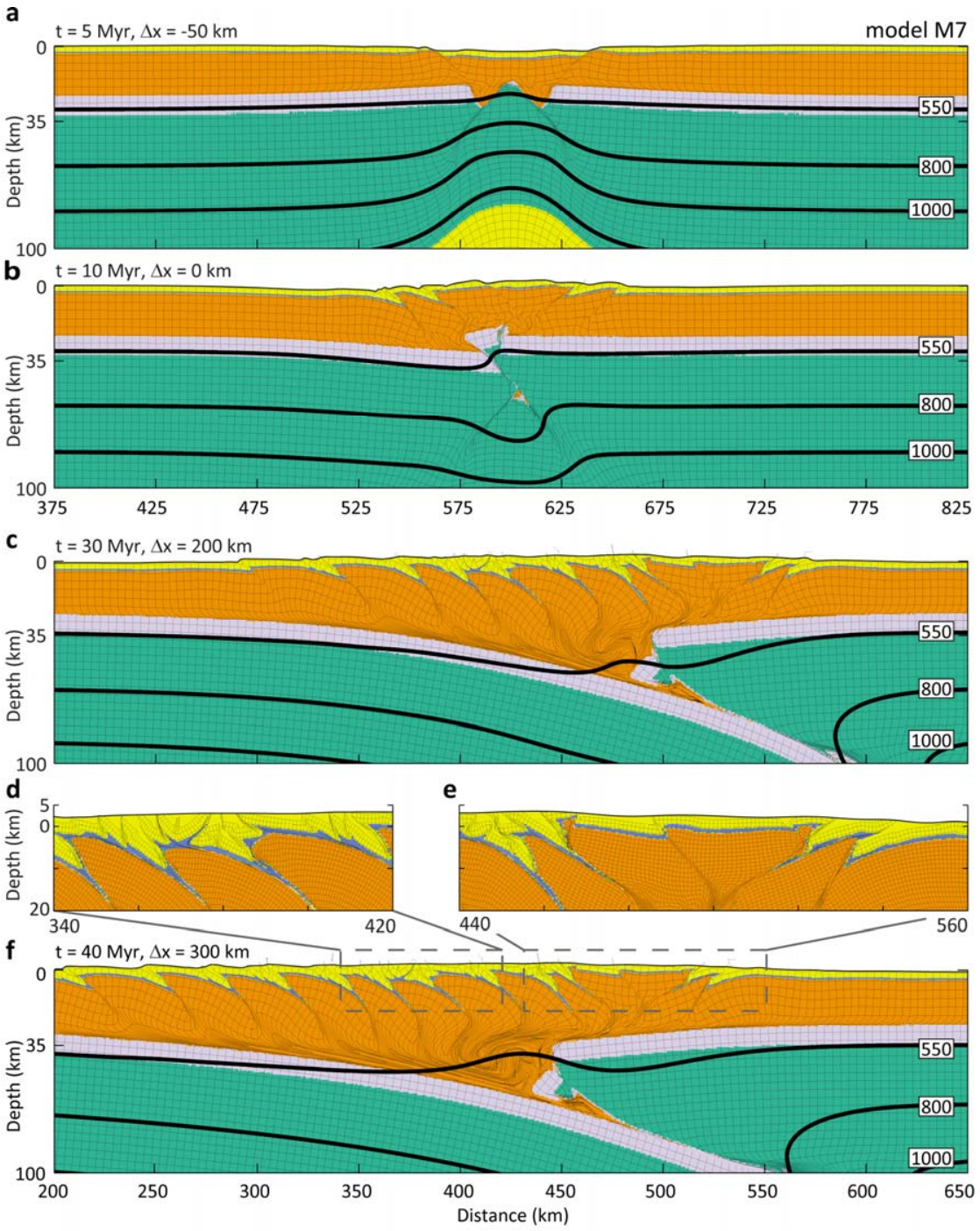

Figure 8. Model M7 has an upper-crustal viscous-strength scaling factor f_{uc}=0.2 to test the effect of less efficient coupling between the upper and the lower crust. Sedimentation and erosion are not accounted for. Presenting the same model properties as in the reference model (Figure 2) after **(a)** 5 Myr (Δx = -50 km) extension **(b)** 10 Myr (Δx = 0 km) full inversion **(c)** 30 Myr (Δx = 200 km) contraction and **(f)** 40 Myr (Δx = 300 km) respectively. **(d)** and **(e)** are zoomed extracts from **(f)** to show the small-scale deformation patterns.

As a result of the weaker coupling, the rifted basin developed in the extensional mode is about 60 % wider and 40 % shallower in comparison with Models 1 to 6, while the underlying mantle lithosphere experiences significantly more thinning than in the reference model (Figure 8a; compare to Figure 2a). Subsequently, inversion results in the development of a much broader keystone structure with a notably lower, plateau-like topographic high and very little thin-skinned thrust-activity (Figure 8b).

In the third phase, basement deformation is concentrated almost exclusively in the subducting plate (Figure 8c). A wide and low-elevation pro-wedge (see also Figure 9) is created by an outward propagating sequence of basement thrust sheets, while thin-skinned thrust development is minor throughout the model experiment. Unlike the previous models, in which the up-thrusted initial keystone structure remained attached to its lower-crustal root, this root is detached from the base of the upper crust shortly after full inversion and wedges in the subduction zone in model M7 (Figure 8c). As contraction continues, the rootless keystone structure is thrusted onto the lower crust of the overriding plate (Figure 8f). Despite this, the overriding plate displays no additional basement thrusting. Overall, the deformation is accommodated in a more distributed manner than in the previous experiments.

4 Discussion

4.1 The effects of extensional inheritance

The main observed difference between the contractional model M2 and the models incorporating explicitly modeled extensional inheritance is provided by the development and structure of the initial keystone structure and the retro-wedge. In the contractional model, the

keystone structure constitutes the bulk of the small, undeveloped retro-wedge throughout the entire model evolution. It has no internal structure and it is more or less stationary at the tip of the overriding plate, with the retro-shear zone accommodating very little displacement after the initiation of subduction. The overriding plate remains largely undeformed at all times, with only minor thin-skinned deformation connected to the retro-shear zone (Figure 3). In contrast to the pure contractional case, models including extensional inheritance show pronounced retro-wedge deformation. After initial inversion and buildup of the orogenic wedge, deformation propagates into the overriding plate. The keystone structure that develops during the inversion of models with extensional inheritance (accordion models) is significantly larger and involves a significant lower-crustal and mantle-lithospheric root. The main factors that control the degree of retro-wedge deformation are: 1) the pre-existence of strain-weakened frictional plastic shear zones that allow reactivation and easier transport of the keystone structure onto the overriding plate, and 2) the loading of the retro-wedge mantle lithosphere by the inverted keystone structure, providing access for thickened pro-wedge crust to be translated to the retro-side of the orogen. Thermal relaxation of the growing and thickening crustal-scale orogenic wedge enhances decoupling between the subducting lower crust and the upper crust, thereby further facilitating thrusting of pro-wedge crust onto the retro-wedge. Following initial translation of the keystone structure onto the retro-wedge, further shortening of the retro-wedge crust allows for the development of new thick-skinned thrust sheets in the previously undeformed basement of the overriding plate (Figure 2f) and the formation of a thin-skinned thrust belt on top. Model M3, which extends until full crustal break-up before inversion, exhibits a more complex keystone structure as it includes several inverted normal

faults (Figure 4). However, this does not affect the overall model evolution significantly. Translation of the keystone structure onto the overriding plate is slower, hence the first basement thrust sheets in the overriding plate form 5 Myr (and 50 km convergence) later, but the general structure is very similar to that of the reference model (compare Figure 2f and Figure 4f). We therefore conclude that the amount of extension experienced by the crust beyond the break-up of the rigid lower crust does not strongly affect the overall deformation style.

4.2 The effects of synorogenic sedimentation

The effects of sedimentation on the evolution of an inverted rift basin can be best understood by comparing the reference model M1 (Figure 2) and model M4 (Figure 5). Syn-tectonic sedimentation leads to the development of a wide and deep sedimentary fold-and-thrust belt in the foreland depression in front of the pro-wedge. As a result of sediment loading, the active frontal basement thrust remains active for a longer time and accommodates more displacement, while the subsequent new basement thrust forms further out below the foreland. In the presence of extensional inheritance (model M4; Figure 5) the additional mass of the initial keystone structure loading the overriding plate is sufficient to create a deep foreland depression that can accommodate a significant amount of synorogenic sediments. Sedimentation also significantly affects thin-skinned deformation on both sides of the orogen, creating complex sets of long thrust sheets and pop-up structures, with generally more displacement along the base of the individual units than observed in the reference model (Figure 5b and c).

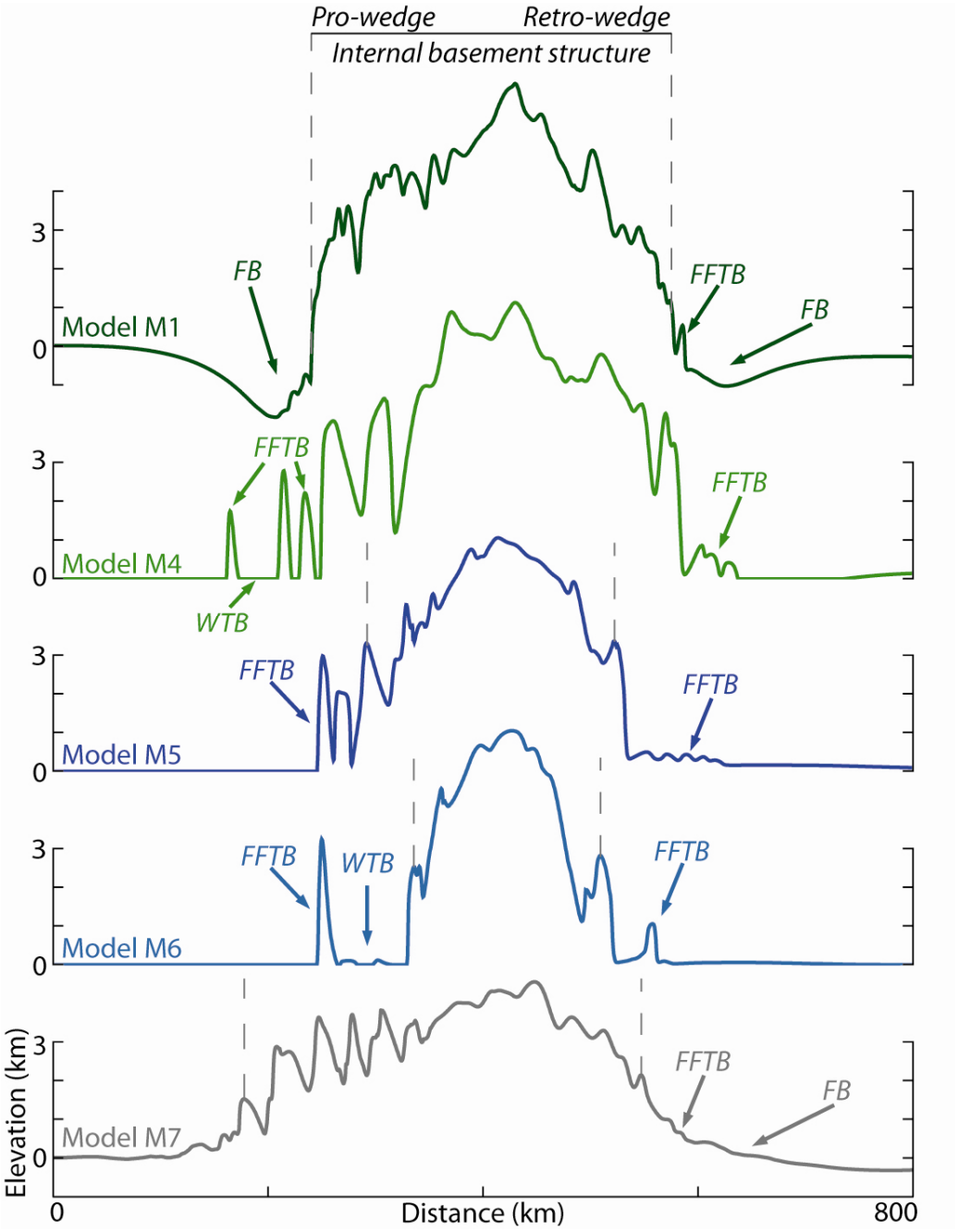

Figure 9. Topographic profiles for **(a)** model M1 **(b)** model M2 **(c)** model M3 **(d)** model M4 and **(e)** model M9 after 40 Myr (Δx = 300 km). Key: FB: foreland basin; FFTB: foreland fold-and-thrust belt; WTB: wedge-top basin. The vertical dashed lines indicate the surface traces of the most external basement thrust sheets.

As concerns the thin-skinned deformation of sedimentary fold-and-thrust belts, our model results are in good agreement with recent modeling results of Fillon et al. (2012), who demonstrated a strong correlation between thin-skinned thrust-sheet length and the thickness of synorogenic sediments loading the foreland fold-and-thrust belt.

In an accompanying paper that focuses on the role of sedimentation in contractional orogens (Erdős et al., subm.), we propose that the effects of syntectonic sedimentation on thrust-sheet development can be understood by considering minimum-work principles (Hardy et al., 1998; Masek and Duncan, 1998). We predict that a new thrust will occur where the total combined work of the gravitational, frictional, and viscous forces required for slipping on the viscous basal décollement and breaking through to the surface is minimized. Thrusting along the active shear zone builds topography, which in turn increases the gravitational work. A new thrust sheet is formed when the total work needed to continue slipping along the active shear zone exceeds the work needed to create a new thrust that slides along the viscous basal décollement and breaks through to the surface. Our models presented here and in Erdős et al. (subm.) demonstrate that these principles apply for both thin-skinned and thick-skinned deformation. For a comprehensive description of the applications of minimum-work principles in the presence of significant synorogenic sedimentation we refer to Erdős et al. (subm.).

4.3 The effects of erosion

The effects of erosion on orogenic evolution in the presence of extensional inheritance can be best understood by comparing models M4, M5, and M6 (Figures 5, 6 and 7). Erosion facilitates the localization of deformation by reducing the load (and therefore the gravitational stresses) in the core of the orogenic wedge, thus leading to a decrease in wedge width (e.g., Willett, 1999).

Moreover, simple mass budget considerations also require that the wedge width decreases with increasing erosion rate, all else remaining equal (Dahlen, 1990; Whipple and Meade, 2004). In the model with a moderate erosion rate (model M5), basement is extensively exposed in the central part of the orogen. As the internal mass of the orogen is reduced by erosion, orogenic loading becomes less effective in creating foreland depressions. As a result, the foreland fold-and-thrust belts are thinner and less developed than the ones observed in model M4 that does not include erosion (Figure 5). Reduced synorogenic loading in turn limits the effect of sedimentation on basement structure. Even with moderate amounts of deposition, the elongation of both the thick-skinned and the thin-skinned thrust sheets is still apparent. Higher erosion rates enhance localization of deformation into a very narrow orogenic wedge, preventing the migration of deformation into the undeformed basement of the overriding plate and resulting in a less developed retro-wedge (e.g., model M6; Figure 7).

4.4 Interaction of thin-skinned and thick-skinned tectonics

The pre-tectonic sediments, including a weak basal décollement horizon, allow for investigating the interaction between thin-skinned and thick-skinned tectonic styles. Both the accordion and the pure contractional models show that the thin-skinned thrust sheets are generally rooted in the footwall of new basement thrusts that are formed in an outward-propagating sequence (e.g., model M1; Figure 2d and e).

Following the formation of a new basement thrust, the earlier, more proximal thin-skinned deformation is abandoned and a new thin-skinned thrust is activated in front of the basement thrust sheet. In contrast, thin-skinned thrusts forming ahead of basement deformation in the foreland do not affect the position of a new basement thrust below the foreland. Thus, it is the

thick-skinned basement deformation that drives thin-skinned deformation in the sedimentary cover, the coupling in the opposite sense being significantly less efficient. Without the presence of syntectonic sedimentation (e.g., model M1; Figure 2d and e) the in an individual thin-skinned thrust sheets have very similar length-scale and their regular activation “accretion cycle” (e.g., Hoth et al., 2007) can be understood from minimum-work principles (Hardy et al., 1998; Masek and Duncan, 1998). When syntectonic sedimentation is included (e.g., model M4; Figure 5b and c), the thin-skinned thrust sheets forming in the foreland fold-and-thrust belts become significantly longer. Basement deformation and sediment loading interact in forcing both the thin- and thick-skinned fold-and-thrust belt structure. While sediment loading results in longer thin- and thick-skinned thrust sheets, basement deformation triggers thin-skinned thrust formation where the basement shear zones reach the basal décollement. As a result, the thin-skinned thrust sheets observed in the models with syntectonic sedimentation display different length scales. The introduction of erosion in the models does not affect the general behavior of the thin-skinned fold-and-thrust belts forming in the forelands, as most erosion takes place in the internal parts of the orogen. Both the pre- and synorogenic sediments are gradually eroded from these models, leaving a growing area of basement rocks exposed in the orogenic core.

4.5 The effect of upper crustal strength

The level of coupling between the strong lower crust and the weaker upper crust is a key parameter in the structural evolution of the orogen. When the upper crust is weak (model M7; Figure 8), the viscous middle crustal décollement is thicker and allows for more distributed deformation during both extension and contraction (Figure 8a and 8c). The reduction in thickness of the frictional-plastic upper crust results in the development of shorter basement

thrust sheets with less displacement accommodated along each thrust. Moreover, the weak upper crust is unable to support high topography, contributing to a wide, plateau-like orogen (see also Figure 9).

5 Comparison with natural systems

The lithosphere-scale thermo-mechanical models presented here demonstrate the fundamental influence of lithospheric strength, extensional inheritance and surface processes on the structural evolution of mountain belts. In the following sections we will summarize the first-order structure of three orogens formed by inversion of a prior rift or rifted passive margin displaying different deformation styles: the High Atlas, the Pyrenees, and the Central Alps. We will compare these observations to our results in order to assess how we could explain the observed differences in the framework of our models.

5.1 The High Atlas

The Moroccan High Atlas Mountains provide a good example of an intracontinental mountain belts (Rodgers, 1987; Ziegler et al., 1995) and formed during Cenozoic times within the interior of the African plate, due to compression linked to convergence between Africa and Europe (Teixell et al*.,* 2003). The chain developed from the inversion of Jurassic rift and transtensional basins and is made up of Mesozoic sediments deposited in these basins, with minor pre-Mesozoic and Cenozoic occurrences (Arboleya et al., 2004 and references therein). Pre-Mesozoic Hercynian basement rocks are only exposed at the surface in eroded antiforms. The High Atlas, similar to other intracontinental mountain belts, experienced moderate crustal shortening, yet it has very high topography, with peaks over 4000 m (Teixell et al., 2003). The

anomalous topography is commonly ascribed to post-contractional removal of mantle lithosphere underneath the belt (e.g., Missenard et al., 2006). In the central part of the orogen, most of the Alpine deformation is accommodated in a 100 km wide belt (Figure 10c after Arboleya et al. (2004) and Ayarza et al. (2005)). Deformation is mostly restricted to the upper crust, while the approximately 13-15 km thick lower crust subducts with the mantle lithosphere (Ayarza et al., 2005; Wigger et al., 1992). The estimated total shortening along this section is in the order of 30 km (Teixell et al., 2003).

Most of the contractional deformation is accommodated along the North and South High Atlas fronts, with minor thin-skinned folding in the forelands and a number of crustal-scale inverted extensional structures present in between (Figure 10a). These characteristics are to first order consistent with the early inversion stage of Model 1 (Figure 2b). The North and South High Atlas fronds can be seen as analogues for the shear zones on either side of the keystone structure in our accordion models, with no major inverted normal faults observed at more distal positions from the orogen.

5.2 The Pyrenees

The Pyrenees (Figure 10b) are a collisional orogen formed between the Late Cretaceous (90 Ma) and Early Miocene (20 Ma) as a result of convergence between the Iberian and European plates (Roest and Srivastava, 1991; Rosenbaum et al., 2002; Vissers and Meijer, 2012). The range is dominated by inversion tectonics (Muñoz et al., 1986), owing to thrusting along inherited extensional structures that were originally formed during Triassic to Cretaceous rifting and transtension, associated with anticlockwise rotation of the Iberian plate with respect to Europe (Roest and Srivastava, 1991; Rosenbaum et al., 2002). Here we focus on the Central Pyrenean

ECORS seismic section (ECORS Team, 1988) and the associated balanced section restoration (Muñoz, 1992).

Underthrusting of the Iberian crust below the European crust results in an asymmetric wedge, featuring a wide southern pro-wedge and a narrower northern retro-wedge. In the centre of the belt, the Axial Zone comprises a south-vergent antiformal stack of upper crustal thrust sheets (Muñoz, 1992). The Axial Zone is flanked towards the south by the South Pyrenean Unit, a fold-and-thrust belt consisting of Mesozoic and Cenozoic sedimentary rocks. North of the Axial Zone, in the North Pyrenean Unit, basement and cover rocks form steep, north-vergent thrust sheets and pop-up structures (Capote et al., 2002; Muñoz, 1992).

The presence of a dense, presumably lower-crustal, body preserved at shallow depth below the North Pyrenean Unit as inferred from gravity data (Torne et al., 1989), together with the inverted extensional structures of the retro-wedge, are features that can only be observed in and explained by our accordion models and are a direct result of extensional inheritance. Moreover, the active imbrication of thick-skinned thrust sheets with a wide thin-skinned foreland fold-and-thrust belt in the pro-wedge, coupled with the relatively slow retro-wedge deformation and shallower retro-foreland basin, can all be observed at an intermediate stage of model M1 (Figure 2c), while the widespread exposure of basement structures in the axial zone is well reproduced by model M5 (Figure 6a). The estimated 160 km of shortening (Beaumont et al., 2000) is also consistent with the modeled amount of contraction at these intermediate model stages.

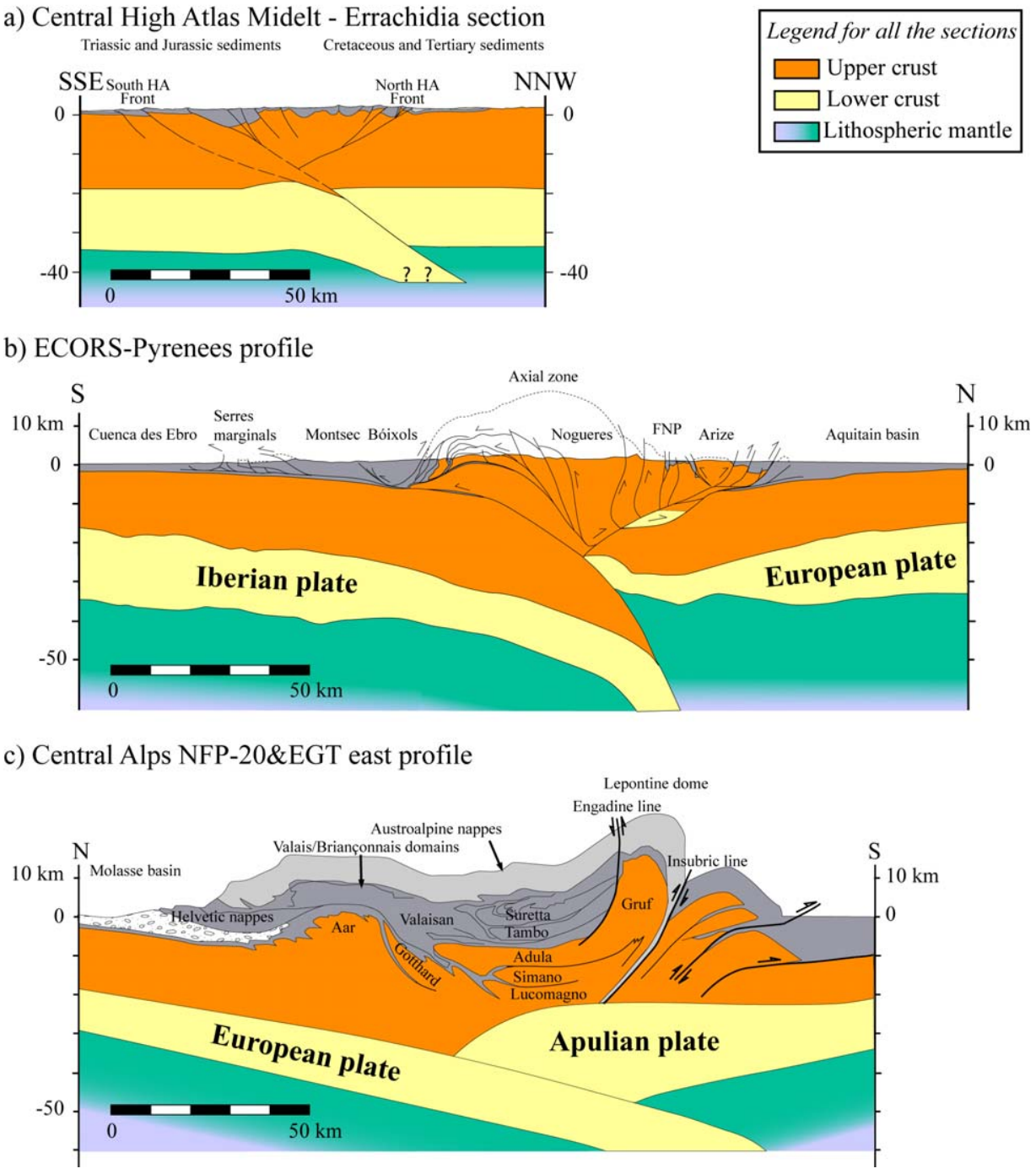

Figure 10. Natural examples. Crustal-scale cross sections from **(a)** the European Central Alps after *Schmid and Kissling* (2000) **(b)** the Central Pyrenees after *Muñoz* (1992) and *Beaumont et al.* (2000) **(c)** the Central High Atlas redrawn after *Arboleya et al.* (2004) and *Ayarza et al.* (2005)

5.3 The Central Alps

The European Alps record the closure of the Tethys ocean basins during convergence of the African and European plates (Stampfli et al., 2001). The crustal structure is well constrained by several crustal-scale deep seismic transects crossing the Alps. Although these sections show significant along strike variation, some first-order crustal-scale features are observed in all of them. These common features are: (1) east-south-east to south directed subduction of the European lithosphere; (2) a gap between the European and Adriatic (or Apulian) Moho and (3) strong decoupling between upper and lower crust, the lower subducting crust along with the mantle lithosphere while the upper crust builds up the orogen (Schmid et al., 2004; Schmid and Kissling, 2000; Schmid et al., 1996). Here we focus on the profile crossing the Central Alps, NFP-20 EAST&EGT (Figure 10c; after Schmid and Kissling (2000)).

The most dominant features of the internal part of this section are the Lepontine dome and the stacking of the sub-Penninic crustal-scale thrusts under the Penninic nappes (Figure 10c). This complex structure is reproduced to first order in our model M5 (Figure 6d), along with the inverted Insubric back-thrust and to a lesser extent the Austroalpine nappes. The 300 km of shortening estimated for this section after the subduction of the Briançonnais and Valais domains is consistent with the amount of contraction at this stage of model development. The complexities introduced by the extensional inheritance and the strike slip deformation accommodated along the Insubric line can explain the existence of lithospheric mantle fragments at shallow depths.

We have in this paper focused on the combined effects of extensional inheritance and surface processes. Numerical models including deposition show a significant effect on both thin-

skinned and thick-skinned deformation with sedimentation leading to an increase in thrust length. We note here that this may explain long thin-skinned thrusts and basement thrusting as observed in the Alpine foreland fold and thrust belt. This relationship between syn-tectonic deposition and orogenic foreland deformation is more fully developed in an accompanying paper (Erdos et al., subm.).

6 Conclusions

In this study we have used thermo-mechanical model experiments to explore the effects of surface processes and extensional inheritance on the structural evolution of contractional orogens and their foreland basins. We draw the following conclusions:

1. Extensional inheritance plays a fundamental role, facilitating the migration of deformation into the undeformed basement of the overriding plate. Moreover, a significant amount of lower-crustal/ lithospheric mantle material is preserved at shallow depths in the presence of extensional inheritance but high erosion rates are needed to bring this material to the surface.

2. The amount of extension experienced by the crust beyond break-up of the rigid lower crust does not affect the overall deformation style strongly. The initial keystone structure becomes somewhat larger and more complex when extension is allowed to run to full crustal break-up, but the general features remain largely unaffected.

3. Sedimentation results in longer basement thrust sheets as well as longer thin-skinned thrust sheets and a generally wider orogenic belt. The active frontal basement thrust remains active for a longer time, accommodating more displacement, while subsequent basement thrusts form further out below the foreland, creating longer thrust sheets. In the presence of inherited

extensional structures this is also true in the retro-wedge, even though the thrust sheets developing there are consistently shorter than those developing in the pro-wedge.

4. Erosion removes material from the internal part of the orogen, narrowing the wedge and reducing the orogenic load on the colliding plates, hence limiting the space available for deposition in the flexural foredeeps and thereby limiting the effects of sedimentation on foreland structures described above. High erosion rates also enhance localization of deformation into a narrow orogenic wedge, preventing its migration into the undeformed basement of the overriding plate.

5. In the presence of pre- and/or synorogenic sediments, thin-skinned fold-and-thrust belts form above the basement thrust sheets. The thin-skinned thrust sheets are generally rooted in the footwall of the basement thrusts as they form in an outward-propagating sequence. Following the formation of a new basement thrust, the earlier, more proximal thin-skinned deformation sequence is abandoned in favor of a new thin-skinned thrust forming in front of the new basement thrust sheet. In contrast, the thin-skinned thrusts forming ahead of the basement deformation structures in the foreland do not affect the position of a new basement thrust.

6. When the middle and upper crust are moderately strong they can support high topography. A weaker upper crust, resulting in a low-viscosity decoupling horizon zone at shallower crustal depths, leads to more distributed crustal shortening, with a wider plateau-like topography supported by a long sequence of moderately long basement thrust-sheets, and low intensity thin-skinned thrust development on top of it.

7. The crustal structure at different stages of the accordion models presented in this study show good first-order correlation with structural features observed in the High Atlas, the Central Pyrenees and the Central Alps. With increasing amounts of convergence (e.g. from High Atlas to Central Alps) the inverted keystone structure migrates further onto the overriding plate, and both the pro- and retro-wedges become wider and more developed.

8. At the early stages of inversion (e.g., High Atlas) the main mass of the orogen is provided by a keystone structure uplifted along two inverted normal faults, while the amount of inverted structures within this block is controlled by the amount of extension previously experienced by the region.

9. The presence of a lower-crustal/lithospheric mantle body thrusted onto the overriding plate and preserved at shallow depth, together with the relatively slow deformation of the retro-wedge involving inverted extensional structures, as observed in the Central Pyrenees, can be explained by the presence of inherited extensional structures.

10. The wide retro-wedge and the basement deformation in the overriding plate observed in the Central Alps are features that are only present in the later stages of our accordion models and result from the thermal relaxation of the growing and thickening orogenic wedge.

Acknowledgements

This study is supported by the Norwegian Research Council that funded the Norwegian component of the European Science Foundation Eurocore TOPO-Europe project PyrTec. The Bergen Center of Computational Science is acknowledged for access to computational

infrastructure. We thank Cedric Thieulot for his help during the early stages of designing and setting up the model experiments.

References

Arboleya, M. L., A. Teixell, M. Charroud, and M. Julivert (2004), A structural transect through the High and Middle Atlas of Morocco, Journal of African Earth Sciences, 39(3-5), 319-327, doi:10.1016/j.jafrearsci.2004.07.036.

Ayarza, P., F. Alvarez-Lobato, A. Teixell, M. L. Arboleya, E. Teson, M. Julivert, and M. Charroud (2005), Crustal structure under the central High Atlas Mountains (Morocco) from geological and gravity data, Tectonophysics, 400(1-4), 67-84, doi: 10.1016/j.tecto.2005.02.009.

Bassi, G., C. E. Keen, and P. Potter (1993), Contrasting styles of rifting: Models and examples form the Eastern Canadian Margin, Tectonics, 12, 639-655.

Beaumont, C., P. Fullsack, and J. Hamilton (1992), Erosional control of active compressional orogens, in Thrust Tectonics, edited by K. R. McClay, pp. 1-18, Chapman & Hall, London.

Beaumont, C., P. Fullsack, and J. Hamilton (1994), Styles of Crustal Deformation in Compressional Orogens Caused by Subduction of the Underlying Lithosphere, Tectonophysics, 232(1-4), 119-132, doi: 10.1016/0040-1951(94)90079-5.

Beaumont, C., J. A. Muñoz, J. Hamilton, and P. Fullsack (2000), Factors controlling the Alpine evolution of the central Pyrenees inferred from a comparison of observations and geodynamical models, Journal of Geophysical Research, 105(B4), 8121-8145, doi: 10.1029/1999jb900390.

Bonnet, C., J. Malavieille, and J. Mosar (2007), Interactions between tectonics, erosion, and sedimentation during the recent evolution of the Alpine orogen: Analogue modeling insights, Tectonics, 26(6), doi:10.1029/2006tc002048.

Bos, B., and C. J. Spiers (2002), Frictional-viscous flow of phyllosilicate-bearing fault rock: Microphysical model and implications for crustal strength profiles, Journal of Geophysical Research, 107(B2), 2028, doi 10.1029/2001jb000301.

Buck, W. R. (1991), Modes of Continental Lithospheric Extension, Journal of Geophysical Research, 96(B12), 20161-20178, doi: 10.1029/91jb01485.

Buck, W. R., L. L. Lavier, and A. Poliakov (1999), How to make a rift wide, Philosophical Transactions of the Royal Society A: Mathematical, Physical and Engineering Sciences, 357(1753), 671-693, doi:10.1098/rsta.1999.0348.

Buiter, S. J. H. (2012), A review of brittle compressional wedge models, Tectonophysics, 530-531, 1-17, doi:10.1016/j.tecto.2011.12.018.

Capote, R., J. A. Muñoz, J. L. Simon, C. L. Liesa, and L. E. Arlegui (2002), Alpine tectonics I: the Alpine system north of the Betic Cordillera, in The Geology of Spain, edited by W. Gibbon and T. Moreno, pp. 367-400, The Geological Society, London.

Dahlen, F. A. (1990), Critical Taper Model of Fold-and-Thrust Belts and Accretionary Wedges, Annual Review of Earth and Planetary Sciences, 18, 55-99, doi: 10.1146/annurev.earth.18.1.55.

DeCelles, P. G., and K. A. Giles (1996), Foreland basin systems, Basin Research, 8(2), 105-123, doi: 10.1046/j.1365-2117.1996.01491.x.

Ellis, S., C. Beaumont, R. A. Jamieson, and G. Quinlan (1998), Continental collision including a weak zone: the vise model and its application to the Newfoundland Appalachians, Can J Earth Sci, 35(11), 1323-1346, doi: 10.1139/E97-100.

Fillon, C., R. S. Huismans, and P. van der Beek (2012), Syntectonic sedimentation effects on the growth of fold-and-thrust belts, Geology, 41(1), 83-86, doi:10.1130/g33531.1.

Ford, M. (2004), Depositional wedge tops: interaction between low basal friction external orogenic wedges and flexural foreland basins, Basin Research, 16(3), 361-375, doi:10.1111/j.1365-2117.2004.00236.x.

Gleason, G. C., and J. Tullis (1995), A Flow Law for Dislocation Creep of Quartz Aggregates Determined with the Molten-Salt Cell, Tectonophysics, 247(1-4), 1-23, doi: 10.1016/0040-1951(95)00011-B.

Hardy, S., C. Duncan, J. Masek, and D. Brown (1998), Minimum work, fault activity and the growth of critical wedges in fold and thrust belts, Basin Research, 10(3), 365-373, doi: 10.1046/j.1365-2117.1998.00073.x.

Hoth, S., A. Hoffmann-Rothe, and N. Kukowski (2007), Frontal accretion: An internal clock for bivergent wedge deformation and surface uplift, Journal of Geophysical Research, 112, B06408, doi:10.1029/2006JB004357.

Huismans, R. S., and C. Beaumont (2003), Symmetric and asymmetric lithospheric extension: Relative effects of frictional-plastic and viscous strain softening, Journal of Geophysical Research, 108(B10), 2496, doi 10.1029/2002jb002026.

Huismans, R. S., and C. Beaumont (2011), Depth-dependent extension, two-stage breakup and cratonic underplating at rifted margins, Nature, 473(7345), 74-78, doi:10.1038/nature09988.

Huismans, R. S., S. J. H. Buiter, and C. Beaumont (2005), Effect of plastic-viscous layering and strain softening on mode selection during lithospheric extension, Journal of Geophysical Research, 110(B2), B02406, doi 10.1029/2004jb003114.

Jamieson, R. A., and C. Beaumont (2013), On the origin of orogens, Geological Society of America Bulletin, 125(11-12), 1671-1702, doi: 10.1130/B30855.1.

Jammes, S., and R. S. Huismans (2012), Structural styles of mountain building: Controls of lithospheric rheologic stratification and extensional inheritance, Journal of Geophysical Research, 117(B10), doi:10.1029/2012jb009376.

Karato, S., and P. Wu (1993), Rheology of the upper mantle: a synthesis, Science, 260(5109), 771-778, doi:10.1126/science.260.5109.771.

Masek, J. G., and C. C. Duncan (1998), Minimum-work mountain building, J Geophys Res, 103(B1), 907, doi:10.1029/97jb03213.

Missenard, Y., H. Zeyen, D. Frizon de Lamotte, P. Leturmy, C. Petit, M. Sébrier, and O. Saddiqi (2006), Crustal versus asthenospheric origin of relief of the Atlas Mountains of Morocco, Journal of Geophysical Research, 111, B03401, doi: 10.1029/2005jb003708.

Mouthereau, F., J. Tensi, N. Bellahsen, O. Lacombe, T. De Boisgrollier, and S. Kargar (2007), Tertiary sequence of deformation in a thin-skinned/thick-skinned collision belt: The Zagros Folded Belt (Fars, Iran), Tectonics, 26(5), doi:10.1029/2007tc002098.

Mouthereau, F., A. B. Watts, and E. Burov (2013), Structure of orogenic belts controlled by lithosphere age, Nature Geoscience, 6(9), 785-789, doi:10.1038/ngeo1902.

Mugnier, J. L., P. Baby, B. Colletta, P. Vinour, P. Bale, and P. Leturmy (1997), Thrust geometry controlled by erosion and sedimentation: A view from analogue models, Geology, 25(5), 427-430, doi: 10.1130/0091-7613(1997)025<0427:Tgcbea>2.3.Co;2.

Muñoz, J. A. (1992), Evolution of a continental collision belt: ECORS Pyrenees crustal balanced cross section, in Thrust Tectonics, edited by K. R. McClay, pp. 235-246, Chapman & Hall, New York.

Rodgers, J. (1987), Chains of Basement Uplifts within Cratons Marginal to Orogenic Belts, American Journal of Science, 287(7), 661-692.

Roest, W. R., and S. P. Srivastava (1991), Kinematics of the Plate Boundaries between Eurasia, Iberia, and Africa in the North-Atlantic from the Late Cretaceous to the Present, Geology, 19(6), 613-616, doi: 10.1130/0091-7613(1991)019<0613:Kotpbb>2.3.Co;2.

Rosenbaum, G., G. S. Lister, and C. Duboz (2002), Relative motions of Africa, Iberia and Europe during Alpine orogeny, Tectonophysics, 359(1-2), 117-129, doi: 10.1016/S0040-1951(02)00442-0.

Schmid, S. M., B. Fugenschuh, E. Kissling, and R. Schuster (2004), Tectonic map and overall architecture of the Alpine orogen, Eclogae Geologicae Helvetiae, 97(1), 93-117, doi: 10.1007/s00015-004-1113-x.

Schmid, S. M., and E. Kissling (2000), The arc of the western Alps in the light of geophysical data on deep crustal structure, Tectonics, 19(1), 62-85, doi: 10.1029/1999tc900057.

Schmid, S. M., O. A. Pfiffner, N. Froitzheim, G. Schonborn, and E. Kissling (1996), Geophysical-geological transect and tectonic evolution of the Swiss-Italian Alps, Tectonics, 15(5), 1036-1064, doi: 10.1029/96tc00433.

Sibson, R. H. (1990), Conditions for fault-valve behaviour, Geol. Soc. Spec. Publ., 54, 15–28.

Stampfli, G., J. Mosar, P. Favre, A. Pillevuit, and J. C. Vannay (2001), Permo-Mesozoic evolution of the western Tethys realm: the Neo-Tethys East Mediterranean Basin connection, in Peri-Tethys Memoir 6: Peri-Tethyan Rift/Wrench Basins and Passive Margins, edited by P. A. Ziegler, pp. 51-108, Mém. Mus. Natn. Hist. Nat., Paris.

Stolar, D. B., S. D. Willett, and G. H. Roe (2006), Climatic and tectonic forcing of a critical orogen, Geological Society of America Special Paper, 398, 241-250, doi:10.1130/2006.2398(14).

Storti, F., and K. McClay (1995), Influence of Syntectonic Sedimentation on Thrust Wedges in Analog Models, Geology, 23(11), 999-1002, doi: 10.1130/0091-7613(1995)023<0999:Iossot>2.3.Co;2.

Streit, J. E. (1997), Low frictional strength of upper crustal faults: A model, Journal of Geophysical Research, 102(B11), 24619-24626, doi: 10.1029/97jb01509.

ECORS Pyrenees Team (1988), The ECORS deep reflection seismic survey across the Pyrenees, Nature, 331, 508–511.

Teixell, A., M.-L. Arboleya, M. Julivert, and M. Charroud (2003), Tectonic shortening and topography in the central High Atlas (Morocco), Tectonics, 22(5), doi:10.1029/2002tc001460.

Thieulot, C. (2011), FANTOM: Two- and three-dimensional numerical modelling of creeping flows for the solution of geological problems, Physics of the Earth and Planetary Interiors, 188(1-2), 47-68, doi:10.1016/j.pepi.2011.06.011.

Torne, M., B. Decabissole, R. Bayer, A. Casas, M. Daignieres, and A. Rivero (1989), Gravity Constraints on the Deep-Structure of the Pyrenean Belt Along the Ecors Profile, Tectonophysics, 165(1-4), 105-116, doi: 10.1016/0040-1951(89)90039-5.

Vissers, R. L. M., and P. T. Meijer (2012), Iberian plate kinematics and Alpine collision in the Pyrenees, Earth-Sci Rev, 114(1-2), 61-83, doi: 10.1016/j.earscirev.2012.05.001.

Whipple, K. X. (2009), The influence of climate on the tectonic evolution of mountain belts, Nature Geoscience, 2(2), 97-104, doi:10.1038/ngeo413.

Whipple, K. X., and B. J. Meade (2004), Controls on the strength of coupling among climate, erosion, and deformation in two-sided, frictional orogenic wedges at steady state, Journal of Geophysical Research, 109, F01011, doi: 10.1029/2003jf000019.

Wigger, P., G. Asch, P. Giese, W. D. Heinsohn, S. O. Elalami, and F. Ramdani (1992), Crustal Structure Along a Traverse across the Middle and High Atlas Mountains Derived from Seismic Refraction Studies, Geologische Rundschau, 81(1), 237-248, doi: 10.1007/Bf01764552.

Willett, S., C. Beaumont, and P. Fullsack (1993), Mechanical Model for the Tectonics of Doubly Vergent Compressional Orogens, Geology, 21(4), 371-374, doi: 10.1130/0091-7613(1993)021<0371:Mmftto>2.3.Co;2.

Willett, S. D. (1999), Orogeny and orography: The effects of erosion on the structure of mountain belts, Journal of Geophysical Research, 104(B12), 28957-28981, doi: 10.1029/1999jb900248.

Ziegler, P. A., S. Cloetingh, and J. D. van Wees (1995), Dynamics of intra-plate compressional deformation: The Alpine foreland and other examples, Tectonophysics, 252(1-4), 7-59, doi: 10.1016/0040-1951(95)00102-6.